Fabrication, Characterization and Electrochemical Studies of Nickel and Nickel-Based Materials

By
Mona Amiri

A dissertation submitted in partial fulfillment of the requirements of the degree of

Doctor of Philosophy in Chemistry and Materials Science

Faculty of Science and Environmental Studies

Department of Chemistry

Lakehead University, Thunder Bay, Ontario

Abstract

Nickel is a naturally abundant transition metal and is very cost effective. This, along with mechanical and magnetic characteristics, and good catalytic activity in different applications, has made it an interesting non-noble metal for various applications such as anodic/cathodic electrode materials in fuel cells, and as an electrocatalyst for oxygen and hydrogen evolution reactions. It is also consumed in various industries like the plating industry where it is an alloying element for iron or copper. Studying the effect of different factors in nickel electrochemical dissolution/ deposition would result in an enhanced understanding of the fundamental aspects of nickel electrochemistry.

Here, the anodic dissolution of an electrolytic Ni electrode was quantitatively investigated by an Inductively Coupled Plasma Atomic Emission Spectroscopy to elucidate the presence of metallic impurities. The electrolytic Ni electrode was subsequently anodically dissolved through the application of current densities at 4.0, 8.0, and 16.0 mA cm^{-2} in Watts solution, after which its crystalline nature and morphological changes were studied. Using μ- X-ray Diffractometry, changes in the crystallinity of a particular site on the electrolytic Ni electrode was investigated over time during the anodic dissolution at an applied current density of 8.0 mA cm^{-2}. The cubic crystalline nature was not altered during the dissolution of electrolytic Ni, while the diminishment of the crystalline plane of Ni (111), and the growth of the Ni (200) crystalline plane were observed during this process.

The anodic dissolution of industrial electrolytic Ni samples in Watts solution was studied in order to better understand the possible causes behind residue formation in anode baskets under actual electroplating conditions in an industrial setup. Cyclic voltammetry and

chronopotentiometry at different applied current densities were employed to characterize the dissolution behavior of these samples prior to and during a long-term dissolution process. Further, residue formation was tracked as a function of the dissolution time by collecting the residue at different stages of the process. These studies showed that the dissolution was not as uniform as desired. Likely, it began from the more susceptible sites on the surface, such as flaws or scratches, and continued through the sublayers, which resulted in a spongy structure with far lower mechanical strength. Furthermore, the residue collected throughout the long-term dissolution showed that residue formation was negligible up to final stages of the dissolution. Further, the amount of accumulated residue increased by raising the current density. Moreover, the long-term anodic dissolution of electrolytic Ni electrode was examined and electrode properties such as impedance behavior, anodic and cathodic efficiencies during the long-term anodic dissolution were assessed.

Potential applications of electrocatalysts containing nickel were also studied. An efficient electrocatalyst, based on a nanocomposite involving nickel hydroxide, carbon nitride and reduced graphene oxide (rGO), was synthesized through a facile one-step electrochemical process for the oxygen reduction reaction (ORR) in alkaline media. Comparison of nanocomposites with various concentrations of nickel hydroxide showed that the catalyst containing 44% Ni in the precursor offered the best activity. As this novel nanocomposite is comprised of low cost naturally-abundant materials, the good catalytic activity, high stability and methanol tolerance make this non-precious metal based catalyst promising for practical applications.

The need for environmentally compatible, less polluting, and more efficient energy systems has spurred extensive research into the development of batteries and other energy storage devices. Here, we report on a novel three-dimensional (3D) porous nickel modified with iridium oxide

(IrO_2) toward the design of a high-performance pseudocapacitor. The 3D porous nickel was grown directly onto a Ni plate via a facile electrochemical deposition method assisted by a simultaneously formed hydrogen bubble template. The effects of the electrodeposition time and the current density were systemically investigated, revealing that 3.0 A cm^{-2} and 150 s were the optimal conditions for the growth of the 3D porous nickel with the highest active surface area, which was subsequently modified with different quantities of IrO_2. The electrodeposited 3D porous Ni network structure served as a suitable template to accommodate the cast iridium chloride precursor, and to anchor the formed IrO_2 during subsequent thermal treatment. The formed 3D porous NiIr(10%)Ox electrode exhibited high charge/discharge stability and a superb specific capacitance 1643 F g^{-1} at 1.92 A g^{-1}, which was ~175 times higher than the 3D porous NiO, and over 95 times higher than the same amount of IrO_2 deposited on a smooth Ni substrate.

To my ***parents***,

Without your support, this would not have been possible.

Acknowledgements

First, I would like to give my sincerest gratitude to my supervisor Dr. Aicheng Chen for his continuous support through my PhD. He has guided me with patience, motivation, enthusiasm using his immense knowledge in electrochemistry and materials science, while doing research and writing the thesis. I cannot imagine having any better advisor and mentor for my PhD study that could make my PhD experience as rewarding and smooth. In addition, I would like to thank the rest of my thesis committee: Dr. Christine Gottardo and Dr. Mark Gallagher for their insightful comments. Also many thanks to Dr. Robert Mawhinney, the coordinator of PhD program in Chemistry and Materials Science Department for his great help in every step of the process.

I would like to extend my appreciation to all the former and current members of Dr. Aicheng Chen's research group, Dr. Guosheng Wu, Dr. Suresh K. Konda, Jesse Smiles, Shuai Chen, Jiali Wen, Dulanjana Wijewardena, Dr. Sapanbir Thind, Dr. Xin Chang, Zhaoyang Zhang, Dr. Maduraiveeran Govindhan, and Dr. Boopathi Sidhureddy for their friendship and collaborations. I also want to take this opportunity to thank all the faculty and staff members of Department of Chemistry, Instrument Lab and Graduate Studies for their support and encouragement.

Last, but not least, my utmost appreciation to my family. They are the ones whose unconditional love and support kept me going during my PhD. There are no words that can really express the level of gratitude and appreciation I have for them.

Table of Content

List of Figures

List of Tables

List of Abbreviations and Symbols

Ar	Argon
CA	Chronoamperometry
CP	Chronopotentiometry
CV	Cyclic Voltammetry
EASA	Electrochemically Active Surface Area
EC	Electrochemical Capacitor
EDS	Energy Dispersive X-ray Spectroscopy
EIS	Electrochemical Impedance Spectroscopy
FTIR	Fourier Transform Infrared Spectroscopy
GCE	Glassy Carbon Electrode
GO	Graphene oxide
ICP-AES	Inductively Coupled Plasma Atomic Emission Spectroscopy
LSV	Linear Sweep Voltammetry
NCG	Nickel hydroxide/Carbon nitride/reduced Graphene oxide
Ni	Nickel
ORR	Oxygen Reduction Reaction
RDE	Rotating Disc Electrode

rGO	reduced Graphene Oxide
RTIL	Room Temperature Ionic Liquids
SEM	Scanning Electron Microscopy
STEM	Scanning Transmission Electron Microscopy
t	time
XPS	X-ray Photoelectron Spectroscopy
XRD	X-ray Diffractometry

Chapter 1: Introduction

Nickel (Ni) has been the focus of intense research due to its excellent properties and abundance, particularly for use in rechargeable alkaline batteries [1], fuel cells [2], and as an electrocatalyst for oxygen evolution [3]. Furthermore, to increase corrosion resistance, Ni is included in many alloys [4-6], and has been of the focus of many electrochemical studies regarding electrodissolution and passivation processes for industrial applications [7-9]. Specifically, due to the strategic and industrial importance of electrolytic Ni spanning various areas such as transportation, service apparatus, petroleum, energy, and catalysts, it has attracted a great deal of attention [10]. Approximately 45% of the worldwide production of Ni is produced through electrorefining and electrowinning processes. The remainder of the available Ni on the market is generated from sulfide ores and lateritic sources [11, 12]. More than 150 years ago, the initial demonstration of Ni electrodeposition was carried out [13]. For industrial purposes, a Watts bath, which contains nickel salts and boric acid, was first introduced in 1916, and is still in wide use today [14].

1.1 Electrochemical dissolution/deposition of nickel

The electrochemical dissolution and passivation of Ni has been the focus of considerable scientific interest in both material science and for industrial applications [15]. In general, the electrodissolution of nickel takes place via two distinct electron transfer steps, followed by a transport step in an acidic medium [16]. The appearance of one or two voltammetric anodic peaks defines the active anodic dissolution/passive transition of nickel in acid media [17, 18]. However, the electrochemical behavior of a Ni electrode in acid media is primarily contingent on the design

of the electrode, where the composition of the electrolyte plays a significant role [19, 20]. A pitting Ni dissolution mode is possible through the presence of the appropriate concentration of aggressive ions, when an applied overpotential exceeds a certain threshold value [17]. In most cases, dissolution inhibition may occur due to the formation of a passive layer on the Ni surface, which is the result of the anodic dissolution of nickel. The formation of an oxy-hydroxide layer on the Ni surface acts to protect it from subsequent dissolution. However, the presence of certain halides such as chloride ions, might lead to the dissolution of this protective layer and hence, give rise to localized dissolution [7, 21].

The aim of the present investigation was to elucidate the changes in surface morphology, crystallinity, electrochemical behaviors, and residue formation during the dissolution of electrolytic Ni.

1.2 Fuel cells

Due to an increasing global population, concurrent with higher standards of living, a significant growth in global energy consumption has occurred over the last few decades [22]. The substantial expansion in global energy production through conventional methods has led to increased greenhouse gas emissions into the atmosphere [23]. Additionally, fossil fuel resources are limited and their efficiencies are not compelling. Fuel cells are electrochemical devices that convert chemical energy into electricity, which have the potential to replace conventional energy sources. The process of energy generation in fuel cells involves the combination of hydrogen (or a hydrogen containing fuel such as methanol) and an oxidant (e.g., either pure oxygen, or oxygen in a mixture of other gases as in the ambient atmosphere). With a constant supply of a fuel and oxidant, fuel cells can continuously produce electricity as required. Fuel cells have utility in various

applications, including transportation, or portable devices. Some of the advantages of fuel cells in comparison to other energy generating devices, are high efficiency energy conversion and zero/low emission output, which makes their development and commercialization very appealing [24, 25].

1.2.1 Oxygen reduction reaction

Major obstacles against the commercialization of the fuel cells include low reaction rates for the oxygen reduction reaction (ORR) on the cathode, insufficient durability, and high costs [26, 27]. Platinum, its alloys, and platinum containing materials are commonly used as cathode materials due to their promising catalytic activity toward the ORR [28-30]. Nevertheless, high cost, scarcity, low tolerance to fuel crossover, and CO poisoning have resulted in researchers setting their focus on the design and synthesis of new candidates for cathode materials [30, 31].

The oxygen reduction reaction at the cathode is significantly dependant on the proper adsorption of O_2 onto the catalyst [32]. The oxygen reduction reaction may proceed via two pathways [33, 34]. The complete, or direct pathway, consists of a 4-electron transfer, whereby oxygen reduces to hydroxide anions (Eq. 1.1) in an alkaline solution. In the less efficient, or incomplete pathway, oxygen initially reduces to hydro-peroxide through 2-electron transfer, and subsequently to hydroxides (Eq. 1.2) [35, 36]. Thus, the 4-electron transfer pathway is the most preferred [36].

$$O_2 + 2H_2O + 4e^- \rightarrow 4OH^- \qquad (1.1)$$

$$O_2 + H_2O + 2e^- \rightarrow HO_2^- + OH^- \qquad (1.2a)$$

$$HO_2^- + H_2O + 2e^- \rightarrow 3OH^- \qquad (1.2b)$$

In order to be able to quantify the number of electrons being transferred in the catalyzed ORR, and therefore the reaction pathway, rotating disc electrode technique is employed and Koutecky-Levich plots are analyzed at different electrode potentials. Employing the reciprocal of the slopes of the best linear fit lines, the number of electrons transferred (n) on the basis of the Koutecky-Levich equation (Eq. 1.3) is calculated.

$$\frac{1}{J} = \frac{1}{J_k} + \frac{1}{J_L} = \frac{1}{J_k} + \frac{1}{B\omega^{1/2}} \qquad (1.3a)$$

$$B = 0.62nFC_0{D_0}^{2/3}\gamma^{-1/6} \qquad (1.3b)$$

$$J_k = nFkC_0 \qquad (1.3c)$$

where J is the measured current, J_k and J_L are the kinetic and diffusion-limited currents, respectively, ω is the angular velocity of the rotating electrode, F is the Faraday constant, D_0 is the diffusion coefficient of oxygen, C_0 is the concentration of oxygen in the bulk, γ is the kinematic viscosity of the solution, and k is the electron-transfer rate constant. The constant of 0.2 is adopted if the rotating speed of the electrode is expressed in rpm.

1.3 Electrochemical capacitors

As mentioned earlier, the need for more efficient, less polluting and more environmentally compatible energy systems has garnered considerable attention on batteries and other energy storage devices [37]. Energy may be released and stored via a simple technique that involves an electrochemically active material in an electrolyte. These devices exploit electrochemical reactions and are referred to as electrochemical capacitors (EC). Based on their charge storage mechanism, electrochemical capacitors may be segregated into two subcategories; supercapacitors and

pseudocapacitors, which operate based on a double-layer effect at the electrode/electrolyte interface, or a Faradaic reaction of electroactive material at the electrode, respectively [38, 39]. Electrochemical capacitors can potentially provide high power densities and good energy densities [40], as well as rapid charge/discharge rates [41]. These characteristics are very dependent on the selected electrode material.

There are two key approaches for improving the electrochemical energy storage performance of an EC. One approach is to increase the specific surface area of the electrode which increases the number of adsorbed ions from the electrolyte. The second approach involves employing a transition metal oxide with different oxidation states, excellent redox reversibility, and chemical stability to utilize its pseudocapacitance feature [42]. Transition metals in oxide and hydroxide forms, such as $Ni(OH)_2$ [43], NiO [44, 45], $Co(OH)_2$ [46], RuO_2 [47], IrO_2 [42], and Fe_2O_3 [48] have demonstrated attractive properties for electrochemical capacitor applications. Nickel oxide has been widely investigated due to its intrinsically benign nature, high redox activity and high capacitance [49]. The achievement of specific capacitances close to theoretical values is not feasible for NiO, since it possesses low electrical conductivity. Modifications are required in order to improve this property, including the use of other oxides with high conductivity. Several studies have reported that the pseudocapacitive behavior of NiO may be enhanced in composite materials, or when combined with oxides such as TiO_2 [41].

1.4 Dissertation, rationale and scope

The primary focus of this dissertation is to investigate the electrochemical dissolution/deposition behavior of electrolytic nickel in Watts solution, and the parameters that

affect it, as well as employing different forms of Ni for green energy applications. The primary objectives of this research are:

1- To study the long-term dissolution behavior of electrolytic nickel.

2- To study the residue formation mechanism of electrolytic nickel.

3- To study the effects of crystalline structures and current density on the dissolution behavior of nickel.

4- To fabricate a nickel hydroxide related electrode for an oxygen reduction application.

5- To fabricate a macroporous nickel oxide structure loaded with iridium oxide for use in an energy storage application.

In the following chapters, a detailed literature review highlighting recent improvements in Ni and Ni related materials, as well as the results of the studies carried out in this research is presented.

For chapter 2, a thorough literature review was conducted, where the electrochemical dissolution and deposition behavior of nickel in acidic media, as well as the effects of various parameters such as additives or temperature, along with several applications of Ni are presented. Chapter 3 presents the different electrode fabrication procedures used in this research work, including the various characterization methods that are employed to investigate the morphology, crystalline structure, and electrochemical properties of the prepared electrodes.

Chapter 4 elucidates the changes that occurred to the surface morphology and crystallinity of the electrode during the electrochemical dissolution process. Additionally, the effects of applied current densities at 4.0, 8.0, and 16.0 mA cm^{-2} in Watts solution on the anodic dissolution of electrolytic Ni electrode are shown. More detailed crystalline structural studies were accomplished

using μ-XRD. In chapter 5, the anodic dissolution of industrial electrolytic Ni samples in Watts solution is studied to reveal the possible causes behind the formation of residues at the anode. Cyclic voltammetry and chronopotentiometry at different applied current densities are employed for assessing the dissolution behavior of these samples, while the formed residue was extracted. Optical and scanning electron microscopy, energy dispersive spectroscopy, and X-ray diffractometry (XRD) were also used to further analyze the properties of the residues and samples throughout the process.

In chapter 6, a facile one-step electrochemical fabrication method for the preparation of a nanocomposite, which involved nickel hydroxide, carbon nitride, and reduced graphene oxide (rGO), is reported, and utilized as an efficient electrocatalyst for the oxygen reduction reaction in alkaline media. This novel nanocomposite, is comprised of low cost naturally-abundant materials, exhibited good catalytic activity, high stability, and methanol tolerance, which makes this non-precious metal based catalyst promising for practical applications.

Chapter 7 reports the simple fabrication of nickel oxide supported IrO_2, via electrodeposition at high current densities and annealing procedures for pseudocapacitor applications. The charge/discharge and cyclic voltammetry studies showed that the prepared electrode demonstrated an excellent pseudocapacitance behavior and high specific capacitance, as well as good capacitance retention following 1000 charge/discharge cycles.

References

[1] S.-G. Kim, S. P. Yoon, J. Han, S. W. Nam, T. H. Lim, I.-H. Oh, S.-A. Hong, A study on the chemical stability and electrode performance of modified NiO cathodes for molten carbonate fuel cells, *Electrochim. Acta,* 2004, **49**, 3081-3089.

[2] V. Rashkova, S. Kitova, I. Konstantinov, T. Vitanov, Vacuum evaporated thin films of mixed cobalt and nickel oxides as electrocatalyst for oxygen evolution and reduction, *Electrochim. Acta,* 2002, **47**, 1555-1560.

[3] Q. Wu, L. Jiang, Q. Tang, J. Liu, S. Wang, G. Sun, Activity and stability of the $Ni(OH)_2$-MnO_x/C composite for oxygen reduction reaction in alkaline solution, *Electrochim. Acta*, 2013, **91**, 314-322.

[4] E. M. A. Martini, S. T. Amaral, I. L. Muller, Electrochemical behaviour of Invar in phosphate solutions at pH= 6.0, *Corros. Sci.*, 2004, **46**, 2097-2115.

[5] P. Marcus, Surface science approach of corrosion phenomena, *Electrochim. Acta*, 1998, **43**, 109-118.

[6] A. Gildenpfennig, U. Gramberg, G. Hohlneicher, Passivation and corrosion of the metallic high performance materials Alloy 33 and MC-Alloy in different environments, *Corros. Sci.*, 2003, **45**, 575-595.

[7] A. Jouanneau, M. Keddam M. C. Petit, A general model of the anodic behaviour of nickel in acidic media, *Electrochim. Acta*, 1976, **21**, 287-292.

[8] M. R. Barbosa, S. G. Real, J. R. Vilche, A. J. Arvıa, Comparative potentiodynamic study of nickel in still and stirred sulfuric acid-potassium sulfate solutions in the 0.4–5.7 pH range, J. *Electrochem. Soc.*, 1988, **135**, 1077-1085.

[9] J. Gregori, J. Agrisuelas, D. Gimenez, M. P. Pena, J. J. Garcıa- Jareno, F. Vicente, Aplicación de un puente LCR en la caracterización de superficies de níquel tratadas voltamperométricamente en medio ácido en ausencia y presencia de ión cloruro, *Rev. Metal.*, 2003, **39**, 346-356.

[10] M. T. Anthony, D. S. Flett, Nickel processing technology: a review, *Miner. Ind. Int.*, 1997, **1**, 26-42.

[11] D. M. Muir, E. Ho, Process review and electrochemistry of nickel sulphides and nickel mattes in acidic sulphate and chloride media, *Miner. Process. Extr. Metall.*, 2006, **115**, 57-65.

[12] C. Lupi, M. Pasquali, A. Dellera, Studies concerning nickel electrowinning from acidic and alkaline electrolytes, *Miner. Eng.*, 2006, **19**, 1246-1250.

[13] A. Brenner, V. Zentner, C. W. Jennings, Plating, 1952, **39**, 865-927.

[14] O. P. Watts, Rapid nickel plating, *Trans. Am. Electrochem. Soc.*, 1916, **29**, 395.

[15] A. G. Muñoz, G. Benitez, M. E. Vela, R. C. Salvarezza, Influence of the adsorption of N species on the anodic dissolution of Ni, *Langmuir*, 2004, **20**, 2361-2368.

[16] J. Gregori, J. J. Garcıa-Jareno, D. Gimenez, F. Vicente, Kinetic calculations of the Ni anodic dissolution from EIS, *J. Solid State Electrochem.*, 2005, **9**, 83-90.

[17] S. G. Real, M. R. Barbosa, J. R. Vilche, A. J. Arvıa, Influence of chloride concentration on the active dissolution and passivation of nickel electrodes in acid sulfate solutions, *J. Electrochem. Soc.*, 1990, **137**, 1696-1702.

[18] K. Deo, S. G. Mehendale, S. Venkatachalam, Electrochemical dissolution of nickel in sulphuric acid by alternating current, *J. Appl. Electrochem.,*1976, 6, 37-43.

[19] M. Zamin, M. B. Ives, Effect of chloride ion concentration on the anodic dissolution behavior of nickel, *Corrosion*, 1973, **29**, 319-324.

[20] S. G. Real, J. R. Vilche, A. J. Arvia, The characteristics of the potentiodynamic potential/current profiles obtained with the Ni/0.5 N H_2SO_4 interface. A contribution to the mechanism of the electrode process, *Corros. Sci.,* 1980, **20**, 563-586.

[21] B. MacDougall, Effect of chloride ion on the localized breakdown of nickel oxide films, *J. Electrochem. Soc.*, 1979, **126**, 919-925.

[22] C. J. Brinker, D. Ginger, Science Policy Reports, Chapter 6: Nanotechnolgy for Sustainability - Energy Conversion, Storage, and Conservation Springer, Netherlands, 2011, **1**, 261.

[23] H. D. Matthews, N. P. Gillett, P. A. Stott, K. Zickfeld, *Nature*, 2009, **459**, 829-832.

[24] R. K. Shah, Recent Trends in Fuel Cell Science and Technology, Chapter 1: Introduction to Fuel Cells, Anamaya Publishers, New Delhi, 2007, 1.

[25] K. V. Kordesch, G. R. Simander, Environmental impact of fuel cell technology, *Chem. Rev.* 1995, **95**, 191-207.

[26] W. He, H. Jiang, Y. Zhou, S. Yang, X. Xue, Z. Zou, X. Zhang, D. L. Akins, H. Yang, An efficient reduction route for the production of Pd–Pt nanoparticles anchored on graphene nanosheets for use as durable oxygen reduction electrocatalysts, *Carbon*, 2012, **50**, 265-274.

[27] J. Feng, Y. Liang, H. Wang, Y. Li, B. Zhang, J. Zhou, J. Wang, T. Regier, H. Dai, Engineering manganese oxide/nanocarbon hybrid materials for oxygen reduction electrocatalysis, *Nano Res.*, 2012, **5**, 718-725.

[28] L. Feng, L. Yang, Z. Huang, J. Luo, M. Li, D. Wang, Y. Chen, Enhancing electrocatalytic oxygen reduction on nitrogen-doped graphene by active sites implantation, *Sci. Rep.*, 2013, **3**, 3306.

[29] X.-Y. Yan, X.-L. Tong, Y.-F. Zhang, X.-D. Han, Y.-Y. Wang, G.-Q. Jin, Y. Qin, X.-Y. Guo, Cuprous oxide nanoparticles dispersed on reduced graphene oxide as an efficient electrocatalyst for oxygen reduction reaction, *Chem. Commun.*, 2012, **48**, 1892-1894.

[30] J. Zhang, C. Guo, L. Zhang, C.M. Li, Direct growth of flower-like manganese oxide on reduced graphene oxide towards efficient oxygen reduction reaction, *Chem. Commun.*, 2013, **49**, 6334-6336.

[31] K. Zhang, Q. Yue, G. Chen, Y. Zhai, L. Wang, H. Wang, J. Zhao, J. Liu, J. Jia, H. Li, Effects of acid treatment of Pt−Ni alloy nanoparticles@graphene on the kinetics of the oxygen reduction reaction in acidic and alkaline solutions, *J. Phys. Chem. C*, 2010, **115**, 379-389.

[32] Y. Feng, F. Li, Z. Hu, X. Luo, L. Zhang, X.-F. Zhou, H.-T. Wang, J.-J. Xu, E.G. Wang, Tuning the catalytic property of nitrogen-doped graphene for cathode oxygen reduction reaction, *Phys. Rev. B*, 2012, **85**, 155454.

[33] Y. Qiao, S.-J. Bao, C. M. Li, Electrocatalysis in microbial fuel cells—from electrode material to direct electrochemistry, *Energ. Environ. Sci.*, 2010, **3**, 544-553.

[34] W. Chen, J. Kim, S. Sun, S. Chen, Electrocatalytic reduction of oxygen by FePt alloy nanoparticles, *J. Phys. Chem. C*, 2008, **112**, 3891-3898.

[35] C. Song, J. Zhang, Electrocatalytic Oxygen Reduction Reaction, in PEM Fuel Cell Electrocatalysts and Catalyst Layers, Editor J. Zhang, Springer London. 2008, 89.

[36] A. Chen, C. Ostrom, Palladium-based nanomaterials: Synthesis and electrochemical applications, *Chem. Rev.*, 2015, **115**, 11999-12044.

[37] X. Xia, J. Tu, Y. Zhang, Y. Mai, X. Wang, C. Gu, X. Zhao, Three-dimentional porous nano-Ni/$Co(OH)_2$ nanoflake composite film: a pseudocapacitive material with superior performance, *J. Phys. Chem. C*, 2011, **115**, 22662-22668.

[38] C. Guan, J. Liu, Y. Wang, L. Mao, Z. Fan, Z. Shen, H. Zhang, J. Wang, Iron oxide-decorated carbon for supercapacitor anodes with ultrahigh energy density and outstanding cycling stability, *ACS Nano*, 2015, **9**, 5198-5207.

[39] H. B. Li, M. H. Yu, F. X. Wang, P. Liu, Y. Liang, J. Xiao, C. X. Wang, Y. X. Tong, G. W. Yang, Amorphous nickel hydroxide nanospheres with ultrahigh capacitance and energy density as electrochemical pseudocapacitor materials, *Nat. Commun.*, 2013, **4**, 1894.

[40] X. Cheng, X. Gui, Z. Lin, Y. Zheng, M. Liu, R. Zhan, Y. Zhu, Z. Tang, Three-dimensional α-Fe_2O_3/carbon nanotube sponges as flexible supercapacitor electrodes, *J. Mater. Chem. A.*, 2015, **3**, 20927-20934.

[41] L. H. Cui, Y. Wang, X. Shu, J. F. Zhang, C. P. Yu, J. W. Cui, H. M. Zheng, Y. Zhang, Y. C. Wu, Supercapacitive performance of hydrogenated TiO_2 nanotube arrays decorated with nickel oxide nanoparticles, *RSC Adv.*, 2016, **6**, 12185-12192.

[42] Y. T. Shih, K. Y. Lee, Y. S. Huang, Characterization of iridium dioxide–carbon nanotube nanocomposites grown onto graphene for supercapacitor, *J. Alloys Compd.*, 2015, **619**, 131-137.

[43] L. L. Zhang, Z. Xiong, X. Zhao, A composite electrode consisting of nickel hydroxide, carbon nanotubes, and reduced graphene oxide with an ultrahigh electrocapacitance, *J. Power Source.*, 2013, **222**, 326-332.

[44] S.Y. Kim, H.M. Jeong, J.H. Kwon, I.W. Ock, W.H. Suh, G.D. Stucky, J.K. Kang, Nickel oxide encapsulated nitrogen-rich carbon hollow spheres with multiporosity for high-performance pseudocapacitors having extremely robust cycle life, *Energ. Environ. Sci.*, 2015, **8**, 188-194.

[45] K. Tao, P. Li, L. Kang, X. Li, Q. Zhou, L. Dong, W. Liang, Facile and low-cost combustion-synthesized amorphous mesoporous NiO/carbon as high mass-loading pseudocapacitor materials, *J. Power Source.*, 2015, **293**, 23-32.

[46] H. Li, M. Yu, X. Lu, P. Liu, Y. Liang, J. Xiao, Y. X. Tong, G. W. Yang, Amorphous cobalt hydroxide with superior pseudocapacitive performance, *ACS Appl. Mater. Interfaces*, 2014, **6**, 745-749.

[47] J. Y. Kim, K. H. Kim, H. K. Kim, S. H. Park, K. C. Roh, K. B. Kim, Template-free synthesis of ruthenium oxide nanotubes for high-performance electrochemical capacitors, *ACS. Appl. Mater. Interfaces*, 2015, **7**, 16686-16693.

[48] C. H. Xu, P. Y. Shen, Y. F. Chiu, P. W. Yeh, C. C. Chen, L. C. Chen, C. C. Hsu, I. C. Cheng, J. Z. Chen, Atmospheric pressure plasma jet processed nanoporous Fe_2O_3/CNT composites for supercapacitor application, *J. Alloys Compd.*, 2016, **676**, 469-473.

[49] S.K. Meher, P. Justin, G.R. Rao, Nanoscale morphology dependent pseudocapacitance of NiO: Influence of intercalating anions during synthesis, *Nanoscale*, 2011, **3**, 683-692.

Chapter 2: Literature Review

2.1 Introduction

Nickel is of great importance due to its various uses in different industries, including rechargeable alkaline batteries [1-5], as electrode materials in fuel cells [6-9], electrocatalysts for oxygen evolution [10-14], and as catalysts in the fertilizer industry [15-19]. It is also consumed in the plating industry as well as enabling the green tint in glasses. It is primarily used in nickel steels and various nickel cast iron alloys [20-22], and is widely consumed in many commercial and special alloys, such as nickel brasses and bronzes, alloys with copper, chromium, aluminum, lead, cobalt, silver, and gold, Inconel, Incoloy, Monel, and Nimonic. Further, it has applications in biomaterials such as shape memory alloys [22-24]; however, it poses human health concerns due to possible allergic reactions in the body in response to nickel ions [21, 25]. Recently, the use of Ni electrodes in diabetes screening components has been proposed [26-27].

Many of these aforementioned applications involve electrolytes and an understanding of the electrochemical behavior of nickel as relates to liquid media. Therefore, behavior related to the deposition or anodic dissolution and passivation of nickel in acidic and basic media via different electrochemical techniques have garnered significant attention over the last few years [11, 28].

2.2 Electrochemical dissolution

Most nickel applications demand a sufficient fundamental understanding of their electrochemical dissolution behavior in different electrolytes, which have been achieved to some

extent through intensive studies using various laboratory based electrochemical techniques. The important information yielded so far, is presented here.

2.2.1 Dissolution in acids

2.2.1.1 Sulfuric acid

Using potentiodynamic polarization curves of nickel in a sulfuric acid solution (Figure 2.1) [29], there are four regions in the nickel dissolution process that may be categorized as: i) dissolution, ii) another active dissolution, iii) passive dissolution, and iv) transpassive dissolution. Based on these results, Itagaki et al. [29] have suggested that each dissolution region has a different mechanism.

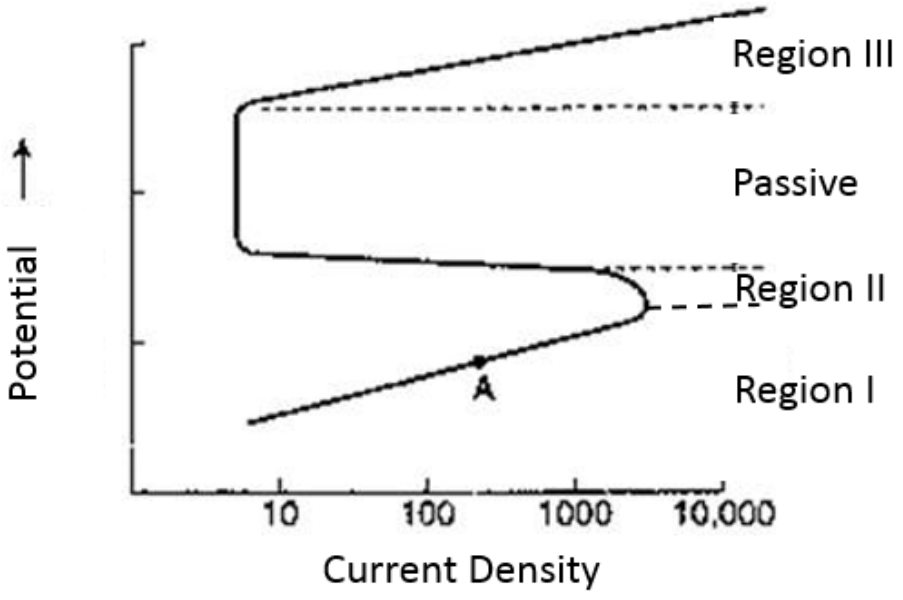

Figure 2.1 Polarization curves of nickel electrodes in sulfuric acid solutions at different pH levels.

For dissolution in region (II) [29], it has been reported that the passive film on Ni is NiO. The transient current at the initial stage of anodic oxidation is large; however, it suddenly decreases. It is presumed that the decreased current is derived from the formation of passive NiO species. Subsequently, it was concluded that the second dissolution region (II) is the pre-passive region between active dissolution and passivation.

For region (III), the authors [29] employed Sato & Okamoto's proposed mechanism as shown in Eqs. 2.1 and 2.2. Colorimetric determination revealed that the dissolved species were divalent ions. Since a passive film exists at the transpassive dissolution potential, the authors were doubtful as to the existence of adsorbed species. The passive film on nickel was NiO. Turner et al. [20] suggested that, in the passive region, passivation follows a solid-state mechanism.

Using rapid polarization and steady-state polarization techniques, the generally accepted active electrochemical dissolution of nickel in sulfuric acid with pH of 0-3 [29-32] follows the anodic dissolution reactions as follows:

$$[Ni]_m + H_2O \Leftrightarrow [Ni]_m(H_2O)_{ad} \Leftrightarrow [Ni]_{m-1}Ni(OH)_{ad} + H^+_{aq} + e^-$$

$$or \qquad Ni + OH^- \underset{k}{\overset{k}{\rightleftharpoons}} NiOH_{ad} + e^- \tag{2.1}$$

$$[Ni]_{m-1}Ni(OH)_{ad} \Leftrightarrow [Ni]_{m-1}(NiOH^+)_{ad} + e^-$$

$$or \qquad NiOH_{ad} \overset{k''}{\rightarrow} NiOH^+ + e^- \tag{2.2}$$

$$[Ni]_{m-1}(NiOH^+)_{ad} + H_2O \Longrightarrow [Ni]_{m-1} + Ni(OH)_2 + H^+_{aq}$$

$$\& \quad [Ni]_{m-1}[Ni(OH)_2] \Leftrightarrow [Ni]_{m-1}[NiO] + H_2O \tag{2.3}$$

$$[Ni]_{m-1}(NiOH^+)_{ad} \Longrightarrow [Ni]_{m-1} + NiOH^+_{aq} + H^+ \Leftrightarrow [Ni]_m + H_2O + Ni^{2+}$$

$$or \qquad NiOH^+ \rightarrow Ni^{2+} + OH^- \qquad (2.4)$$

Using impedance analysis, Barbosa et al. [32] proposed that the adsorption of water occurred during the reaction Eq. 2.1, after which the adsorbed water underwent a second transformation as in Eq. 2.2. The reactions of Eq. 2.3 and Eq. 2.4 were competitive reactions in the formation of nickel oxide/hydroxide, as the passive layer and nickel dissolution through soluble reaction intermediates, respectively.

The rate-determining step changed from step Eq. 2.1 to step Eq. 2.3, and Eq. 2.4 as $NiOH^+$ ion concentration increased in the vicinity of the surface. The rate of anodic dissolution was also controlled by the population of OH^- ions that were involved in a reaction cycle that consisted of steps Eq. 2.1, Eq. 2.2, and Eq. 2.3 [30]. It is believed that first stage passivation was due to the formation of $Ni(OH)_2$ which was followed by the formation of Ni_2O_3 species at more positive potentials than those of existing $Ni(OH)_2$ species [32].

The immersion of oxide-free Ni in 0.05 M H_2SO_4 in a potential range of from -0.25 to -0.2V [33] resulted in a step flow dissolution mechanism, where increasing potential initiated the more rapid dissolution of Ni with the formation and growth of three dimensional pits. The immersion of Ni with an oxide layer formed in air, in the same solution at passive potentials, led to a gradual dissolution of the current layer and the formation of a passive layer. The morphology and structure of the secondary layer was different than the first.

The reaction in Eq. 2.2 is a rate determining step. The adsorption of $NiOH_{ads}$ obeyed the Langmuir isotherm, and fractional coverage of $NiOH_{ads}$ was much smaller than unity, for dissolution in region (I), and an expression for steady-state current was obtained [29]:

$$i_w = F\left(kk^{"}/_{k'}\right)[OH^-]exp\{(1+\beta)FE/RT\} \quad (2.5)$$

where *F* is Faraday constant, *R* is the gas constant, T is temperature, and β is a symmetry factor, respectively. The Tafel slope was derived from Eq. 2.5 [29]:

$$\partial E/_{\partial \log i_w} = 2.303RT/_{(1+\beta)F} \quad (2.6)$$

and $\partial E/_{\partial \log i_w}$ is calculated as 40 mV.dec^{-1} by assuming p = 0.5. Eq. 2.5 satisfied the experimentally obtained reaction parameters.

A scheme of transpassive dissolution was proposed by Keddam et al. [34], which is in agreement with PDM studies and experiments conducted by Bojinov and Tzvetkoff [35]:

$$\begin{array}{ccccc} Ni \rightleftharpoons Ni(II)_{ad} & \rightleftharpoons & Ni(II)^*_{ad} & \rightleftharpoons & Ni(III)_{ad} \\ \searrow & & \swarrow & & \downarrow \\ & Ni(II) & & & O_2 \end{array} \quad (2.7)$$

It has been mentioned [29] that the formation of $Ni(II)_{ad}$* exhibited accelerated transpassive dissolution. Therefore, it was proposed that the oxidation of NiO to a higher valent oxide yielded active dissolution sites, such as the formation of active species or point defects.

In Figure 2.2 an overall schematic analytical pathway of nickel, proposed by Davis et al. [36], is presented, which depicts the Ni dissolution and deposition cycles.

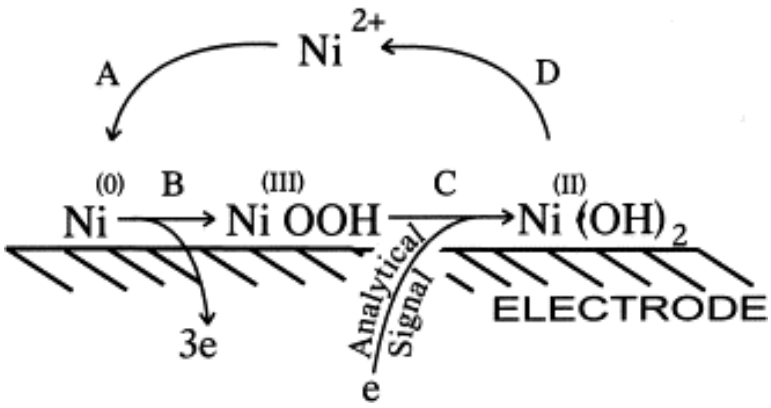

Figure 2.2 Schematic of nickel analytical pathway. Image reproduced from reference [36] with permission. Copyright 2002, Elsevier.

2.2.1.2 Nitric acid

Effect of nitric acid media, or more precisely, its cathodic reaction products was more complex than other media [37]. The active dissolution of nickel occurred due to its interactions with the reduction products of HNO_3 over a wide range of potentials and acid concentrations [37], and this process was reported to be kinetically controlled. The increased concentration of HNO_3 [38] resulted in the shifting of the anodic peak potential toward more noble potentials, and increasing the current density of the anodic dissolution peak. Also, the addition of Cl^- up to a certain concentration [38] had no influence on the anodic polarization. For concentrations of Cl^- beyond this threshold, the current density increased and the dissolution was more of a pitting form.

2.2.1.3 Hydrochloric acid

The electrolytic etching of nickel-42 in HCl [39] occurred only in the active region, and there is no pitting following etching. It appeared that during dissolution in an HCl electrolyte, the (111)

plane was most susceptible to dissolution in contrast to the HNO_3 solution, as the intensity of (111) plane decreased significantly following electrolytic etching in a XRD pattern.

2.2.1.4 Acetic acid

Badea and Badea studied [40] the anodic and cathodic behavior and time dependence of the corrosion potential for Ni in aqueous acetic acid solutions of various concentrations, between 0.5 and 13 M CH_3COOH. In comparison to sulfuric acid solutions, acetic acid solutions have smaller i_{cr} values, over one order of magnitude, which indicated that acetic acid solutions were less corrosive. However, the i_p was the same, which signified that the passive film had the same chemical nature in both solutions. It has been suggested that in order to increase the Ni corrosion resistance in acetic acid solutions, oxygen should be eliminated from the solution, since the active state of nickel proceeds via the depolarization of oxygen.

2.2.1.5 Phosphoric acid

Nickel EIS studies [35] in a 1 M H_3PO_3 solution revealed the existence of competition between transpassive dissolution and secondary passivation. Further, the interactions between the Ni(II) film and phosphate anions were considered to be weaker than that of sulfate anions.

2.2.2 Dissolution in ionic liquids

Zhang et al. studied [41] the dissolution behavior of Ni in Lewis acidic and basic 1-butyl-3-methyl-imidazolium chloride (BMIC) aluminum chloride ($AlCl_3$) ionic liquids (ILs). Ni exhibited a wide range of passivity with a low passivation current density in both solutions. In acidic solution, Ni demonstrated an active-to-passive behavior, while in a basic solution, it did not

dissolve. It appears that the good corrosion resistance of Ni in a chloride containing solution, was due to the differences in Cl^- activity [41].

2.2.3 Effect of Ni crystal size and microstructure

Electrode history [21] and microstructure influence the dissolution behavior. Studies have indicated [42-43] that for materials with a passive film, the smaller the grain size, the lower the dissolution rate becomes, which is due to the more rapid formation of a passive film as a result of a larger grain boundary density. However, this is dependent on the electrolyte in which the material is immersed within. For a sulfuric acid solution, smaller grains result in only a higher dissolution rate [43]. The passive current density for nanocrystalline Ni was reported to be higher than that of Ni with coarser grain sizes, which was related to the defective nature of the passive film on its nanocrystalline structure [44]. It is noteworthy that for nanocrystalline Ni, the finer the grain, the higher the breakdown potential became. Further, the corrosion rate was lower in nanocrystalline Ni on contrast to its bulk counterpart.

2.2.4 Effect of concentration and pH

Hara and Sugimoto [45] studied the composition and structure of passive and transpassive films on Ni in regard to the potential and pH of the solution by means of modulated reflection spectroscopy. Based on their results, in acidic media ($pH \leq 4$) at higher potentials in the transpassive stage, or during primary passivation in neutral solutions ($6 < pH < 9$), the formation of NiO_x ($1 < x < 1.5$) was anticipated at the outermost portion of the passive layer, which consisted primarily of NiO. Increasing potential elevated the value of x, which was related to the excess

oxygen content, and therefore Ni^{3+} ion content. In neutral solutions at transpassivation and oxygen evolution potentials, γ-$NiOOH.2NiO_2$ formed on the NiO_x surface. In alkaline solutions ($pH \geq 10$) at lower potentials in the passive region, $Ni(OH)_2$ was formed, which at pH levels lower than or equal to 12, would be in α-$Ni(OH)_2$ form, and in more potent alkaline solutions ($pH \geq 13$), in β-$Ni(OH)_2$ form. It was observed [40] that at lower potentials, a two-layered passive film, with a compact NiO inner layer and α- or β-$Ni(OH)_2$ outer layer was formed. At higher potentials, α- and β-$Ni(OH)_2$ were oxidized to γ-$NiOOH.NiO_2$ or β-NiOOH, respectively.

The effects of acid concentrations [20] on the steady state polarization curves are shown in Figure 2.3. For concentrations of up to 5 M, the results revealed a classical active-passive transition, with the "passive" current density increasing with the acid concentration. It was suggested that the relatively high dissolution rate in acidic solutions makes it unlikely for the potential to contribute significantly to the formation of NiO, thus passivation. Other research [29] conducted through multiple angle incidence reflectivity measurements showed that, in a 1 M sulfuric acid solution, the passive NiO film was oxidized to form NiOOH.

In 10 M solutions [20], the "passive" current was again increased even though the active/passive transition was no longer present. The "passive" current fell by at least one decade, which was suggested to be due to the presence of sulfates on the surface, particularly β-$NiSO_4.6H_2O$. At concentrations higher than 10 M [46], two plateaux were observed in the polarization curves, rather than two maxima, which appeared in lower concentrations. In practical terms, the currents had the same value; however, the surface aspect in each plateau was different: a generalized attack occurred and grains were revealed in the activation plateau, whereas in transpassivation, the surface was electropolished and the micro-roughness disappeared.

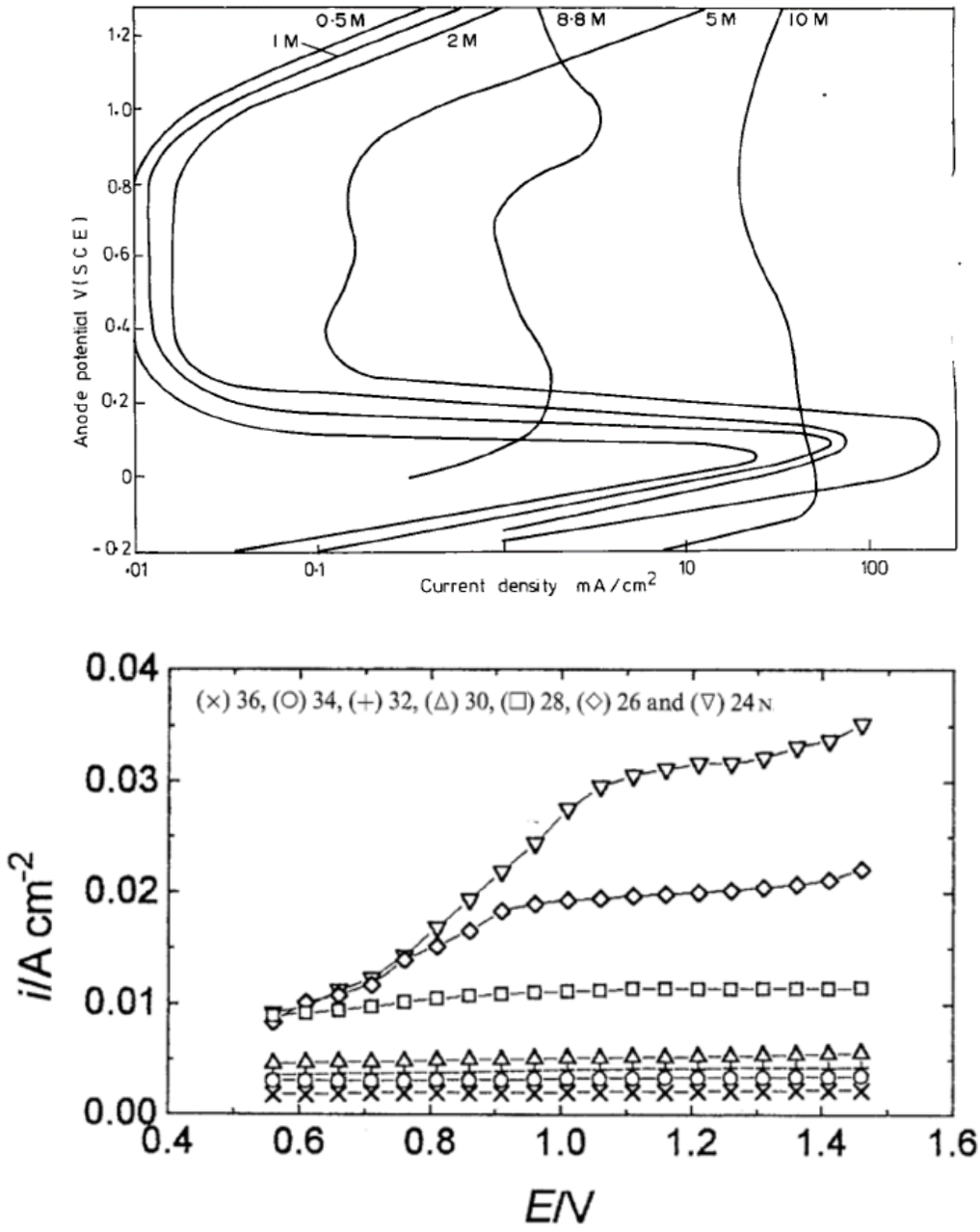

Figure 2.3 Current density vs. potential of nickel in different concentrations of sulfuric acid (potentials are quoted against the normal hydrogen electrode). Images reproduced from references [20] and [46] with permission. Copyright 1973, Elsevier and 1996, Springer, respectively.

Using double-layer capacity measurements, Turner et al. [20] showed that, in general, the passive film became thinner with increasing electrolyte concentrations. It was shown [20] that at

potentials anodic to the passivating potential, a surface film may be observed; however, no dependence on concentration was indicated.

Deo et al. [47] proposed that lower nickel dissolution efficiencies in dilute sulfuric acid was the consequence of the formation of insoluble oxide films during the electrochemical evolution of oxygen in the positive half cycle. The decrease in passivation at higher concentrations might be due to the ability of concentrated sulfuric acid to dissolve the oxide film.

2.2.5 Effect of temperature

The effect of temperature on the steady state polarization curves in 0.5 M H_2SO_4 [20] is an overall increase in the "passive" current density. It was concluded [20] that the passivation potential is temperature independent, although the potential range of the passive region decreased significantly with increasing temperature. At potentials anodic to the passivation potential the dissolution rate increased rapidly with temperature.

2.2.6 Effect of additive anions

Typically, a passive film will form on a nickel surface in a sulfuric acid solution, which reduces the dissolution rate. However, the presence of certain anions such as chloride may prevent it from passivating, causing localized dissolution such as pitting [27, 48]. In general, anions play a significant role in the kinetics of anodic dissolution [21]. Shein et al. [49] proposed that the effect of halides present in the sulfate solution on the dissolution behavior of Ni is contingent on the attributes of the solution. Based on the pH of the solution, species of anion and its concentration, the Ni dissolution rate may either increase or decrease [49].

Using cyclic voltammetry, it was shown [49] that the current of the peak related to nickel dissolution following an increase in the first cycle, decreased over several cycles to smaller values, i.e. to the value of a blank solution in the case of chloride, which is the most studied case. Also [49], there was a shift in the anodic peak toward more positive potentials. Based on the results, the shift increases in the presence of halides with the order of $F^- < Cl^- < Br^- < I^-$. It has been shown that, Cl^-, Br^-, and I^- ions have a passivating effect on nickel dissolution at low anodic potentials, while at more positive potentials they might increase the dissolution rate. This deceleration effect might be due to the competitive adsorption of these ions rather than hydroxide, which reveals the inhibition of dissolution. An additional effect of anions was the adsorption of intermediate species, the desorption of which resulted in the formation of new active sites on the electrode surface.

In the impedance plot, an inductive loop appeared rather than a capacitive loop at low frequencies [21,48], which was believed [32] to be due to the adsorption and transformation of Cl^- ions on the electrode active sites, and desorption of chloride species for intermediates. It was concluded [32] that the chloride interfered with reactions Eq. 2.3 and Eq. 2.4, causing the formation of $[Ni]_{k-1}(NiCl)_{ad}$ and $[Ni]_{k-1}(NiClH)^+{}_{ad}$ intermediate species, which inhibited passivation; hence, initiating localized corrosion.

Gregori et al. [50] proposed that the inductive loop appeared only in acidic media at pH < 3.5 when the Ni(I)/Ni(II) reaction was slower than Ni(II)/Ni^{2+}(aq), which meant that Ni(I) accumulated on the electrode surface, attained a maximum, after which its concentration decreased.

Increasing the Cl^- concentration, and therefore $[Cl^-]/[OH^-]$ or $[Cl^-]/[HCO_3^-]$ ratios, favored the adsorption of Cl^- ions and the deterioration of the passive film such that the protective layer

breakdown occurred at lower potentials [27] and salt layer precipitation ensued [25]. Overall, it decreased the passivation tendency of Ni [51].

During the localized dissolution of Ni, a series of complex reactions such as the diffusion of soluble species through pores, and the precipitation of insoluble phases may occur. However, a proposed simplified mechanism [52] for passive layer breakdown via aggressive anions (such as chloride ions) occurred according to the following steps: i) preferential competitive adsorption of aggressive anions over species such as H_2O or OH^-; ii) diffusion of halide anions through the oxide layer, possibly via cracks (flaws) and binding with metal sites; iii) diffusion of halide ions through the metal oxide lattice and binding to metal sites; iv) adsorption of aggressive anions on the oxide film, which promoted its dissolution. The proposed reactions are as follows (Eq. 2.8):

$$Ni + X^- \rightleftharpoons Ni(X^-)_{ad} \quad (2.8a)$$

$$Ni(X^-)_{ad} \rightleftharpoons NiX + e^- \quad (2.8b)$$

$$NiX + OH^- \rightarrow Ni(X)(OH)_{aq} + e^- \quad (2.8c)$$

Or

$$NiX + X^- \rightarrow NiX_{2_{aq}} + e^- \quad (2.8d)$$

where X^- = Cl^-, Br^-, or F^-. Typically, the smaller the anion, the easier its penetration into the lattice, therefore more aggressive it can get [53].

An interesting study conducted on the F^- ion effect in an acidic medium on single crystal Ni [54] samples grown with different crystal orientations revealed that the dissolution rate was also dependent on the electrode structural orientation.

2.3 Electrodeposition

Nickel electrodeposition has been used because of its excellent surface coverage [55]. In most cases [56-58] the electrodeposition of nickel is accompanied by pronounced hydrogen evolution. Therefore, the efficiency is not 100% and the pH in close proximity to the cathode is always higher than the bulk electrolyte. If the rise of pH is not avoided, at higher currents, insoluble nickel hydroxide will form on the surface, which is usually not desirable for nickel deposition [57, 59]. In order to avoid this increase in pH, a boric acid buffer is added to the deposition bath [60].

An electrodeposition study employing a supercritical CO_2 process showed that there was a relationship between microstructure characteristics; i.e. grain size and crystallographic orientation, and the internal stress of the Ni coating [60]. Deposition of nickel on gold electrodes was studied in a sulfate bath for catalytic purposes [58]. The deposition of Ni occurs in two different ways; the deposition of Ni^0 via adsorption and $Ni(OH)_2$, which is believed to be chemical precipitation. The former occurs at potentials of below -0.8 V, which might be due to a charge-transfer reaction by Ni^{2+} discharge (Ni ion reduction). Nickel hydroxide formation on the electrode surface is associated with H_2 evolution, and a subsequent increase in pH at the double layer.

It is worthy of mention that at potentials of above -0.75 V (Ni^0/Ni^{2+} reversible Nernst potential), hydroxide deposition via reaction Eq. 2.2 takes place due to a strong basic environment. Further, results have shown that by increasing the deposited layer thickness, it is most probable that $Ni(OH)_2$ surrounds the Ni^0 deposits.

However, studies involving the deposition of Ni on a Pd-Au (111) bimetallic substrate have shown a preferential behavior for the first Ni monolayer [61]; i.e. it is faster on Au (111) than Pd-

Au (111). This effect disappears after the first monolayer, as the Pd-Ni binding energy (80 meV) is smaller than that of Ni-Au.

Furthermore, a dissolution study of the deposited coating showed [61] that a Ni monolayer from Pd islands dissolved much more rapidly than Au (111). It has also been mentioned that H-desorption and H-adsorption take place with Ni deposition and dissolution, respectively.

The electrodeposition of nickel on a polypyrrole film has been successfully achieved through two potential steps [62]. For this purpose, the polymer layer needs to attain a conductive state via the application of positive potentials. The subsequent lowering of the potential to appropriate values for metal ion reduction and deposition occurs for a brief time.

2.3.1 Effect of temperature

Temperature may severely impact the processes that occur at the electrode/electrolyte interface [56], while drastically altering the Faradaic current. Studies of nickel deposition on nickel in Watts solution (containing chloride and sulfate salts of nickel) have revealed a two-step deposition process (Eq. 2.9) consisting of kinetics and adsorption over a broad range of temperatures and potentials.

$$Ni(II) + e^- \rightarrow Ni(I)_{ad}$$
$$Ni(I)_{ad} + e^- \rightarrow Ni \qquad (2.9)$$

An increase in temperature results in an increase of current [88], which is believed to be due to a higher reaction rate, since Ni deposition in Watts solution is mediated by charge transfer. A rise in temperature of ~ 25 ºC (from 40 ºC to 65 ºC) may reduce the internal stress of the coating

by ~40% (a decrease of from 500 MPa to 300 MPa) [60]. This is due to an increase in the electrical conductivity of the electrolyte [60], which leads to a lower grain nucleation rate, therefore, larger grains, and consequently, lower internal stress.

2.3.2 Effect of saccharin addition

It has been reported [44, 63] that the addition of saccharin to Ni plating in a sulfamate-based bath, resulted in the formation of smaller grains. The concentration of saccharin controls the grain refinement level [43]. Secondary-ion mass spectrometry (SIMS) data have shown that a small concentration (1-2%) of saccharin at the grain boundaries prevented neighboring Ni grains from bonding during the growth stage; hence, leading to the formation of voids at the grain boundaries. This served to create a structure that was associated with compressive stress rather than tensile stress [64], which is typically the case for saccharin free baths. These voids might cause further dimple rupture fracture [65]. However, it has been reported that sulfur introduced to nickel may initiate inter-granular embrittlement following the annealing treatment [66].

It has been reported that sodium saccharin in Watts bath, reduces the internal stress below the threshold that is required for recrystallization [67]. However, presence of saccharin, in supercritical CO_2 containing [92] electrolyte while electrodepositing Ni in Watts solution, was not effective in reducing either the grain size or internal tensile stress. In another study, it was shown that in nanocrystalline Ni deposits, the micro-strain increased with grain size reduction [44] through the use of saccharine.

2.3.3 Effect of hydrogen

The use of Kinetic Monte Carlo (KMC) simulations of hydrogen atom (as impurities) effects on Ni (110) and Ni (100) growth have shown [68] that it may catalyze the formation of larger Ni (100) islands. It can also accelerate the breakdown of 3D Ni islands during epitaxial growth. Due to the presence of H atoms [67], Ni (100) has a flattened surface, in contrast to Ni (110), which exhibits layer by layer growth with or without the presence of H atoms.

2.3.4 Effect of NO_2^-

The schematic effect of the presence of NO_2^- on Ni deposition, on a vitreous carbon electrode in sulfate solution (pH = 6) is presented in Figure 2.4 [69]. Based on the deposition potential and NO_2^- concentration, this mechanism can differ. At low concentrations and potentials, Ni^{2+} adsorption on active sites of the substrate is destabilized by the preferential adsorption of NO_2^-, rather than OH-groups. The formation and growth of some nuclei on the surface accompanied by $Ni(OH)_2$ adsorption, caused by NO_2^- or its reduction product, acts to hinder passivation. Another reason is the formation of amino-complexes with NH_3 (final product of NO_2^-), which increases the Gibbs nucleation activation energy.

At high NO_2^- concentrations, local alkalization takes place prior to deposition. Due to decreased Ni^{2+} activity, deposition begins with the reduction of $Ni(OH)_2$, adsorbed on the active sites of the electrode. Through the formation of initial Ni deposits, reduction enhances and further deposition is diffusion controlled by this $Ni(OH)_2$ layer. Subsequently, the passivation of growing crystals occurs via $Ni(OH)_2$ adsorption and a thin oxide layer formation, due to the localized alkaline environment.

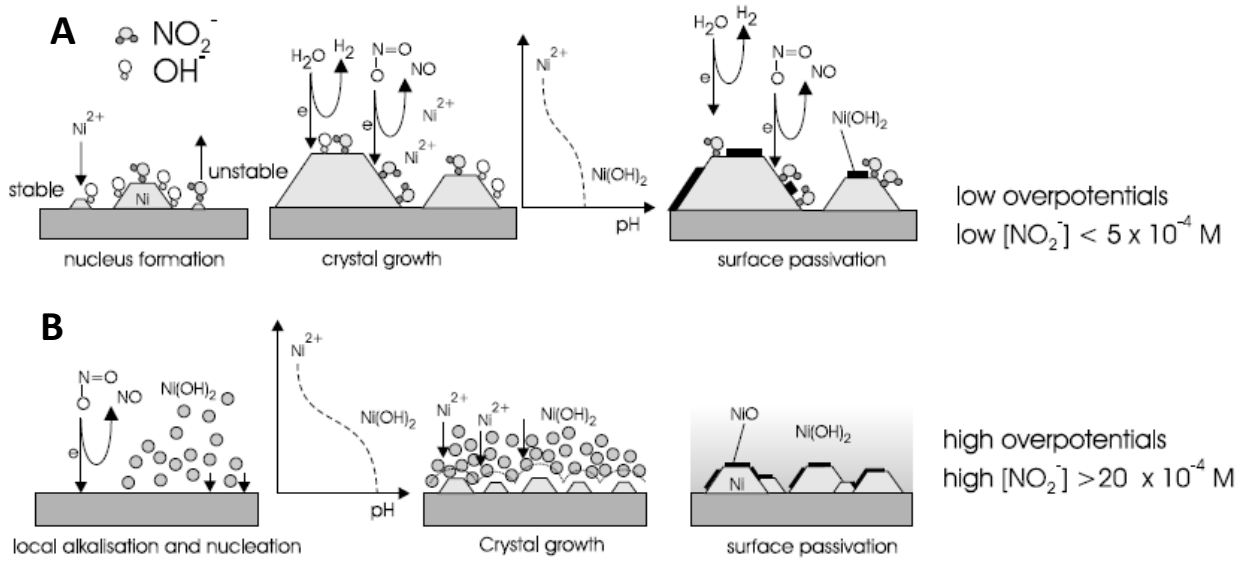

Figure 2.4 Schematic effect of the presence of NO_2^- on Ni deposition on a vitreous carbon electrode; (A) inhibition of passivation and nucleation due to presence of low NO_2^- concentrations at low overpotentials, (B) precipitation of a $Ni(OH)_2$ due to strong localized alkalization as a result of NO_2^- reduction at high overpotentials and concentrations of $NO_2^- > 5 \times 10^{-4}$ M. Image reproduced from reference [68] with permission. Copyright 2003, Elsevier.

2.4 Applications

2.4.1 Batteries

There is an ever-increasing demand for high performance power sources that possess high energy and power densities, while being lightweight, ultrathin, flexible, cost effective, and environmentally compatible. Batteries, particularly rechargeable batteries, have garnered significant attention as a source of energy over the last decade due to the high demand for portable devices. They operate based on an electrochemical reaction between two electrode materials in an electrolyte in a reversible manner. Much research has been focused on improving conventional batteries by enhancing their capacity, lifespan, increasing their charging speed, minimizing safety

issues, etc. In contrast to reversible intercalation/deintercalation chemistry for aqueous alkali-ion batteries and metal ion batteries, nickel/metal batteries are based primarily on faradaic reactions that involve one or multiple electron reactions on electrode materials [70]. Nickel-rich systems ($LiNi_xM_{1-x}O_2$; M = Mn, Co, and Al; $x > 0.5$) are considered as promising candidates to meet such requirements, although their structural degradation and thermal instability pose challenging bottlenecks [71]. Numerous electrochemical redox couples have been explored for their utility in rechargeable alkaline nickel/metal batteries, inclusive of nickel/cadmium, nickel/zinc, nickel/cobalt, and nickel/iron. Among these, aqueous Ni/Fe batteries are particularly favorable as (i) both Ni and Fe active materials are insoluble in alkaline solution and have no requirement for a separator (in contrast to Ni/Zn and Ag/Zn batteries); (ii) both Ni and Fe are earth-abundant elements and exhibit low toxicity or corrosive effects. Recently, novel flexible Ni/Fe cells [72] (Figure 2.5) have demonstrated superior energy and power densities stemming from the nanoscale features of active materials, and the hierarchical structure of the electrodes. Stable capacities on repeated bending and excellent longevity (up to 2000 cycles) have been demonstrated [70].

The structural and thermal instability of Ni-rich cathode materials has been an issue [71]; hence, surface modifications such as coating and core-shell structures have been investigated. Another persistent issue is pulverization due to constant volume changes during cycling, which results in poor cycling and the cracking of the electrode. Foam or mesh substrates for electrodes have been introduced [73, 74], where mainly Ni foams play a role as the substrate. Ni is also employed as a doping material [75]. One technique for increasing the cycling ability of electrodes is to decrease the particle size to the nanometric range, which results in additional capacity [76].

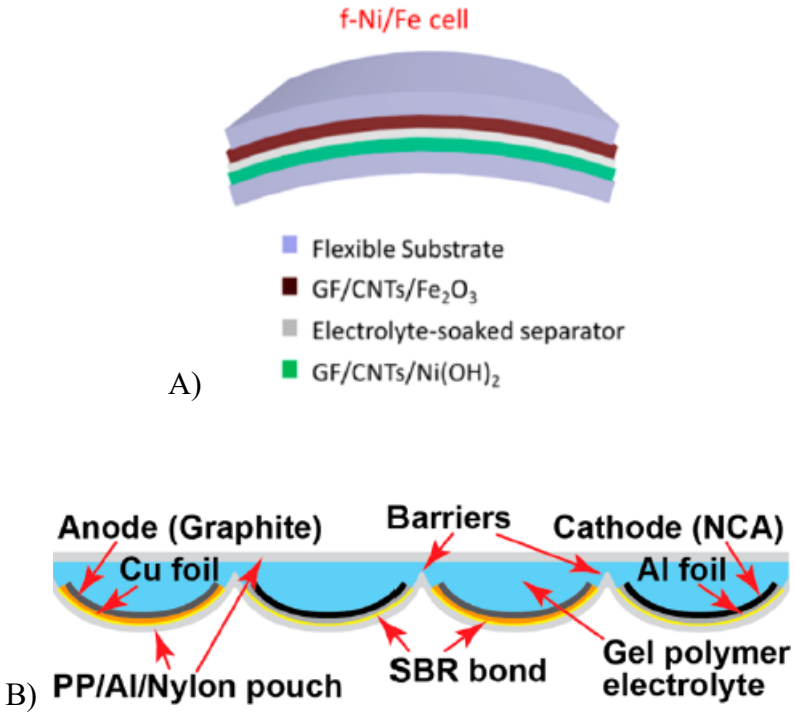

Figure 2.5 (A) The f-Ni/Fe cell structure, (B) interdigitated electrodes with pouch barriers between adjacent anodes and cathodes via the curved geometry of each electrode. Images reproduced from references [70] and [72] with permission. Copyright 2014 and 2015, American Chemical Society.

2.4.2 Fuel cells

Fuel cells are devices that generate energy by means of chemical reactions. They consume fuels such as methanol or hydrogen, which are oxidized to continuously produce electrons/electricity. However, they are very costly due to the use of expensive catalysts that are required for lowering the energy consumption/costs for the processes involved in energy production, such as the oxygen reduction reaction, methanol oxidation, fuel production (e.g., hydrogen). Nickel as a support, or in metal form, along with nickel oxide, have been widely used for catalytic purposes in the production of fuels such as urea [77, 78], formic acid [79], methanol [80] or ethanol electro-oxidation [81], hydrazine [82], hydrogen [83] or oxygen evolution [84, 85], or water splitting to be used in different types of fuel cells. Nickel in the form of oxide has been

used in conjunction with other oxides such as manganese oxide nanorods, and have demonstrated interesting electro-catalytic properties. Different supports have been employed for the electrocatalytic materials. Graphene comprises one of the most studied supports for various metal or composite [83] electrodes, which have shown improved performance compared to non-supported electrodes. This is thought to be due to a degree of intrinsic graphitization and the enhanced metal-support interactions of graphene. Nickel foam is another popular substrate that has offered superior supporting characteristics for various metals [81, 82], oxides [80], or hydroxides [86] in fuel cell-related fields.

Nickel catalysts have demonstrated both higher current densities and lower oxidation potentials, for the electro-oxidation of urea, than those of noble metal catalysts [87-88]; however, their efficiencies are inadequate. Nickel nanowires [77], nickel-cobalt bimetallic hydroxides [87], and nickel hydroxide [86] have been employed for hydrogen production as urea electro-oxidation catalysts, showing promising results and extended longevity toward replacing current electrocatalysts in this industry.

High operating temperatures present an additional issue with some types of fuel cells such as molten carbonate fuel cells (MCFCs), which have very highly efficient energy conversion capacities [89]. Since nickel oxide is very tolerant of moderately high temperatures, it is one of the most used cathodes for this type of fuel cell. However, modifications are required in order to increase catalyst longevity. Different surface modification methods, such as TiO_2- modified NiO, have been shown to improve this feature [89]. Reducing the working temperature is another method that might potentially decrease costs, while improving the durability of the materials by reducing oxidation levels. However, this calls for new materials with higher ion conductivity at lower temperatures to maintain high efficiencies [90, 91]. Once again, Ni and Ni based materials

such as a Ni-Al_2O_3 nanoparticle layer, as well as some Ni-Al or Ni-Cr anodes, have exhibited improved characteristics under such working conditions.

2.4.3 Supercapacitors

Supercapacitors have been the focus of increasing attention as novel energy storage devices due to their higher power density and longer cycling life, in comparison to conventional rechargeable batteries [92]. Electrochemical capacitors (EC) operate based on an electrochemical process in electrolytes. If the storage of energy occurs via an electrochemical Faradaic reaction, it is referred to as "pseudocapacitance". However, when the storage of energy relies on the non-Faradaic double layer process, it is categorized as "supercapacitance". Recently, it has been demonstrated that nanostructured electrodes for supercapacitors significantly decreased the diffusion time for ions and electrons, resulting in higher capacities and longer cycle times [93]. The performance of a supercapacitor is influenced by two key parameters: the surface area of the substrate, as well as the electron transport capacity of the active materials [94]. Amyriad of materials are under study, among which NiO and $Ni(OH)_2$ [95], RuO_2 [96], and Fe_2O_3 [97] are the most popular, with nickel hydroxide ($Ni(OH)_2$) being one of the most attractive candidates. This is due to its layered structure with large interlayer spacing, which offers a high theoretical specific capacitance [98]. The mixing of Ni with Co, or their oxides, has shown improved capacitances; therefore, they have been widely studied [97]. Nickel has been employed as a foam substrate [92, 97] and has shown significant improvements due to its high surface area. The use of conductive graphene has also been useful toward enhancing the performance of functional nickel hydroxide nanostructures by increasing conductivity [98].

2.4.4 Electrochemical sensors

Electrochemical sensing is based on an electrochemical redox reaction that occurs on the surface of an electrode, which results in a change in current and, hence, detection. The most important factors for sensors are selectivity and wide linear range, which accounts for the sensing concentration range, or sensitivity. Nickel has been successfully utilized in combination with organic and inorganic materials as electrochemical sensors for glucose [99], ascorbic acid [100], ethanol [101], NADH [102, 103], and H_2O_2 [104].

The most studied target has been electrochemical glucose sensing, which has achieved very promising results. Again, a method for increasing the signal of the sensor is through means of enhancing the surface area of the electrode, which is achieved by reducing the particle size to the nanoscale. Nickel hydroxide [105, 106] and nickel oxide [107, 108] are the most common forms of nickel that are used for sensing, which are successfully employed in combination with other materials such as Ni/NiO core-shell [108], boron doped diamond [109, 110], multi-walled carbon nanotubes [106], or graphene supported electrodes [107], to increase the durability, stability, and selectivity of the electrode.

2.5 Summary and perspectives

Nickel has found different applications in fuel cells, sensors and biosensors, catalysts and electrocatalysts over the last several years, most of which involve an electrochemical reaction in solution. Therefore, much research has been focused on the elucidation and prediction of the anodic dissolution behavior and deposition characteristics of nickel and its alloys. The dissolution steps and behavior of nickel, as well as factors that mediate its activity, such as structure, crystal

size, the presence and concentration of anions, as well as temperature in various media, was discussed towards a further understanding of corrosion and polishing procedures. Further, the electrodeposition of nickel and impacts of influential parameters, such as hydrogen evolution during the process, bath temperature, and presence of additives were discussed.

References

[1] M. Freitas, Nickel hydroxide powder for $NiO{\cdot}OH/Ni(OH)_2$ electrodes of the alkaline batteries, *J. Power Sources*, 2001, **93**, 163-173.

[2] I. G. Casella, M. Gatta, Electrodeposition and characterization of nickel-copper alloy films as electrode material in alkaline media, *J. Electrochem. Soc.*, 2002 , **149**, 465-471.

[3] K. Watanabe, T. Kikuoka, Physical and electrochemical characteristics of nickel hydroxide as a positive material for rechargeable alkaline batteries, *J. Appl. Electrochem.*, 1995, **25**, 219-226.

[4] K. I. Watanabe, M. Koseki, N. Kumagai, Effect of cobalt addition to nickel hydroxide as a positive material for rechargeable alkaline batteries, *J. Power Sources*, 1996, **58**, 23-28.

[5] J. Chen, D. H. Bradhurst, S. X. Dou, H. K. Liu, Nickel hydroxide as an active material for the positive electrode in rechargeable alkaline batteries, *J. Electrochem. Soc.*, 1999 , **146**, 3606-3612.

[6] S. C. Singhal, Advances in solid oxide fuel cell technology, *Solid State Ionics*, 2000, **135**, 305–313.

[7] W. Yang, S. Yang, W. Sun, G. Sun, Q. Xin, Nanostructured silver catalyzed nickel foam cathode for an aluminum–hydrogen peroxide fuel cell, *J. Power Sources*, 2006, **160**, 1420–1424.

[8] C. D. Iacovangelo, Stability of molten carbonate fuel cell nickel anodes, *J. Electrochem. Soc.*, 1986, **133**, 2410-2416.

[9] B. C. H. Steele, A. Heinzel, Materials for fuel-cell technologies, *Nature*, 2001, 414, 345-352.

[10] A. C. C. Tseung, S. Jasem, Oxygen evolution on semiconducting oxides, *Electrochemi. Acta*, 1977, **22**, 31-34.

[11] J. Gregori, J. J. Garcia-Jareno, F. Negrete, M. P. Pena, C. Sanz, J. Subiela, F. Vicente, Electrochemical dissolution and passivation of nickel powder randomly dispersed in a graphite+ polypropylene matrix, *J. Appl. Electrochem.*, 2007, **37**, 241-248.

[12] X. Wang, H. Luo, H. Yang, P. J. Sebastian, S. A. Gamboa, Oxygen catalytic evolution reaction on nickel hydroxide electrode modified by electroless cobalt coating*, Int. J. Hydrogen Energ.*, 2004, **29**, 967-972.

[13] V. Rashkova, S. Kitova, I. Konstantinov, T. Vitanov, Vacuum evaporated thin films of mixed cobalt and nickel oxides as electrocatalyst for oxygen evolution and reduction, *Electrochimi. Acta*, 2002, **47**, 1555–1560.

[14] M. Dinca, Y. Surendranath, D. G. Nocera, Nickel-borate oxygen-evolving catalyst that functions under benign conditions, *PNAS*, 2010 , **107**, 10337–10341.

[15] A. R. Sheik, M. K. Ghosh, K. Sanjay, T. Subbaiah, B. K. Mishra, Dissolution kinetics of nickel from spent catalyst in nitric acid medium, *J. Taiwan Inst. Chem. Engr.*, 2013, **44**, 34–39.

[16] B. Singh, Treatment of spent catalyst from the nitrogenous fertilizer industry-a review of the available methods of regeneration, recovery and disposal, *J. Hazard. Mater.*, 2009, **167**, 24–37.

[17] N. M. Al-Mansi, N. M. Abdel Monem, Recovery of nickel oxide from spent catalyst, *Waste Manage.*, 2002, **22**, 85-90.

[18] Y. kiIshida, K. Kumabe, K. Hata, K. Tanifuji, T. Hasegawa, K. Kitagawa, N. Isu, Y. Funahashi, T. Asai, Selective hydrogen generation from real biomass through hydrothermal reaction at relatively low temperatures, *Biomass Bioenerg.*, 2009, **33**, 8-13.

[19] K. K. Sahu, A. Agarwal, B. D. Pandey, Nickel recovery from spent nickel catalyst, *Waste Manage. Res.*, 2005, **23**, 145-154.

[20] M. Turner, G. E. Thompson, P. A. Brook, The anodic behaviour of nickel in sulphuric acid solutions, *Corros. Sci.*, 1973, **13**, 985-990.

[21] J. Gregori, J. J. Garcia-Jareno, D. Gimenez-Romero, F. Vicente, Kinetic calculations of the Ni anodic dissolution from EIS, *J. Solid State Electrochem.*, 2005, **9**, 83-90.

[22] D. Stoeckel, A. Pelton, T. Duerig, Self-expanding nitinol stents: material and design considerations, *Eur. Radiol.*, 2004, **14**, 292-301.

[23] C. L. Chu, R. M. Wang, T. Hu, L. H. Yin, Y. P. Pu, P. H. Lin, S. L. Wu, C. Y. Chung, K. W. K. Yeung, P. K. Chu, Surface structure and biomedical properties of chemically polished and electropolished NiTi shape memory alloys, *Mater. Sci. Eng. C*, 2008, **28**, 1430–1434.

[24] W. Simka, M. Kaczmarek, A. Baron-Wiechec, G. Nawrat, J. Marciniak, J. Zak, Electropolishing and passivation of NiTi shape memory alloy, *Electrochim. Acta*, 2010, **55**, 2437–2441.

[25] J. Gregori, J. J. Garcia-Jareno, F. Vicente, An approximate theoretical impedance analysis of the anodic dissolution of nickel across nickel (II) stabilised by means of competitive anions, *Electrochim. Acta*, 2007, **52**, 4062-4072.

[26] T. You, O. Niwa, Z. Chen, K. Hayashi, M. Tomita, S. Hirono, An amperometric detector formed of highly dispersed Ni nanoparticles embedded in a graphite-like carbon film electrode for sugar determination, *Anal. Chem.*, 2003, **75**, 5191–5196.

[27] H. Ayoub, V. Lair, S. Griveau, P. Brunswick, J. H. Zagal, F. Bedioui, M. Cassir, Electrochemical kinetics of anodic Ni dissolution in aqueous media as a function of chloride ion concentration at pH values close to physiological conditions, *Electroanal.*, 2012, **24**, 386-391.

[28] S. S. Mahshid, S. Mahshid, A. Dolati, M. Ghorbani, L. Yang, S. Luo, Q. Cai, Template-based electrodeposition of Pt/Ni nanowires and its catalytic activity towards glucose oxidation, *Electrochim. Acta*, 2011, **58**, 551–555.

[29] M. Itagaki, H. Nakazawa, L Watanabe, K. Noda, Study of dissolution mechanisms of nickel in sulfuric acid solution by electrochemical quartz crystal microbalance, *Corros. Sci.*, 1997, **39**, 901-911.

[30] N. Sato, G. Okamoto, Kinetics of the anodic dissolution of nickel in sulfuric acid solutions, *J. Electrochem. Soc.*, 1964, **111**, 897-903.

[31] S. G. Real, J. R. Vilche, A. J. Arvia, The characteristics of the potentiodynamic potential/current profiles obtained with the Ni/0.5 N H_2SO_4 interface. A contribution to the mechanism of the electrode, *Corros. Sci.*, 1980, **20**, 563-586.

[32] M. R. Barbosa, J. A. Bastos, J. J. Garcia-Jareno, F. Vicente, Chloride role in the surface of nickel electrode, *Electrochim. Acta*, 1998, **44**, 957-965.

[33] J. Scherer, B. M. Ocko, O. M. Magnussen, Structure, dissolution, and passivation of Ni (111) electrodes in sulfuric acid solution: an in situ STM, X-ray scattering, and electrochemical study, *Electrochim. Acta* , 2003, **48**, 1169-1191.

[34] M. Keddam, H. Takenouti, N. Yu, Transpassive dissolution of Ni in acidic sulfate media: a kinetic model, *J. Electrochem. Soc.*, 1985, **132**, 2561-2566.

[35] M. Bojinov, T. Tzvetkoff, The influence of solution anion on the mechanism of transpassive dissolution of ferrous-and nickel-based alloys, *J. Phys. Chem. B*, 2003, **107**, 5101-5112.

[36] J. Davis, D. H. Vaughan, D. Stirling, L. Nei, R. G. Compton, Cathodic stripping voltammetry of nickel: sonoelectrochemical exploitation of the Ni (III)/Ni (II) couple, *Talanta*, 2002, **57**, 1045–1051.

[37] V. P. Razygraev, M. V. Lebedeva, Effect of products of nitric acid reduction on active dissolution and passivation of nickel, *Prot. Met. Phys. Chem. Surf.*, 2009, **45**, 771–776.

[38] S. M. Abd El Haleemand E. E. Abd El AAl, Electrochemical behavior of nickel in HNO_3 and the effect of chloride ions, *J. Mater. Eng. Perform.*, 2004, **13**, 784-792.

[39] Y. Y. Ko, Y. Y. Wang, C. C. Wan, Electrochemical dissolution of nickel-42 in acid electrolytes, *Mater. Sci. Eng. A*, 1991, **148**, 79-83.

[40] G. E. Badea, T. Badea, Electrochemical Behaviour of nickel in aqueous acetic acid solutions, *Revue Roumaine de Chimie*, 2008, **53**, 291-295.

[41] Q. Zhang, Y. Hua, Z. Zhou, Corrosion properties of copper, nickel, and titanium in alkylimidazolium chloroaluminate based ionic liquids, *Int. J. Electrochem. Sci.*, 2013, **8**, 10239-10249.

[42] K. D. Ralston, N. Birbilis, C. H. J. Davies, Revealing the relationship between grain size and corrosion rate of metals, *Scripta Mater.*, 2010, **63**, 1201–1204.

[43] Q. Li-yuan, L. Jian-she, J. Qing, Effect of grain size on corrosion behavior of electrodeposited bulk nanocrystalline Ni, *Trans. Nonferr. Met. Soc. China*, 2010, **20**, 82-89.

[44] R. Mishra, R. Balasubramaniam, Effect of nanocrystalline grain size on the electrochemical and corrosion behavior of nickel, *Corros. Sci.*, 2004, **46**, 3019–3029.

[45] N. Hara, K. Sugimoto, In situ analysis of passive and transpassive films on nickel by modulated UV-Visible reflection Spectroscopy, *Trans. Japan Inst. Met.*, 1983, **24**, 236-245.

[46] G. Cordeiro, O. R. Mattos, O. E. Barcia, L. Beaunier, C. Deslouis, B. Tribollet, Anodic dissolution of nickel in concentrated sulfuric acidic solutions, *J. Appl. Electrochem.*, 1996, **26**, 1083-1092.

[47] K. Deo, S. G. Mehendale, S. Venkatachalam, Electrochemical dissolution of nickel in sulphuric acid by alternating current, *J. Appl. Eelectrochem.*, 1976, **6**, 37-43.

[48] S. G. Real, M. R. Barbosa, J. R. Vilche, A. J. Arvia, Influence of chloride concentration on the active dissolution and passivation of nickel electrodes in acid sulfate solutions, *J. Elect. Soc.*, 1990, **137**, 1696-1702.

[49] A. B. Shein, O. S. Ivanova, R. N. Minkh, The effect of anions on the anodic dissolution of nickel silicide in sulfate electrolytes, *Prot. Met.*, 2008, **44**, 32–38.

[50] J. Gregori, J. J. Garcia-Jaren, D. Gimenez-Romero, A. Roig, F. Vicente, Anodic dissolution of nickel across two consecutive electron transfers calculation of the Ni (I) intermediate concentration, *J. Electrochem. Soc.*, 2007, **154**, 371-377.

[51] G. Beth-Nielsen, F. de Fontenay, H. Poulsen, Electrochemical and CMT measurements of the anomalous dissolution of nickel in solutions containing oxygen, *Electrochim. Acta*, 1997, **42**, 1847-1858.

[52] T. H. Nguyen, R. T. Foley, On the mechanism of pitting of aluminum, *J. Electrochem. Soc.*, 1979, **126**, 1855-1860.

[53] T. P. Hoar, D. C. Mears, G. P. Rothwell, The relationships between anodic passivity, brightening and pitting, *Corros. Sci.*, 1965, **5**, 279-289.

[54] U. Landau, Anodic dissolution of nickel single crystals in an acidic fluoride containing electrolyte, *Z. Metallk*, 2000, **91**, 854-862.

[55] T. Vasilache, S. Gutt, I. Sandu, V. Vasilache, G. Gutt, M. Risca, A. V. Sandu, Electrochemical mechanism of nickel and zinc-nickel alloy electrodeposition, *Recent Pat. Corros. Sci.*, 2010, **2**, 1-5.

[56] O. Aaboubi, J. Amblard, J.-P. Chopart, A. Olivier, A temperature and electrochemical impedance spectroscopy analysis of nickel electrocrystallization from a Watts solution, *J. Phys. Chem. B*, 2001, **105**, 7205-7210.

[57] J. Ji, W. C. Cooper, D. B. Dreisinger, E. Peters, Surface pH measurements during nickel electrodeposition, *J. Appl. Electrochem.*, 1995, **25**, 642-650.

[58] S. Zafeiratos, F. E. Paloukis, S. G. Neophytides, Nickel electrodeposition on a gold polycrystalline foil: a combined voltammetric and photoelectron spectroscopy study, *J. Phys. Chem. B*, 2004, **108**, 1371-1379.

[59] B. V. Tilak, A. S. Gendron, M. A. Mosoiu, Borate buffer equilibria in nickel refining electrolytes, *J. Appl. Electrochem.*, 1977, **7**, 495-500.

[60] V. C. Nguyen, C. Y. Lee, L. Chang, F. J. Chen, C. S. Lin, The relationship between nano crystallite structure and internal stress in Ni coatings electrodeposited by watts bath electrolyte mixed with supercritical CO_2, *J. Electrochem. Soc.*, 2012, **159**, 393-399.

[61] A. Damian, F. Maroun, P. Allongue, Electrochemical growth and dissolution of Ni on bimetallic Pd/Au (111) substrates, *Electrochim. Acta*, 2010, 55, 8087-8099.

[62] M. Wysocka-Zolopaa, E. Gradzkaa, K. Szymanskib, K. Winkler, Electrodeposition of nickel, cobalt, and iron on polypyrrole films, *Thin Solid Films*, 2013, **548**, 44-51.

[63] A. Bhandari, S. J. Hearne, B. W.Sheldon, S. K. Soni, Microstructural origins of saccharin-induced stress reduction in electrodeposited Ni, *J. Electrochem. Soc.*, 2009, **156**, 279-282.

[64] K. S. Kumar, S. Suresh, M. F. Chisholm, J. A. Horton, P. Wang, Deformation of electrodeposited nanocrystalline nickel, *Acta Materialia*, 2003, **51**, 387-405.

[65] J. W. Dini, H. R. Johnson, H. J. Saxton, Influence of sulfur content on the impact strength of electroformed nickel, *Electrodeposition Surf. Treat.*, 1974, **2**, 165-176.

[66] T. E. Buchheit, D. A. LaVan, J. R. Michael, T. R. Christenson, S. D. Leith, Microstructural and mechanical properties investigation of electrodeposited and annealed LIGA nickel structures, M*etall. Mater. T. A*, 2002, **33A**, 539-554.

[67] K. Haug, J. Jamoury, Kinetic Monte Carlo study of the effects of hydrogen on the 3-D epitaxial growth of Ni (100) and Ni (110), *J. Phys. Chem. B*, 2002, **106-119**, 11253-11263.

[68] A. G. Munoz, D. R. Salinas, Inhibitory effects of NO_2^- on Ni deposition, *J. Electroanal. Chem.*, 2003, **547**, 115-124.

[69] K. Wykpis, M. Popczyk, A. Budniok, Electrolytic deposition and corrosion resistance of Zn-Ni coatings obtained from sulphate-chloride bath, *Bull. Mater. Sci.*, 2011, **34**, 997–1001.

[70] J. Liu, M. Chen, L. Zhang, J. Jiang, J. Yan, Y. Huang, J. Lin, H. J. Fan, Z. X. Shen, A flexible alkaline rechargeable Ni/Fe battery based on graphene foam/carbon nanotubes hybrid film, *Nano Lett*., 2014, **14**, 7180−7187.

[71] H. Kim, M. G. Kim, H. Y. Jeong, H. Nam, J. Cho, A new coating method for alleviating surface degradation of $LiNi_{0.6}Co_{0.2}Mn_{0.2}O_2$ cathode material: nanoscale surface treatment of primary particles, *Nano Lett.*, 2015, **15**, 2111−2119.

[72] J. S. Kim, D. Ko, D. J. Yoo, D. S. Jung, C. T. Yavuz, N. I. Kim, I. S. Choi, J. Y. Song, J. W. Choi, A half millimeter thick coplanar flexible battery with wireless recharging capability, *Nano Lett*., 2015, **15**, 2350-2357.

[73] P. Nithyadharseni, M.V. Reddy, B. Nalini, B.V.R. Chowdari, Electrochemical investigation of SnSb nano particles for lithium-ion batteries, *Mater. Lett*., 2015, **150**, 24–27.

[74] Q. Zhao, X. Hu, K. Zhang, N. Zhang, Y. Hu, J. Chen, Sulfur nanodots electrodeposited on Ni foam as high-performance cathode for Li–S batteries, *Nano Lett*., 2015, **15**, 721−726.

[75] N. Wan, T. Zhao, S. Sun, Q. Wu, Y. Bai, Nickel and nitrogen co-doped tin dioxide nano-composite as a potential anode material for lithium-ion batteries, *Electrochim. Acta*, 2014, **143**, 257–264.

[76] Y. N. Nuli, S. L. Zhao, Q. Z. Qin, Nanocrystalline tin oxides and nickel oxide film anodes for Li-ion batteries, *J. Power Sources*, 2003, **114**, 113-120.

[77] F. Guo, K. Ye, K. Cheng, G. Wang, D. Cao, Preparation of nickel nanowire arrays electrode for urea electro-oxidation in alkaline medium, *J. Power Sources*, 2015, **278**, 562-568.

[78] W. Yan, D. Wang, L. A. Diaz, G. G. Botte, Nickel nanowires as effective catalysts for urea electro-oxidation, *Electrochim. Acta*, 2014, **134**, 266–271.

[79] M. K. Kumar, N. S. Jha, S. Mohan, S. K. Jha, Reduced graphene oxide-supported nickel oxide catalyst with improved CO tolerance for formic acid electrooxidation, *Int. J. Hydrogen Energ*., 2014, **39**, 12572-12577.

[80] S. Sun, Z. J. Xu, Composition dependence of methanol oxidation activity in nickel–cobalt hydroxides and oxides: an optimization toward highly active electrodes, *Electrochim. Acta*, 2015, **165**, 56–66.

[81] C. Zhou, X. Wang, X. Jia, H. Wang, C. Liu, Y.Yang, Nanoporous platinum grown on nickel foam by facile plasma reduction with enhanced electro-catalytic performance, *Electrochem. Comm*., 2012, **18**, 33-36.

[82] B. Filanovsky, E. Granot, I. Presman, I. Kuras, F. Patolsky, Long-term room-temperature hydrazine/air fuel cells based on low-cost nanotextured Cu–Ni catalysts, *J. Power Sources*, 2014, **246**, 423-429.

[83] K. Xiong, L. Li, L. Zhang, W. Ding, L. Peng, Y. Wang, S. Chen, S. Tan, Z. Wei, Ni-doped Mo_2C nanowires supported on Ni foam as a binder-free electrode for enhancing the hydrogen evolution performance, *J. Mater. Chem*. *A*, 2015, **3**, 1863–1867.

[84] A. C. Garcia, F. H. B. Lima, E. A. Ticianelli, M. Chatenet, Carbon-supported nickel-doped manganese oxides as electrocatalysts for the oxygen reduction reaction in the presence of sodium borohydride, *J. Power Sources*, 2013, **222**, 305-312.

[85] D. K. Bediako, B. Lassalle-Kaiser, Y. Surendranath, J. Yano, V. K. Yachandra, D. G. Nocera, Structure–activity correlations in a nickel–borate oxygen evolution catalyst, *J. Am. Chem. Soc*., 2012, **134**, 6801−6809.

[86] V. Vedharathinam, G. G. Botte, Direct evidence of the mechanism for the electro-oxidation of urea on $Ni(OH)_2$ catalyst in alkaline medium, *Electrochim. Acta*, 2013, **108**, 660–665.

[87] W. Yan, D. Wang, G. G. Botte, Nickel and cobalt bimetallic hydroxide catalysts for urea electro-oxidation, *Electrochim. Acta*, 2012, **61**, 25–30.

[88] K. Ye, D. Zhang, F. Guo, K. Cheng, G. Wang, D. Cao, Highly porous nickel@carbon sponge as a novel type of three-dimensional anode with low cost for high catalytic performance of urea electro-oxidation in alkaline medium, *J. Power Sources*, 2015, **283**, 408-415.

[89] H. S. Choi, K. Kim, C. W. Yi, A simple surface modification of NiO cathode with TiO_2 nano-particles for molten carbonate fuel cells (MCFCs), *Bull. Korean Chem. Soc*., 2014, **35**, 1237-1240.

[90] H. V. P. Nguyen, M. R. Othman, D. Seo, S. P. Yoon, H. C. Ham, S. W. Nam, J. Han, J. Kim, Nano Ni layered anode for enhanced MCFC performance at reduced operating temperature, *Int. J. Hydrogen Energ*., 2014, **39**, 12285-12290.

[91] C. H. A. Tsang, K. N. Hui, K. S. Hui, L. Ren, Deposition of Pd/graphene aerogel on nickel foam as a binder-free electrode for direct electro-oxidation of methanol and ethanol, *J. Mater. Chem. A*, 2014, **2**, 17986–17993.

[92] X. Xiong, D. Ding, D. Chen, G. Waller, Y. Bu, Z. Wang, M. Liu, Three-dimensional ultrathin $Ni(OH)_2$ nanosheets grown on nickel foam for high-performance supercapacitors, *Nano Energy*, 2015, **11**, 154–161.

[93] C. An, Y. Wang, Y. Huang, Y. Xu, L. Jiao, H. Yuan, Porous $NiCo_2O_4$ nanostructures for high performance supercapacitors via a microemulsion technique, *Nano Energy*, 2014, **10**, 125–134.

[94] J. Li, J. Xiao, Z. Wang, Z. Wei, Y. Qiu, S. Yang, Construction of bicontinuously porous Ni architecture as a deposition scaffold for high performance electrochemical supercapacitors, *Nano Energy*, 2014, **10**, 329–336.

[95] M. Li, S. Xu, Y. Zhu, Y. Xu, P. Yang, L. Wang, P. K. Chu, Three-dimensional nanoscale Co_3O_4 electrode on ordered Ni/Si microchannel plates for electrochemical supercapacitors, *Mater. Lett*., 2014, **132**, 405-408.

[96] J. Y. Kim, K. H. Kim, H. K. Kim, S. H. Park, K. C. Roh, K. B. Kim, Template-free synthesis of ruthenium oxide nanotubes for high-performance electrochemical capacitors, *ACS. Appl. Mater. Interfaces*, 2015, **7**, 16686-16693.

[97] A. K. Singh, D. Sarkar, G. Gopal Khan, K. Mandal, Designing one dimensional Co-Ni/Co_3O_4-NiO core/shell nano-heterostructure electrodes for high-performance pseudocapacitor, *Appl. Phys. Lett*., 2014, **104**, 133904.

[98] J. Zhu, S. Chen, H. Zhou, X. Wang, Fabrication of a low defect density graphene-nickel hydroxide nanosheet hybrid with enhanced electrochemical performance, *Nano Res*., 2012, **5**, 11-19.

[99] C. Y. Ko, J. H. Huang, S. Raina, W. P. Kang, A high performance non-enzymatic glucose sensor based on nickel hydroxide modified nitrogen-incorporated nanodiamonds, *Analy*., 2013, **138**, 3201-3208.

[100] X. Liu, X. Li, Y. Xiong, Q. Huang, X. Li, Y. Dong, P. Liu, C. Zhang, A glassy carbon electrode modified with the nickel (II)-bis (1, 10-phenanthroline) complex and multi-walled carbon nanotubes, and its use as a sensor for ascorbic acid, *Microchim. Acta*, 2013, **180**, 1309–1316.

[101] S. Blanco, R. Vargas, J. Mostany, C. Borras, B. R. Scharifker, A novel nickel nanowire amperometric sensor: Direct current vs. alternating current strategies for ethanol, acetaldehyde and acetylcholine detection, *J. Electroanal. Chem*., 2015, **740**, 61–67.

[102] E. Sharifi, A. Salimi, E. Shams, Electrocatalytic activity of nickel oxide nanoparticles as mediatorless system for NADH and ethanol sensing at physiological pH solution, *Biosens. Bioelectron*., 2013, **45**, 260–266.

[103] M. Govindhan, M. Amiri, A. Chen, Au nanoparticle/graphene nanocomposite as a platform for the sensitive detection of NADH in human urine, *Biosens. Bioelectron*. 2015, **66**, 474-480.

[104] S. Lata, B. Batra, N. Karwasra, C. S. Pundir, An amperometric H_2O_2 biosensor based on cytochrome c immobilized onto nickel oxide nanoparticles/carboxylated multiwalled carbon nanotubes/polyaniline modified gold electrode, *Proc. Biochem*., 2012, **47**, 992–998.

[105] N. Qiao, J. Zheng, Nonenzymatic glucose sensor based on glassy carbon electrode modified with a nanocomposite composed of nickel hydroxide and graphene, *Microchim. Acta*, 2012, **177**, 103-109.

[106] A. Sun, J. Zheng, Q. Sheng, A highly sensitive non-enzymatic glucose sensor based on nickel and multi-walled carbon nanotubes nanohybrid films fabricated by one-step co-electrodeposition in ionic liquids, *Electrochim. Acta*, 2012, **65**, 64–69.

[107] S. Liu, B. Yu, T. Zhang, A novel non-enzymatic glucose sensor based on NiO hollow spheres, *Electrochim. Acta*, 2013, **102**, 104–107.

[108] L. Wang, Z. Lu, Q. Cheng, L. Liu, Three-dimensional nickel-nickel oxide core-shell nanorod array for nonenzymatic glucose sensing, *Anal. Lett*., 2015, **48**, 1854-1864.

[109] Z. Deng, H. Long, Q. Wei, Z. Yu, B. Zhou, Y. Wang, L. Zhang, S. Li, L. Ma, Y. Xie, J. Min, High-performance non-enzymatic glucose sensor based on nickel-microcrystalline graphite-boron doped diamond complex electrode, *Sensor. Actuat. B*, 2017, **242**, 825-834.

[110] K. E. Toghill, L. Xiao, M. A. Phillips, R. G. Compton, The non-enzymatic determination of glucose using an electrolytically fabricated nickel microparticle modified boron-doped diamond electrode or nickel foil electrode, *Sensor. Actuat. B*, 2010, **147**, 642–652.

Chapter 3: Materials and Methods

3.1 Introduction

This chapter briefly discusses the various instrumentation and techniques that were employed in the characterization and electrochemical studies of nickel and nickel-based materials. The applied synthesis methods for the fabrication of the electrodes are also presented.

3.2 Experimental

3.2.1 Materials

$NiSO_4.6H_2O$, $NiCl_2.6H_2O$, and H_3BO_3 were of analytical grade and were purchased from Aldrich. Analytical grade graphene oxide (4 mg mL^{-1}), Nafion (10%), ammonium chloride (NH_4Cl, $\geq$ 99.5%), and potassium hydroxide were purchased from Sigma-Aldrich. Iridium chloride ($IrCl_3 \cdot 3H_2O$) was obtained from Pressure Chemical Corp. All chemicals were used as received without any further purification.

For the anodic nickel dissolution experiments, electrolytic Ni chip samples of more than 99% purity and almost identical in weight were obtained from Vale Canada and used as working electrodes for the experiments in as-received condition. Titanium wires were used for electrical connections, while the connected area was covered with Teflon tape in order to prevent dissolution beneath the connection and potential premature disconnection during the experiment. Titanium plates were of commercially available grade. Nickel plates used as a substrate for nickel deposition were purchased from Alfa-Aesar (99.5% pure) and were cut into 1 cm x 1 cm squares.

Deionized distilled water (18.2 MΩ cm) employed for the preparation of the aqueous solutions was purified with a NANOpure® DiamondTM water system.

Strong basic macroreticular anion exchanger membrane (Amberlite IRA900RF Cl) was purchased from Rohm and Haas Co.

3.2.2 Characterization

Surface morphology investigations were conducted using a Hitachi SU-70 scanning electron microscopy (SEM) equipped with energy dispersive spectroscopy (EDS), which was employed for elemental analysis of the residue at the end of anodic dissolution process. X-ray diffraction (XRD) patterns were recorded using a Pananalytical X'pert Pro Diffractometer with Ni filtered monochromatic Cu Kα (1.5406 Å, 2.2 KW Max.) radiation, and the patterns were analyzed using X'pert HighScorePlus software. The diffracted X-ray intensities were recorded in the 2θ range from 10° to 100°. Infrared spectroscopy (FTIR) and X-ray photoelectron spectroscopy (XPS), were also employed for surface characterization. XPS measurements were carried out where the takeoff angle as relates to the horizontal surface was 90°, and a monochromatic Al Kα X-ray source of 400 μm spot size was used. Charge compensation was measured, and the spectrum was corrected using the position of main C1s peak (C–C) at 284.6 eV, and XPSpeak software was used for the deconvolution of the spectra.

The dissolution of Ni was quantitatively recorded with inductively coupled plasma atomic emission spectroscopy (ICP-AES) using a Varian Vista Pro CCD with a CETAC ASX-510 Auto Sampler.

3.2.2 Electrochemical studies

Electrochemical experiments were carried out with a VoltaLab 40 (PGZ301 & VoltaMaster 4) for short-term studies, and an Arbin Instruments (MSTAT, USA) potentiostat/galvanostat for long-term studies using a conventional one-compartment three-electrode cell. A Solartron SI 1287 equipped with a frequency response analyzer (1252A) was employed for electrochemical impedance spectroscopy (EIS) and galvanostatic charge/discharge. The reference electrode for long-term anodic dissolution studies was comprised of Ni, whereas Ag/AgCl was used for the remainder of the studies. Further, Ti plates were employed as a counter electrode for long term studies, while a coil shaped Pt wire was used for the remainder of the electrochemical experiments. The platinum wire was quenched prior to use. A summary of the electrochemical methods used in the present work are as following:

1. Charge/discharge: An electrochemical method for investigating the charge storage behavior of a material by measuring the potential response of the electrode vs. time at a constant current (by altering between anodic/cathodic currents) in a specific potential window.

2. Chronoamperometry (CA): An electrochemical technique where a constant potential is applied to the working electrode and the response current density is measured vs. time.

3. Chronopotentiometry (CP): An electrochemical technique where a constant current density is applied to the working electrode and the response potential is measured vs. time.

4. Cyclic voltammetry: An electrochemical technique to study the oxidation and reduction of the species in the electrolyte where the current response at the electrode is measured over time while the potential of the working electrode is ramped linearly to a certain potential and back to the initial potential in a cycle.

5. Electrochemical impedance spectroscopy (EIS): An electrochemical technique where the resistance of an electrochemical setup can be studied by measuring the current response at a constant applied AC potential where the frequency is varied in a specified range. Using an equivalent circuit one can infer the elements such as resistance and capacitance present in the system.

6. Linear sweep voltammetry (LSV): In order to study the oxidation or reduction of species, this voltammetric technique is used where the current response at the electrode is measured while the potential of the working electrode is swept linearly.

7. Polarization curve: The plot of current density vs. potential, which is used for electrochemical studies of the reaction kinetics on the electrode. Even though the potential is the independent variable, it is very common in electrochemistry field for polarization curve to be plotted E vs. log |i| format.

3.2.4 Synthesis and electrolyte preparation

3.2.4.1 Preparation of Watts solution for anodic dissolution of nickel

Watts bath was prepared by mixing 300 g L^{-1} of $NiSO_4.6H_2O$, 35-45 g L^{-1} of $NiCl_2.6H_2O$, and 40 g L^{-1} of boric acid. The temperature of the solution was set to 55.0 ± 0.2 ^oC and constantly maintained using with a circulating water thermostat (Thermo Scientific). All solutions were made fresh for every experiment.

Residue collection at the conclusion of the experiments was carried out by means of a centrifuge device by Thermo Electron Corporation (Biofude Startos).

For short-term anodic dissolution studies, electrolytic Ni materials (Thompson Ni sample, Vale Canada) connected with Cu-wire, were embedded in a Teflon holder with an exposed area of 1.0 cm^2 and used as working electrodes. They were polished using 240, 400, and 600 mesh SiC powder, followed by finely polishing with variously sized diamond suspensions (9.0, 3.0, 1.0, and 0.05 μm), and finally sonicated in pure water.

3.2.4.2 Synthesis of nickel hydroxide/carbon nitride/reduced graphene oxide

The fabrication of the NCG nanocomposite was achieved by casting the precursors from a stock solution onto a GCE, following the in situ electrochemical reduction of GO and Ni precursors. The g-C_3N_4 sample was prepared using a facile combustion method, as described in our previous study [1]. The GCE surface was polished with alumina powder (0.5 μm) followed by sonication in pure water for 1 min. A 100 μL mixture of GO (0.25 mg mL^{-1}), $NiCl_2.6H_2O$ (5-15 mM), g-C_3N_4 (0.5 mg mL^{-1}), and Nafion (10%) was cast onto the GCE and then allowed to air dry. All electrochemical procedures were done using three-electrode setup with Pt as the counter electrode and Ag/AgCl as reference electrodes.

The *in-situ* formation of the nanocomposites on the GCE was achieved using cyclic voltammetry (CV) performed in 0.1 M KOH by running 20 cycles within the reducing electrode potential of from between 0.765 V and -0.035 V (vs. RHE) at a 10 mV s^{-1} scan rate. For comparison purposes, electrodes consisting of only $Ni(OH)_2$, C_3N_4/rGO (CG), $Ni(OH)_2/C_3N_4$ (NC), $Ni(OH)_2$/rGO (NG), and $Ni(OH)_2/C_3N_4$/rGO with various concentrations of Ni were prepared using the identical electrochemical approach.

3.2.4.3 Synthesis of nickel oxide supported iridium oxide

Prior to electrodeposition, a nickel foil purchased from Alfa-Aesar (purity: 99.5%; thickness: 0.5 mm) was cut into small pieces (1.0 cm x 1.0 cm), cleaned via sonication in acetone, and rinsed using double-distilled water. The electrodeposition of the 3D porous nickel electrodes was carried out in a 2.0 M NH_4Cl + 0.1 M $NiCl_2$ solution under two different current densities of 1.5 and 3.0 A cm^{-2} over different time intervals of 75, 100, and 150 s using Arbin Instruments (MSTAT, USA) potentiostat/galvanostat. The 3D porous Ni electrode prepared at 3.0 A cm^{-2} for 150 s was selected to be modified with various loadings of a 0.1 M iridium chloride precursor, where the loaded iridium amounts were 3.0, 7.0, 10.0, and 15.0 wt.% of the 3D porous Ni that was electrodeposited on the Ni plate. For clarification, the prepared samples were denoted as NiIr(3%)Ox, NiIr(7%)Ox, NiIr(10%)Ox, and NiIr(15%)Ox, respectively. Following air drying, the cast electrodes, including a 3D porous nickel electrode (as the control electrode), were annealed at 450 ^{o}C for 3 h in an air furnace.

References

[1] S. K. Konda, M. Amiri, A. Chen, Photoassisted deposition of palladium nanoparticles on carbon nitride for efficient oxygen reduction, *J. Phys. Chem. C*, 2016, **27**, 14467-14473..

Chapter 4: Anodic Dissolution of the Electrolytic Ni Electrode in Watts Solution

4.1 Introduction

Nickel (Ni) is of great importance due to its technological applications, particularly in rechargeable alkaline batteries [1], cathodes for fuel cells [2] and electrocatalysts for oxygen evolution reactions [3]. Furthermore, to increase corrosion resistance Ni is added to the composition of many alloys [4-6]. It has been the topic of many electrochemical studies as relates to electrochemical dissolution and passivation processes in various electrolytes for industrial applications [7-9]. In particular, electrolytic Ni has attracted a great deal of attention due to the strategic and industrial importance of nickel in various fields including transportation, service apparatus, petroleum, power generation, and catalysis [10]. Approximately 45% of the global production of Ni is generated through electrorefining and electrowinning processes, whereas the remaining available Ni is derived from sulfide ores and lateritic sources [11, 12]. More than 150 years ago, the initial electrodeposition of Ni was successfully carried out [13]. For industrial purposes, the Watts bath, which contains chloride and nickel sulfate salts, was first introduced in 1916 and is still widely used [14]. Generally, Ni electrochemical dissolution proceeds via two single electron transfer steps that are followed by a transport step in acidic medium [15, 16]. The appearance of single or double voltammetric anodic peaks defines the active anodic dissolution/passive transition of nickel in acidic media [17]. Several studies have demonstrated the electrochemical dissolution of Ni in acidic [18] and basic [19] media. The electrochemical behavior of a Ni electrode in acidic media is contingent on the design of the electrode, as well as the composition of the electrolyte [20, 21]. It is possible for pitting-like dissolution to occur on Ni,

where aggressive ions are present and their concentration and the applied overpotential exceed certain threshold values [22].

In general, dissolution inhibition may occur due to the formation of a passive layer on the Ni surface, which is a result of active anodic dissolution. The formation of an oxy-hydroxide layer on the Ni surface protects it from subsequent dissolution. However, the presence of certain chloride ions can destroy the layer at local sites, which leads to localized dissolution and pitting [23, 24]. Muñoz et al. [25] studied the effects of nitrate ions on the dissolution of Ni in acid phosphate solutions by means of potentiodynamic scans and impedance spectroscopy under electrode rotation. They reported that the nitrate ions prompted an increase in the rate of active Ni dissolution through a lower NiOH surface coverage, which hindered the formation of the pre-passive layer at low pH-values, and increasing the passivation current by preferential adsorption against passivating species, such as NiOH and $Ni(OH)_2$. Krug et al. [26] have reported real-time surface X-ray scattering studies of electrochemical dissolution at technologically relevant rates, using metal electrodes in acidic chloride-containing solutions. They also demonstrated that surface roughness can play a significant role on the mechanism of the observed electrochemical dissolution of gold.

The aim of the present investigation was to elucidate and understand the changes in surface morphology, crystallinity, electrochemical behaviors, and residue formation during the anodic dissolution of an electrolytic Ni electrode. To this end, we systematically analyzed several aspects of the electrochemical dissolution of an electrolytic Ni electrode related to the surface changes occurring during its dissolution in Watts solution. Hence, detailed knowledge of this process would allow for an improved understanding of the dissolution behavior of the electrolytic Ni in Watts solution for industrial refinery applications.

4.2 Experimental

4.2.1 Materials

$NiSO_4.6H_2O$, $NiCl_2.6H_2O$, and H_3BO_3 were obtained from industrial samples. A Watts-type bath solution was prepared, which contained 300 g L^{-1} of $NiSO_4.6H_2O$, 35 g L^{-1} of $NiCl_2.6H_2O$, and 40 g L^{-1} of H_3BO_3. All other analytical grade reagents were used as received. Double distilled water, purified with a Nanopure® water system was used in the preparation of all solutions. The solution temperature was controlled with a circulating water thermostat (Thermo Scientific). A strong basic macroreticular anion exchange resin (Amberlite IRA900RF Cl) was purchased from Rohm and Haas Co for the ICP-AES studies.

Electrolytic Ni materials (Thompson Ni sample, Vale Canada) connected to a Cu-wire and embedded in a Teflon mount with an exposed area of 1.0 cm^2, were used as working electrodes. First, mounted electrolytic Ni samples were polished using 240, 400, and 600 grit SiC powders. After achieving a uniform surface, they were finely polished with various sizes of diamond suspensions (9.0, 3, 1, and 0.05 μm) using a polishing cloth. Finally, they were sonicated in acetone and pure water.

4.2.2. Instrumentation

Surface morphology studies were performed using a Hitachi SU-70 scanning electron microscopy (SEM). X-ray diffraction (XRD) patterns were recorded with a Pananalytical X'pert Pro Diffractometer, which was equipped with a Ni filtered monochromatic Cu Kα (1.5406 Å, 2.2 KW Max.) radiation. The diffracted X-ray intensities were recorded in the 2θ range of from 20° to 100°. The dissolution of Ni was quantitatively recorded employing an analysis of the electrolyte

via inductively coupled plasma-atomic emission spectroscopy (ICP-AES) using a Varian Vista Pro CCD with a CETAC ASX-510 Auto Sampler. Electrochemical experiments were carried out by means of a VoltaLab 40 (PGZ301 & VoltaMaster 4) using a conventional one-compartment three-electrode cell. An electrolytic Ni electrode was employed as the working electrode (electrode area: ~1 cm^2), a silver/silver chloride electrode (Ag/AgCl) as the reference electrode, and a titanium plate (Ti) as the counter electrode. Electrochemical measurements such as cyclic voltammetry and electrochemical impedance spectroscopy were performed. The applied current densities for electrochemical dissolution were 4.0, 8.0, and 16.0 mA cm^{-2} and the electrolyte used was Watts solution.

4.3 Results and discussion

4.3.1. Surface morphology and crystalline nature of the electrolytic Ni electrode

Figure 4.1A displays the SEM images of the polished electrolytic Ni electrode. The microstructure grain boundaries can be easily seen in the high-magnification image, as depicted in the inset of Figure 4.1A. Figure 4.B shows the energy dispersive X-ray (EDS) spectrum of the electrolytic Ni electrode. The EDS spectrum revealed that Ni was predominantly present at the electrode surface, along with small amounts of environmental carbon and oxygen species. In addition, elemental mapping of the electrode was recorded and shown in the inset of Figure 4.1B. Primarily, there was only elemental Ni present in the mapping analysis. It was very difficult to locate the presence of small amounts of any other metallic impurities at the electrode surface.

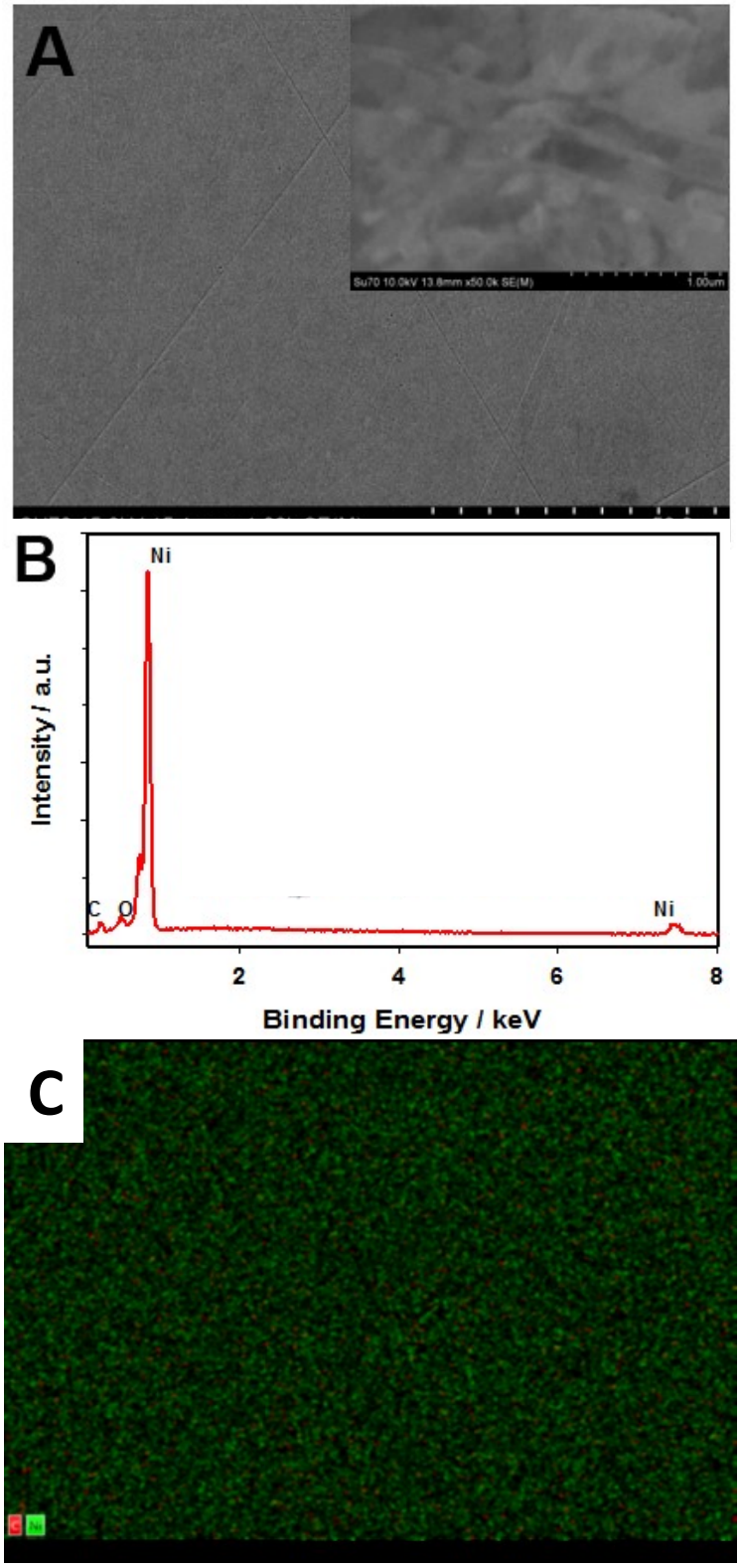

Figure 4.1 (A) SEM images (inset: high-magnification image), (B) EDS spectrum of the polished electrolytic Ni, and (C) Elemental mapping of the Ni (green dots) and O (red dots)).

To further investigate the crystalline nature of the electrolytic Ni electrode, the X-ray diffraction pattern (XRD) spectrum was recorded and is presented in Figure 4.2A. The XRD pattern of the electrolytic Ni revealed a number of peaks at 44.4, 51.7, 76.2, and 92.8° corresponding to (111), (200), (220), and (311) planes, respectively, of the face-centered cubic lattice. The XRD pattern as shown in Figure 4.2A matched with that of Ni in the JCPDS database (JCPDS PDF: 04-1027), and based on this observation, the (111) plane of the cubic lattice of Ni was the predominant one. In order to look into the distribution of the crystalline Ni and their crystallite size distribution at the electrode surface, a normal XRD pattern was not useful. The micro X-Ray diffraction (μXRD) pattern assists with the quantitative investigation of the effects of the crystalline nature on residue formation, as well as providing the possibility of probing small portions of the material surface. In μXRD, a parallel X-ray beam is collimated to form a small spot (~300 μm in diameter) prior to irradiating the sample. The small volumes of the Ni electrode that are irradiated by the beam can provide phase mapping in proximity to a perceived defect or point of interest, offering the possibility of a marked preferred orientation of the irradiated crystallite. Figure 4.2B illustrates the μXRD pattern of the electrolytic Ni electrode at various spots. The inset of Figure 4.2B depicts a photograph of the polished electrolytic Ni electrode and the position of the spots that were used to record for the μXRD patterns. Figure 4.2B(a) shows the μXRD pattern of the center spot, whereas the curves of (b) – (e) display the corner spots on the surface of the polished electrolytic Ni electrode. The XRD patterns of the (a), (b), (c), and (e) spots in Figure 4.2B reveal that the Ni (111) plane was most dominant, and the peak intensity of the other planes decreased in the order of (111) > (200) > (220) > (311).

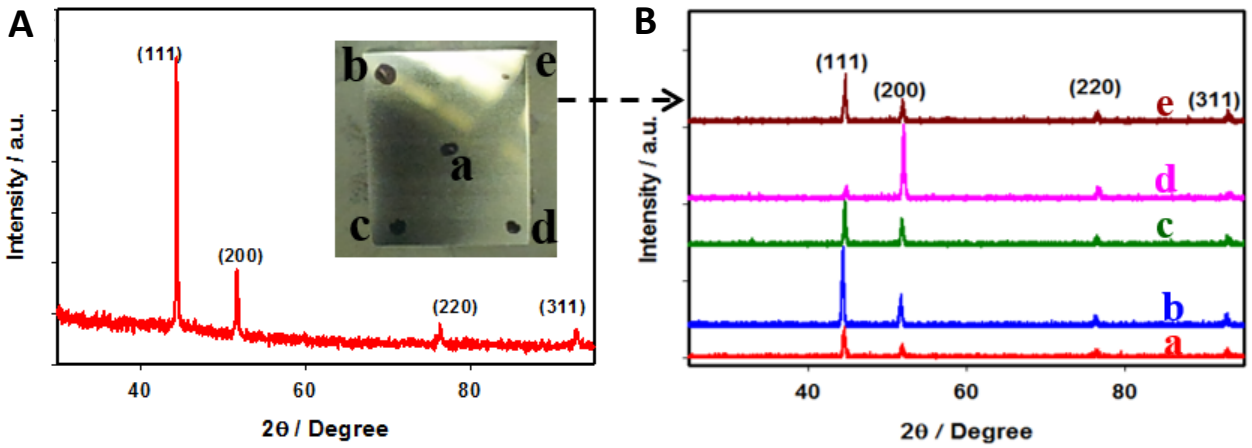

Figure 4.2 (A) XRD pattern of the electrolytic Ni (inset: photographs of the electrolytic Ni with the position of the spots (a-e) used for μ-XRD measurements), (B) μ-XRD patterns of the spots (a-e as displayed in the inset of (A)) on the surface of the electrolytic Ni.

Conversely, the obtained μXRD pattern of the spot (d) exhibited that the (200) plane of Ni was dominant rather than the (111) plane. In order to provide quantitative data on the crystalline nature of the electrolytic Ni electrode, the μXRD peak intensity ratios of planes (111) to (200) were estimated as 3.2, 2.6, 3.1, 0.2, and 1.9 for the spots of (a), (b), (c), (d) and (e), respectively. Based on the μXRD investigation, it was important to note that the crystallinity of the electrolytic Ni varied significantly from site to site. In addition, it helps to understand that the homogenous distribution of the crystallinity of the metal would likely provide a more homogeneous anodic dissolution of the metal. Therefore, the variation of the Ni crystallinity might be able to affect the homogeneous dissolution of electrolytic Ni during the electrochemical anodic dissolution of Ni electrode.

4.3.2. ICP-AES analysis of the dissolved electrolytic Ni

To further quantitatively study the potential presence of diminutive amounts of impurities, other than the small amounts of carbon and oxygen species not detected by EDS spectroscopy (as shown in Figure 4.3B), an ICP-AES technique was performed. Recently, the electrochemical dissolution of gold was quantitatively investigated by Cherevko et al., using ICP-MS analysis [27]. This technique facilitated a deeper understanding of the formation of residues during electrochemical dissolution. Therefore, to discover the presence of impurities at the electrolytic Ni electrode, the ICP-AES technique was applied by applying the small current density of 4.0 mA cm^{-2} for 10 min, whereby the anodic electrochemical dissolution of the electrolytic Ni was quantitatively investigated by an ICP-AES analysis in 0.1 M H_2SO_4 using our custom designed two-compartment three electrode cell. The electrolytic Ni was used as the anode in one compartment along with an Ag/AgCl reference electrode, whereas a Pt coil was employed as the cathode in the other compartment, and a macroreticular anion exchange resin was installed to separate the anodic and cathodic cells, as presented schematically in Figure 4.3. Solution collected from the anodic compartment of the electrochemical cell was subsequently analyzed by ICP-AES measurements.

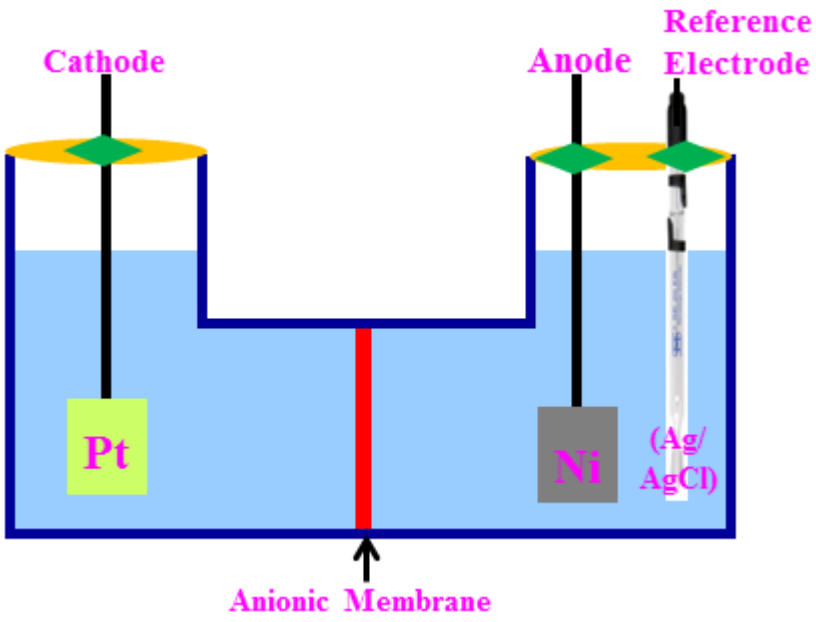

Figure 4.3 Schematic illustration of the two-compartment electrochemical cell for the dissolution of the electrolytic Ni electrode and carrying out the ICP-AES studies.

The resulting quantities of the elements that were found in the solution, other than the elements corresponding to the solution, are presented in Figure 4.4. This figure depicts the plot of the weight of metal ions against the total quantity of the metal ions present in the solution. The ICP-AES results indicated that the electrolytic Ni possessed some impurities, such as Fe and Cu, which were associated with Ni. The quantities of the obtained Fe, Cu, and Cr metallic impurities during the anodic dissolution of electrolytic Ni electrode were found to be 0.078, 0.301, and 0.002 $\mu g\ mL^{-1}$ (which is negligible for Cr) , respectively. The percentage of the obtained Fe, Cu and Cr impurities were calculated to be 0.052, 0.203, and 0.001%, respectively. Compared to the other impurities, there was a higher amount of copper in the electrolytic Ni electrode. The presence of these metal impurities on the electrolytic Ni electrode might partially explain the generation of residue in industrial refinery applications.

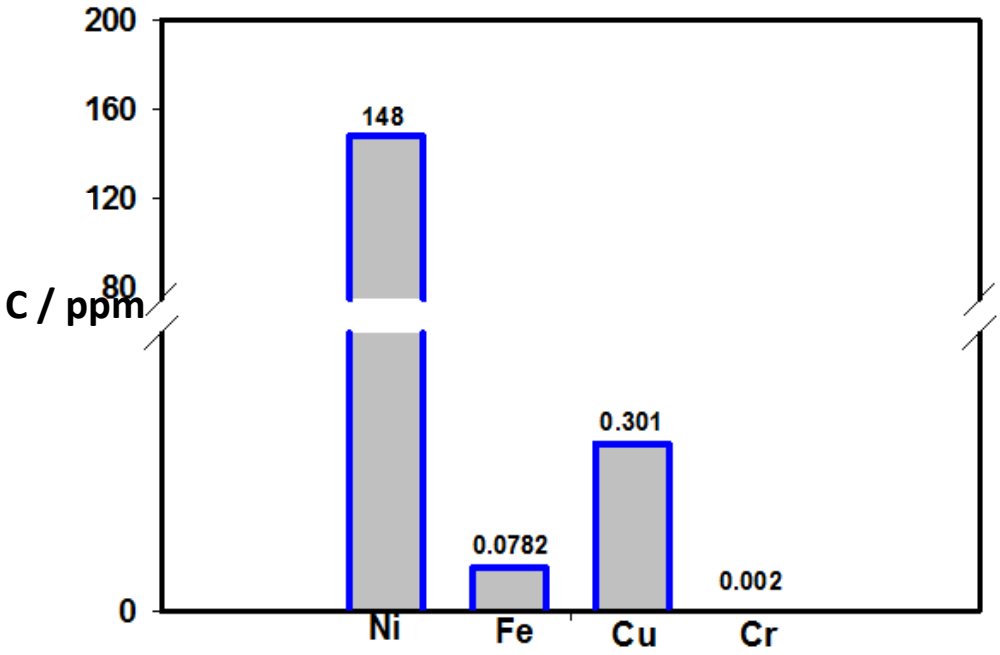

Figure 4.4 Concentration of dissolved metal ions other than Ni in a 0.1 M H_2SO_4 solution.

4.3.3. Electrochemical investigations of the electrolytic Ni electrode

The electrochemical response of the Ni electrode offered an initial approximation of the dissolution and passivation processes that proceeded in the electrolyte, or Watts solution in this case. Figure 4.5A depicts the cyclic voltammogram of the electrolytic Ni electrode in Watts solution and investigates the anodic behavior of the electrolytic Ni electrode. On the anodic scan, the active anodic dissolution process of Ni occurred in the range of from 0 to 0.3 V vs. Ag/AgCl with an anodic peak current density (J_{pa}) at ~0.2 mA. The breakdown potential (E_b) of the Ni electrode, where there is a sudden increase in current density by a slight increase in potential, was observed at ~0.4 V, whereas the anodic dissolution took place in the active dissolution area of the Ni electrode. The oxidation process of the electrolytic Ni electrode proceeded at low anodic potentials of ~0.2 V which led to the formation of an oxide film that was most likely composed of an inner NiO layer and a $Ni(OH)_2$ outer layer [28]. Due to the initial stage of anodic oxidation at

the Ni electrode, the large transient current density was attained (potential range of 0.1 to 0.3 V), which suddenly decreased. It was assumed that this decrease in the current response was due to the formation of passive NiO species. The onset potential of the transpassive region for the electrolytic Ni electrode in Watts solution, was obtained at ~0.4 V. Also a small passive region was observed in the potential range of 0.3–0.4 V. The presence of a more uniform and protective film of oxide and hydroxide nature could cause the passive region to appear at more positive potentials (as observed here) [29, 30]. The nickel electrode behaved with a typical active/passive region in Watts solution, and the mechanism of the Ni dissolution and passivation has been previously explained in the literature [31-33]. In short, the adsorption and discharge of hydroxyl ions (OH^-) with the release of one electron at the Ni anode surface, and the formation of adsorbed hydroxide (OH) proceeded as is explained by the reaction in Eq. 4.1. The adsorbed hydroxide (OH) discharged further and released an electron, as shown in the reaction of Eq. 4.2. The reaction in Eq. 4.3 is a rate determining step, and the adsorption of $NiOH_{ad}$ species obeyed the Langmuir isotherm, which is an expression that is employed for steady-state current. The obvious reaction is the formation of nickel ions (Ni^{2+}) with the further release of an electron. Moreover, the rate of the anodic dissolution of Ni was controlled by the quantity of hydroxyl ions (OH^-) that were involved in the reaction cycle. The electrochemical oxidation of Ni electrode occurred via two competitive processes involving, (i) the formation of a passive layer (Eq. 4.2) and (ii) the dissolution of nickel (Eq. 4.3).

$$Ni + OH^- \leftrightarrow NiOH_{ad} + e^- \quad (4.1)$$

$$NiOH_{ad} \rightarrow NiOH^+ + e^- \quad (4.2)$$

$$NiOH^+ \rightarrow Ni^{2+} + e^- \quad (4.3)$$

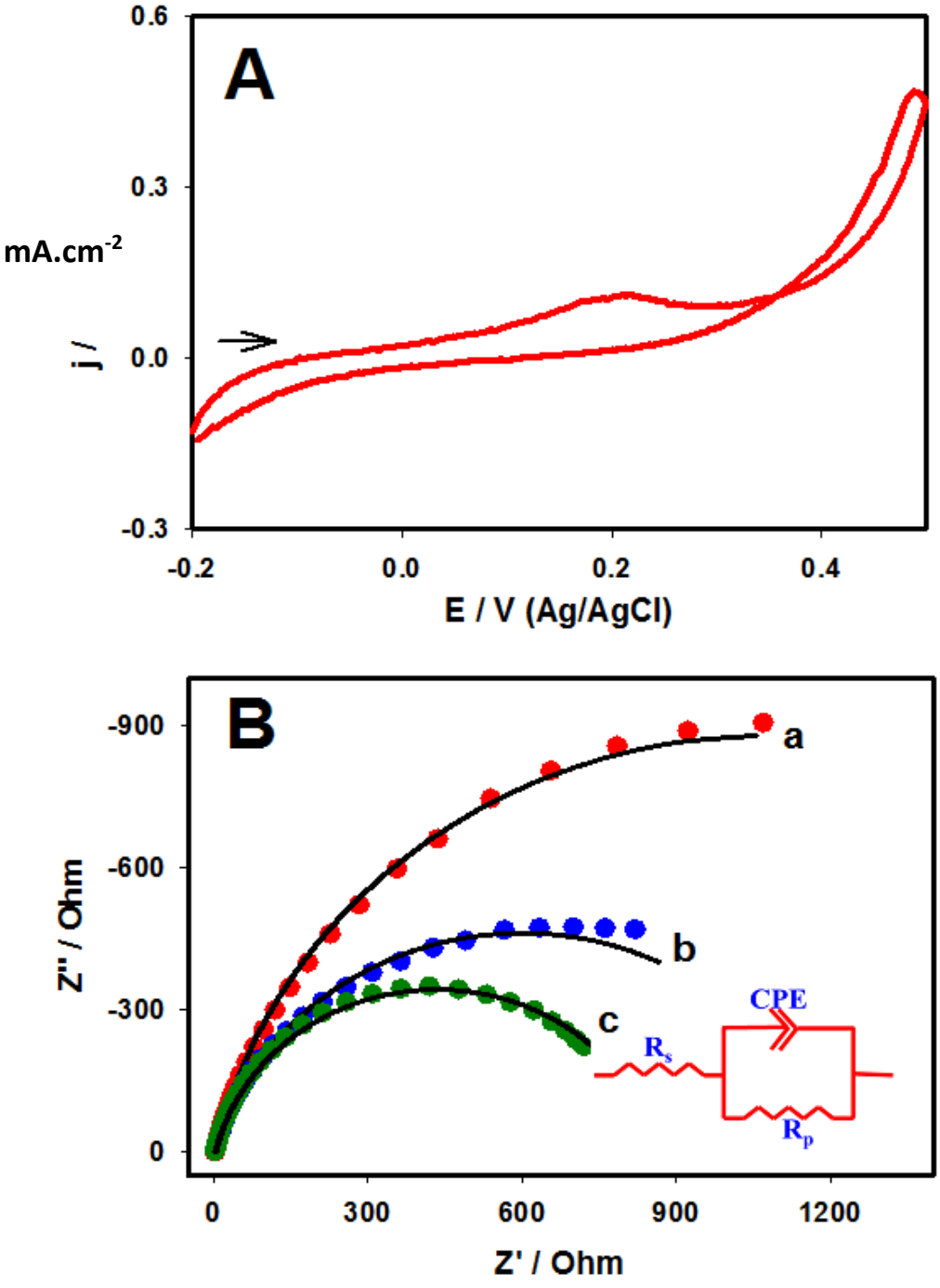

Figure 4.5 (A) Cyclic voltammogram recorded at the electrolytic Ni electrode in Watts solution at a scan rate of 20 mV s^{-1}, (B) electrochemical impedance spectra of the electrolytic Ni electrode recorded at different applied potentials of 0.10 (a), 0.15 (b), and 0.20 V vs. Ni (c) in Watts solution at an amplitude of 5 mV and frequency range of 100 kHz to 50 mHz (inset is the corresponding equivalent electric circuit).

An electrochemical impedance spectroscopic (EIS) study provided information about the interfacial properties of electrolytic Ni electrode in Watts solution, and is displayed in Figure 4.5B. A Nyquist plot of the complex impedance represents the imaginary versus the real part of the impedance, which is in the shape of a semicircle at higher frequencies. This corresponds to the electron-transfer-limited process, whereas the linear portion at lower frequencies corresponds to the diffusion-controlled process (which was not observed here) [34]. EIS was recorded under three potentials at 0.10, 0.15, and 0.20 V for the electrolytic Ni electrode, which are shown in Figure 4.5B. All of the complex Nyquist plot results were fitted with equivalent electric circuits, which are presented in the inset of Figure 4.5B. The experimental results are displayed in symbols, and the equivalent fitting curves are presented as the solid lines together with the experimental data. The R_s and R_p elements and CPE represent the uncompensated solution resistance, polarization resistance (resistance against charge transfer at the electrode), and the constant phase element. Generally, CPE is defined by two components; CPE-T (capacitance value) and CPE-P (a constant describing how close the CPE is to an ideal capacitor).

The elements of the electric equivalent values, as well as the errors (%) associated with them obtained via the fitting of the experimental data are presented in Table 4.1. The error values showed less than a 3% error, which indicates that the equivalent electric circuit is well in agreement with the experimental results. The R_s values were found in the range of from 3.15-3.24 Ω under all of the applied potentials to the electrolytic Ni electrode. The obtained R_p values were 2153.0, 1192.0, and 861.4 Ω for the applied potentials of 0.10, 0.15, and 0.20 V, respectively. The obtained CPE-P values were ~0.84 to 0.87, 0.85, suggesting that the CPE-T values acquired in this study were close to ideal C_{dl} (where CPE-P is equal to 1). The CPE-T values were 0.11, 0.12, and 0.17 mF cm^{-2} for applied electrode potentials of 0.10, 0.15, and 0.20 V, respectively. At an applied potential

of 0.2 V (the anodic peak potential), a smaller R_p value and higher capacitance (CPE-T) were obtained in contrast to lower applied potentials, indicating the faster kinetics of the active dissolution process taking place by increasing the applied electrochemical dissolution potentials.

Table 4.1 EIS fitted elemental data with errors derived from the Nyquist plots in Figure 4.5B.

E / V vs. Ag/AgCl	R_s / Ω.cm^2		R_p / Ω cm^2		CPE-T / mF cm^{-2}		CPE-P	
	Value	Error / %	Value	Error / %	Value	Error / %	Value	Error / %
0.10	3.22	0.78	2153.00	2.67	0.11	1.49	0.87	0.28
0.15	3.15	0.81	1192.00	1.79	0.12	1.62	0.84	0.29
0.20	3.24	0.82	861.4	1.31	0.17	1.74	0.85	0.31

4.3.4. Effect of applied current densities

The effect of the applied current densities on the interface dynamics during the dissolution and passivation of Ni was analyzed by monitoring changes in the surface morphology of the electrolytic Ni, which were acquired from SEM images. Changes in the surface morphology of the electrolytic Ni electrode was investigated using the images that were obtained following the removal of the electrode from the solution under various applied current densities, and are displayed in Figure 4.6. Increasing the applied current densities resulted in higher electrode potentials (Figure not shown here). Figure 4.6A presents a SEM image of the polished surface of the electrolytic Ni electrode. The initial surface morphology revealed a slightly corrugated morphology with initial micrometer sized grains, while several scratches remaining from the polishing step were still visible. Figure 4.6B displays a SEM image of the electrolytic Ni electrode

surface following the application of a current density of 4.0 mA cm^{-2} for 10 min. It was observed that by applying a current density of 4.0 mA cm^{-2}, a homogeneous dissolution took place on the surface of electrolytic Ni, as shown in Figure 4.6B. The average pit size was estimated to be ~53.2 nm, and by applying the low current density of 4.0 mA cm^{-2}, an almost uniform pit distribution was obtained. In contrast, by applying current densities of 8.0 and 16.0 mA cm^{-2} for 10 min, relatively deeper and wider pits were formed on the surface of the metal (as shown in Figure 4.6C and D). At an applied current density of 8.0 mA cm^{-2}, a mixture of large and small pits was found at the electrolytic Ni electrode. The average dimensions of these large and small pits were calculated to be ~217.2 and ~51.3 nm, respectively, for the electrolytic Ni electrode. With the application of a current density of 16.0 mA cm^{-2}, extremely large sized pits of ~3.5 μm were formed, and no small pits were observed. It was also recognized that micrometer size grains, observed in Figure 4.6D, were easier to dissolve as the anodic dissolution process progressed. It has been reported that anodic dissolution efficiency was decreased with higher current densities, which might lead to the enhanced formation of NiO [35]. It was also thought that the formation of large pits was due to the stress-free attack that occurred at the inner walls of the pits, where there was competition between different processes occurring during the anodic dissolution of the metal surface, such as dissolution and passivation, which contributed to the change of particular topographies of the metal surface [36]. Electrochemical dissolution processes are typically related to the variable distribution of the active sites of Ni, and the associated progress of different types of surface roughness [37]. Dissolution occurred in the active region of the electrolytic Ni samples, and the application of low current densities were more desired in order for the homogeneous dissolution of Ni to occur.

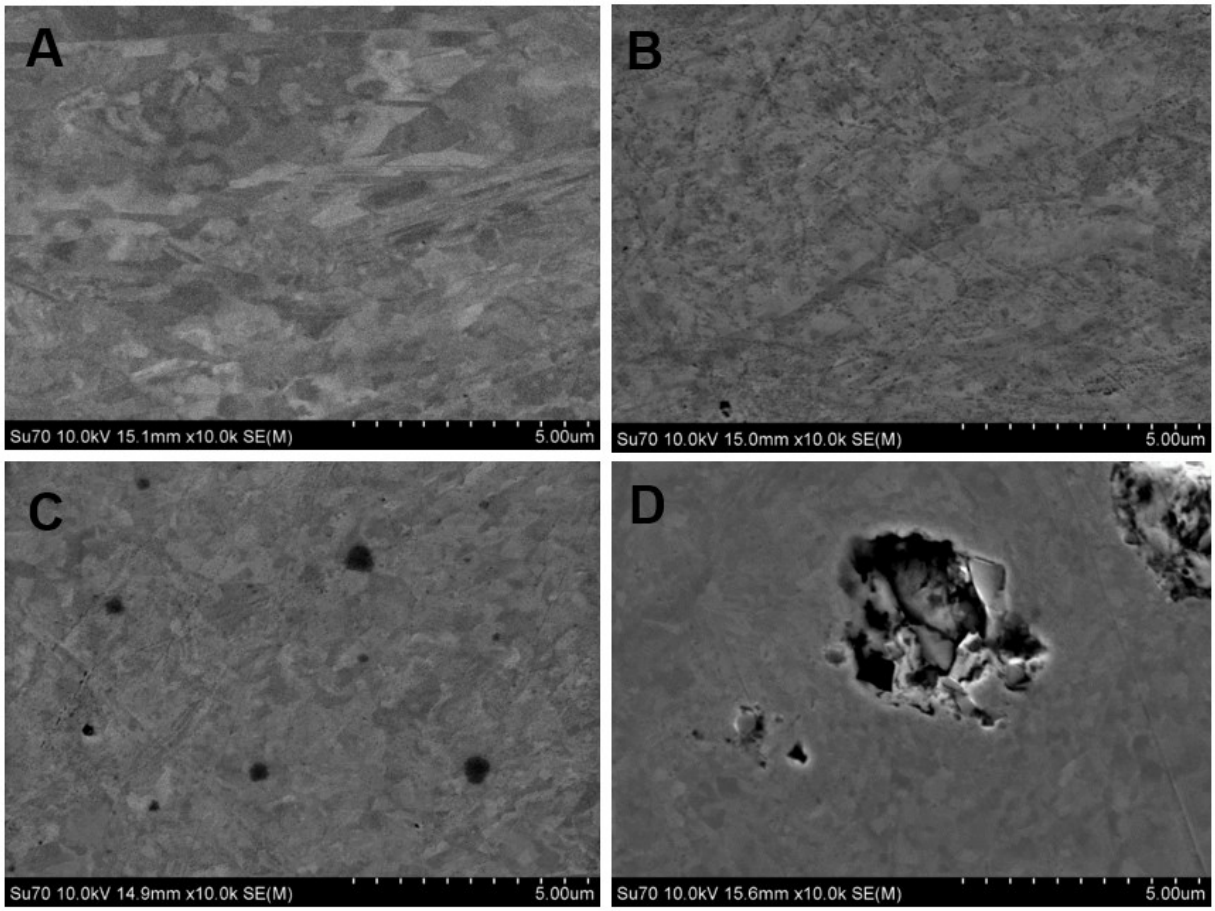

Figure 4.6 SEM images of (A) polished electrolytic Ni prior to and following the application of various current densities of (B) 4.0, (C) 8.0, and (D) 16.0 mA cm^{-2} for 10 min.

4.3.5. Changes in surface morphology during anodic dissolution

Figure 4.7 presents SEM images of the electrolytic Ni electrode during the anodic dissolution in Watts solution, demonstrating the effect of time on the anodic dissolution and surface morphology. The anodic dissolution experiment was carried out at constant applied current density of 8.0 mA cm^{-2} for 10, 20, and 30 minutes. Changes in the surface morphology of the Ni electrode

were examined by SEM, which were obtained once the sample was extracted from the solution and washed every 10 min for total of three times. The dissolution of the electrolytic Ni electrode was nearly homogeneous, with an average pit size of 0.42 μm following 10 min of anodic dissolution.

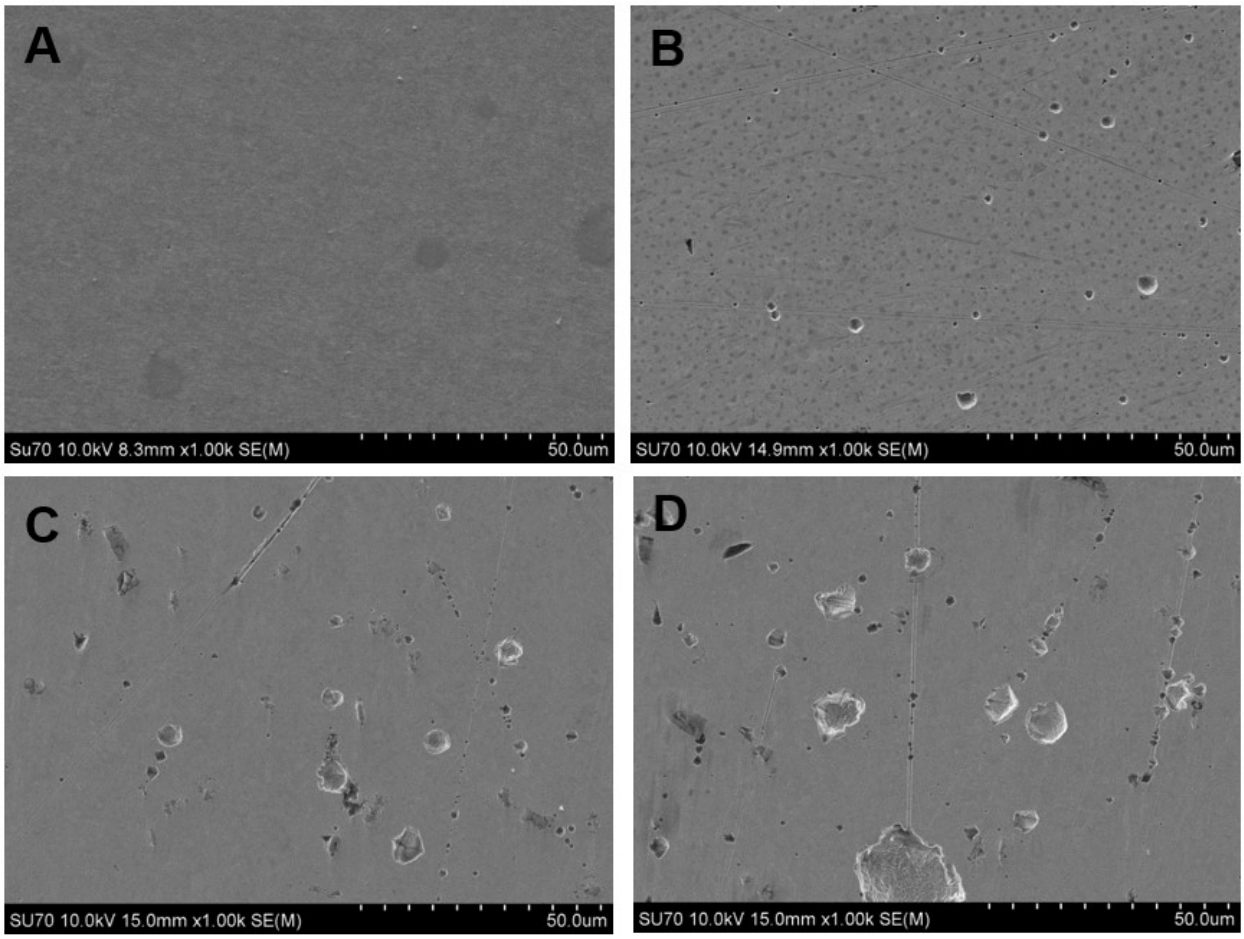

Figure 4.7 SEM images obtained for electrolytic Ni sample during the dissolution for (A) 0 min, (B) 10 min, (C) 20 min, and (D) 30 min at an applied constant current density of 8.0 mA cm^{-2}.

As seen in Figure 4.7B, the subsequently preferred active sites were readily available for the further active dissolution of the Ni after the first 10 min. Figure 4.7C shows a SEM image of the electrolytic Ni electrode following the application of a constant current density of 8.0 mA cm^{-2} for 20 min. Large pits and some smaller pits were observed at the electrolytic Ni electrode, as shown in Figure 4.7C. Small pit sizes in the range of from 0.32 to 0.53 μm were observed at scratched sites on the Ni electrode. Pit sizes were increased by the localized anodic dissolution of the electrolytic Ni, as can be easily seen in Figure 4.7D. Layer by layer structures were found within the formed large pits. It is possible that the probable adsorption of chloride ions and deterioration of the passive film was a more favorable dissolution mechanism. Localized dissolution mostly occurred at the electrode surface, since the dimensions of the pits were observed to increase. Also, the surface roughness as function of dissolution time was significantly increased. Dissolution within the pits increased via localized dissolution with increasing dissolution periods, which can be easily seen in Figure 4.7B-D.

4.3.6. Micro-XRD analysis of the electrolytic Ni

The crystalline nature of the electrolytic Ni electrode was investigated as a function of the anodic dissolution duration. The μXRD pattern was employed to study the crystallinity of the electrolytic Ni electrode at a specific site (marked spots shown in Figure 4.2). The μXRD pattern was recorded every 10 min of dissolution at an applied current density of 8.0 mA cm^{-2}, with the results presented in Figure 4.8. Our previous experiments suggested that the distribution of grain sizes and the crystallinity of the electrolytic Ni were variable. Hence, the μXRD spectra were recorded at specified locations at the center of the electrolytic Ni electrode, and the crystallinity of the sample was monitored as the dissolution progressed.

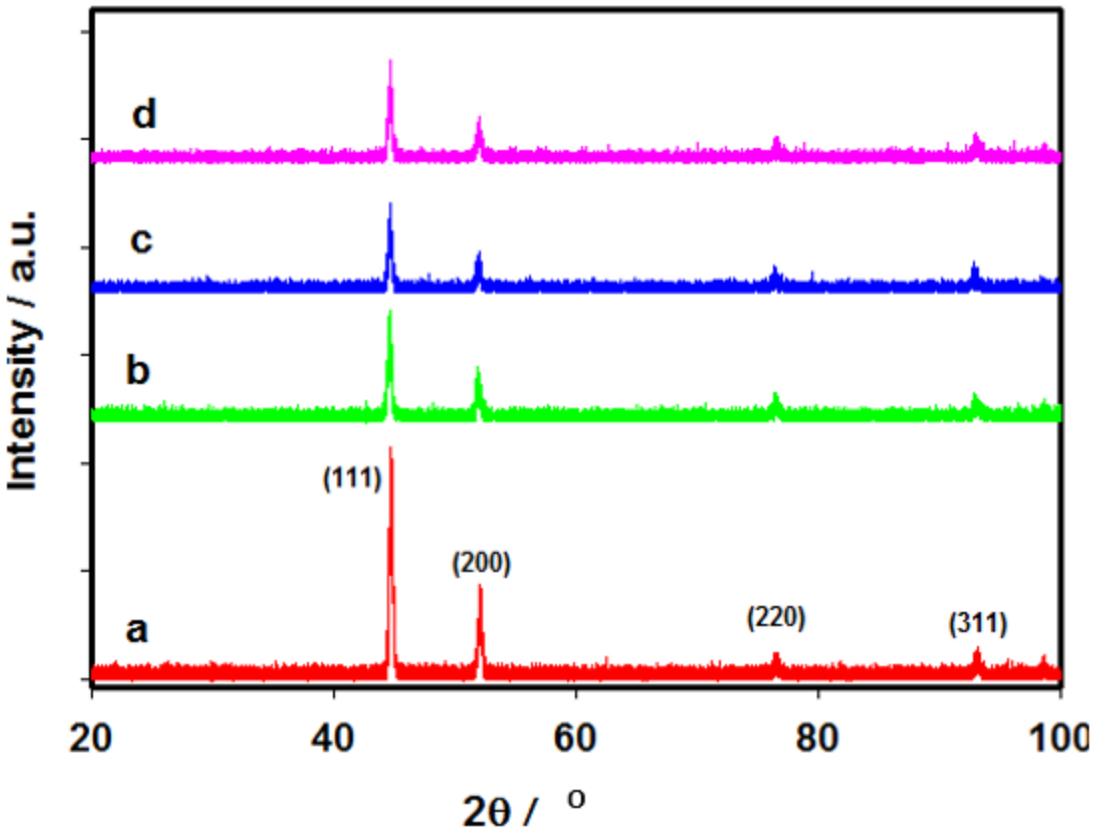

Figure 4.8 μXRD of the center spot of the electrolytic Ni sample recorded during the dissolution for (a) 0 min, (b) 10 min, (c) 20 min, and (d) 30 min at an applied constant current density of 8.0 mA cm^{-2}.

Figure 4.8a depicts the μXRD pattern of the electrolytic Ni electrode at a specified location prior to dissolution and corresponded to cubic crystalline nickel, with a predominant (111) plane. By increasing the anodic dissolution time of the electrolytic Ni, the peak intensity ratio, as well as the intensities were decreased. The peak intensity ratio of the (111) plane to the (200) plane was estimated as 3.2, 2.9, 2.8, and 1.7 for the curves of (a), (b), (c), and (d), respectively, where the ratio decreased from 3.6 to 1.7 for the electrolytic Ni electrode. The crystallite size calculation using the Scherrer equation ($\tau = \frac{K\lambda}{\beta\, cos\theta}$, where τ is average crystal size, *K* is a dimensionless shape factor, λ is X-ray wavelength, β is the full width at half maximum (FWHM) and θ is Bragg angle)

indicated that the crystallite size was decreased from 67 nm to 22 nm over a 30 min dissolution period under an applied current density of 8.0 $mAcm^{-2}$.

The crystalline nature, inner crystallite sizes, and their distribution may be controlled by the formation of passive layers and the rate of anodic dissolution [38]. Mishra et al. [39] studied the effects of grain size on the dissolution of Ni, and demonstrated that Ni with a small grain size might result in a lower dissolution rate. The Ni dissolution rate was decreased with grain size due to the great hindrance of anodic dissolution. The μXRD analysis indicated that inner surface grain sizes were smaller than the outer grains on the surface of Ni. These results demonstrated that the μXRD technique was a powerful tool for quantitative studies on the dissolution processes at the Ni electrode.

4.4 Conclusions

In conclusion, we demonstrated the surface morphology, crystalline nature, and distribution and the electrochemical characteristics associated with the anodic dissolution of an electrolytic Ni electrode in Watts solution. ICP-AES provided quantitative data as relates to the presence of impurities at the electrolytic Ni electrode during the anodic dissolution by designing a custom-made electrochemical cell. The anodic dissolution process of the electrolytic Ni electrode was systematically investigated by altering the surface morphology and crystallinity through the application of current densities at 4.0, 8.0, and 16.0 mA cm^{-2}. The μ-XRD assisted with an investigation into the crystallinity of electrolytic Ni during the anodic dissolution at a specified site. The cubic crystalline structure was not altered during the dissolution of the electrolytic Ni electrode, whereas the peak intensity ratio of Ni (111)/(200) planes revealed that the (200) plane

intensity increased by prolonging the duration of the anodic dissolution at the electrolytic Ni electrode.

Our investigations suggest that (i) the variable crystalline nature, (ii) the presence of other metallic impurities such as Cu, Fe, and Cr, (iii) the disappearance of the (111) plane Ni crystals by increasing the anodic dissolution of the electrolytic Ni, (iv) variable microstructured Ni grains and (v) the localized anodic dissolution behaviors of the electrolytic Ni electrode, might be involved in the formation of the residue. A model investigation was studied for the anodic dissolution of the electrolytic Ni electrode in the present investigation, which demonstrated that the rapid interfacial dissolution kinetics of Ni soluble materials may be readily studied, which could open the way for improvements in industrial refinery based applications.

References

[1] S.-G. Kim, S. P. Yoon, J. Han, S. W. Nam, T. H. Lim, I.-H. Oh, S.-A. Hong, A study on the chemical stability and electrode performance of modified NiO cathodes for molten carbonate fuel cells, *Electrochim. Acta,* 2004, **49**, 3081-3089.

[2] Li F, Liu W, Sun Y, Ding W, Cheng S. Enhancing hydrogen production with Ni–P coated nickel foam as cathode catalyst in single chamber microbial electrolysis cells. *Int. J. Hydrogen Energy*, 2017, **42**, 3641-3646.

[3] Q. Wu, L. Jiang, Q. Tang, J. Liu, S. Wang, G. Sun, Activity and stability of the $Ni(OH)_2$-MnO_x/C composite for oxygen reduction reaction in alkaline solution, *Electrochim. Acta*, 2013, **91**, 314-322.

[4] E. M. A. Martini, S. T. Amaral, I. L. Muller, Electrochemical behaviour of Invar in phosphate solutions at pH= 6.0, *Corros. Sci.*, 2004, **46**, 2097-2115.

[5] Z. Chao, X. Yaomu, L. Chufeng, L. Conghua, The effect of mucin, fibrinogen and IgG on the corrosion behaviour of Ni–Ti alloy and stainless steel, *BioMetals*, 2017, **30**, 367-377.

[6] S. T. Rashkov, N. Atanssov, Structure and corrosion resistance of electrolytic nickel coatings containing codeposited nonconducting particles, *J. Appl. Electrochem*., 1980, **10**, 535-541.

[7] A. Jouanneau, M. Keddam, M.C. Petit, A general model of the anodic behaviour of nickel in acidic media, *Electrochim. Acta*, 1976, **21**, 287-292.

[8] P. Najafi Sayar, M.E. Bahrololoom, Comparison of anodic dissolution, surface brightness and surface roughness of nanocrystalline nickel coatings with conventional decorative chromium coatings, *J. Appl. Electrochem*., 2009, **39**, 2489-2496.

[9] J. H. Gerretsen, J. H. W. De Wit, The passivation of nickel in 0.5 M sulphuric acid, *J. Appl. Electrochem*., 1991, **21**, 276-277.

[10] S. Sathyavathi, A. Manjula, J. Rajendhran, P. Gunasekaran, Extracellular synthesis and characterization of nickel oxide nanoparticles from Microbacterium sp. MRS-1 towards bioremediation of nickel electroplating industrial effluent, *Bioresource Technol*., 2014, **165**, 270-273.

[11] D. M. Muir, E. Ho, Process review and electrochemistry of nickel sulphides and nickel mattes in acidic sulphate and chloride media, *Miner. Process. Extr. Metall.*, 2006, **115**, 57-65.

[12] C. Lupi, M. Pasquali, A. Dellera, Studies concerning nickel electrowinning from acidic and alkaline electrolytes, *Miner. Eng.*, 2006, **19**, 1246-1250.

[13] A. Brenner, V. Zentner, C. W. Jennings, Plating, 1952, **39**, 865-927.

[14] O. P. Watts, Rapid nickel plating, *Trans. Am. Electrochem. Soc.*, 1916, **29**, 395.

[15] A. G. Muñoz, G. Benitez, M. E. Vela, R. C. Salvarezza, Influence of the adsorption of N species on the anodic dissolution of Ni, *Langmuir*, 2004, **20**, 2361-2368.

[16] J. Gregori, J. J. Garcıa-Jareno, D. Gimenez, F. Vicente, Kinetic calculations of the Ni anodic dissolution from EIS, *J. Solid State Electrochem.*, 2005, **9**, 83-90.

[17] S. G. Real, M. R. Barbosa, J. R. Vilche, A. J. Arvıa, Influence of chloride concentration on the active dissolution and passivation of nickel electrodes in acid sulfate solutions, *J. Elect. Soc.*, 1990, **137**, 1696-1702.

[18] G. Cordeiro, O.R. Mattos, O.E. Barcia, L. Beaunier, C. Deslouis, B. Tribolloet, Anodic dissolution of nickel in concentrated sulfuric acidic solutions, *J. Appl. Electrochem.*, 1996, **26**, 1083-1092.

[19] L. Wang, J. Zhang, Y. Gao, Q. Xue, L. Hu, T. Xu, Grain size effect in corrosion behavior of electrodeposited nanocrystalline Ni coatings in alkaline solution, *Scripta Mater*., 2006, **55**, 657-660.

[20] M. Zamin, M. B. Ives, Effect of Chloride ion concentration on the anodic dissolution behavior of nickel, *Corrosion,* 1973, **29**, 319-324.

[21] S. G. Real, J. R. Vilche, A. J. Arvia, The characteristics of the potentiodynamic potential/current profiles obtained with the Ni/0.5 N H_2SO_4 interface. A contribution to the mechanism of the electrode process, *Corros. Sci.*, 1980, **20**, 563-586.

[22] M. Mettikos-Hukovit, I. Milosev, Electrochemical methods in the study of localized corrosion attack, *J. Appl. Electrochem*., 1992, **2**, 448-455.

[23] B. MacDougall, Effect of chloride ion on the localized breakdown of nickel oxide films, *J. Electrochem. Soc.*, 1979, **126**, 919-925.

[24] S. Z. Fernandes, S. G. Mehendale, S. Venkatachalam, Influence of frequency of alternating current on the electrochemical dissolution of mild steel and nickel, *J. Appl. Electrochem*., 1980, **10**, 649-654.

[25] A. G. Muñoz, J. W. Schultze, Effects of NO_2^- on the corrosion of Ni in phosphate solutions, *Electrochim. Acta*, 2004, **49**, 293-301.

[26] K. Krug, D. Kaminski, F. Golks, J. Stettner, O. M. Magnussen, Real-time surface x-ray scattering study of Au (111) electrochemical dissolution, *J. Phys. Chem. C*, 2010, **114**, 18634-18644.

[27] S. Cherevko, A. A. Topalov, I. Katsounaros, K. J. J. Mayrhofer, Electrochemical dissolution of gold in acidic medium, *Electrochem. Commun*., 2013, **28**, 44-46.

[28] H. Ayoub, S. Griveau, V. Lair, P. Brunswick, M. Cassir, F. Bedioui, Electrochemical characterization of nickel electrodes in phosphate and carbonate electrolytes in view of assessing a medical diagnostic device for the detection of early diabetes, *Electroanal*., 2010, **22**, 2483-2490.

[29] J. R. Vilche, A. J. Arvia, Kinetics and mechanism of the nickel electrode-II. Acid solutions containing a high concentration of sulphate and nickel ions, *Corros. Sci*., 1978, **18**, 441-463.

[30] S. G. Real, M. R. Barbosa, J. R. Vilche, A. J. Arvia, Influence of chloride concentration on the active dissolution and passivation of nickel electrodes in acid sulfate solutions, *J. Electrochem. Soc.*, 1990, **137**, 1696-1702.

[31] J. M. Bockris, A. K. N. Reddy, B. Rao, An ellipsometric determination of the mechanism of passivity of nickel, *J. Electrochem. Soc*., 1966, **113**, 1133-1144.

[32] N. Sato, G. Okamoto, Anodic passivation of nickel in sulfuric acid solutions, *J. Electrochem. Soc*., 1963, **110**, 605-614.

[33] D. Danset, L. Manceron, L. Andrews, Vibrational spectra of nickel and platinum dioxide molecules isolated in solid argon, *J. Phys. Chem. B*., 2001, **105**, 7205-7210.

[34] J.-W. M. Cappadonia, J. Divisek, T. von der Heyden, U. Stimming, Oxygen evolution at nickel anodes in concentrated alkaline solution, *Electrochim. Acta*, 1994, **39**, 1559-1564.

[35] K. Deo, S. G. Mehendale, S. Venkatachalam, Electrochemical dissolution of nickel in sulphuric acid by alternating current, *J. Appl. Electrochem.,*1976, 6, 37-43.

[36] D. W. Suggs, A. J. Bard, Scanning tunneling microscopic study with atomic resolution of the dissolution of Cu (111) in aqueous chloride solutions, *J. Am. Chem. Soc*., 1994, **116**, 10725-10733.

[37] A. G. Munoz, M. E. Vela, R.C. Salvarezza, Complex surface dynamics during anodic dissolution of Ni, *Langmuir*, 2005, **21**, 9238-9245.

[38] R. Rofagha, R. Langer, A. M. El-Sherik, U. Erb, G. Palumbo, K. T. Aust, The corrosion behaviour of nanocrystalline nickel, *Scripta Metall*., 1991, **25**, 2867-2872.

[39] R. Mishra, R. Balasubramaniam, Effect of nanocrystalline grain size on the electrochemical and corrosion behavior of nickel, *Corros. Sci.*, 2004, **46**, 3019–3029.

Chapter 5: Long-Term Electrochemical Dissolution of Industrial Electrolytic Nickel and Residue Formation

5.1 Introduction

Nickel is a naturally-abundant transition metal that is very cost effective. Nickel-based materials have been the subject of many studies due to their good catalytic performance [1-2], corrosion resistance at room/high temperatures [3-5], mechanical [6], and magnetic properties [7]. They have been used in different applications, such as electrode materials in rechargeable alkaline batteries [8-12] and in fuel cells [13-16], electrochemical capacitors [17-19], sensors [20-22], electrocatalysts for oxygen evolution [23-26], and catalysts in the fertilizer industry [27-30].

High purity nickel is typically produced by two methods, including the Mond process and electrorefining, or electrowinning. In the Mond process, nickel is purified by passing carbon monoxide over solid nickel with high impurity values [31]. However, about 45% of nickel is produced through electrorefining or electrowinning processes from acidic sulfate containing solutions, which are very similar to electroplating in principle that leads to a high purity nickel as a result [32]. Nickel produced in later manner is referred to as electrolytic nickel.

Electroplating comprises one of the very simple processes for material deposition and surface coating, which has been used for over 150 years for depositing different metals such as nickel and its alloys [33]. More than 150,000 tons of nickel is electrodeposited worldwide for either decorative or functional applications every year [6]. The primary objective of the nickel coating is to serve as a protection against wear or corrosion, while providing a bright decorative finish. The physical characteristics of electroplated coatings are affected, and can be manipulated by different

parameters involved in the electroplating process, such as the composition of the bath and applied current density [6]. The most common bath used in industry for nickel plating is called “Watts” bath, which has been in use for ~100 years, which consists of nickel based chloride and sulfate salts with an acidic pH [6, 34]. In an actual electroplating plant setup, nickel chips or pellets are loaded into large titanium baskets as the replenishing source of nickel for the process, which maintains the nickel bath content by anodically dissolving into it [35].

The formation of residues during the process, at the bottom of the container within which the plating is being carried out, as well as in the baskets, is one of the major issues that electroplating plants face. In order to clean the bath and baskets of fine Ni particles, electroplating plants require regular maintenance shut-downs, which incur further significant cost increases for the process for plants, as well as loss of production [36]. Furthermore, the properties of the residue may be altered by changing the quality of the nickel feed. For example, studies have indicated that the residue that is collected following the dissolution of pure nickel is of a conductive nature. However, for nickel feeds that contain sulfur impurities, the residues were found to be non-conductive [36].

The objective of this work was to investigate the short-term and long-term dissolution behaviors, as well as the mechanisms of residue formation by industrial electrolytic nickel under various applied current densities. This knowledge will be implemented in the future toward resolving the issue of high residue formation by improving our understanding of the electrolytic Ni dissolution process, as well as those that underlie the formation of these residues. To this end, electrochemical Ni dissolution studies were undertaken under different current densities in combination with surface imaging and X-ray diffraction (XRD). This was done in order to monitor the surface morphologies and structures of dissolved Ni, and structural evolution as a function of the dissolution time. Scanning Electron Microscopy (SEM) equipped with an Energy Dispersive

Spectroscopy (EDS) detector is employed to determine the morphologies and elemental analyses of the residues.

5.2 Experimental

5.2.1 Chemicals and materials

$NiSO_4.6H_2O$, $NiCl_2.6H_2O$, and H_3BO_3 were purchased from Sigma-Aldrich and were of analytical grade. All chemicals were used as received without any further purification. A Watts bath was produced by mixing 300 g L^{-1} of $NiSO_4.6H_2O$, 45 g L^{-1} of $NiCl_2.6H_2O$, and 40 g L^{-1} of boric acid. Double distilled water (18.2 MΩ cm), purified by a Nanopure® water system, was used in the preparation of all solutions, which were made fresh for each experiment. The temperature of the solution was set to 55 ± 0.2 ºC and maintained using a Thermo Scientific water bath. Similarly, weighted electrolytic Ni chip samples of more than 99% purity were obtained from an industrial provider and used as working electrodes in their as-received condition. Titanium wires were employed as electrical contacts, while the connected areas were covered with Teflon tape in order to prevent dissolution beneath the connection, and possible disconnection, prior to the final stage of the experiment. In the second setup for long-term experiments, 80.88 g of the electrolytic Ni was fabricated as the anode (with a surface area of ~11.87 cm^2) by connecting a copper wire using soldering technique, followed by application of an epoxy coating above the connection and drying in an oven at 45 °C overnight. Prior to running any experiments, the samples were cleaned by sonication in acetone and pure water for 5 min each.

5.2.2 Surface characterization and electrochemical studies

The electrochemical experiments were carried out using a VoltaLab 40 (PGZ301 & VoltaMaster 4) for short-term studies and an Arbin Instruments (MSTAT, USA) potentiostat/galvanostat unit for long-term dissolution by employing a conventional one-compartment three-electrode cell. A commercial Ni plate and two etched Ti plate electrodes were employed as the reference electrode and counter electrodes, respectively. Since the long-term studies would take days to complete and the solution was practically saturated with nickel cations, the nickel sheets would remain stable enough and at equilibrium with the solution to play the role of the reference electrode. The cyclic voltammetry technique was performed at a scan rate of 20 mV s^{-1}. Electrochemical dissolution was performed by applying current densities of 15.0, 30.0, 45.0 mA g^{-1} (and 8.0 mA cm^{-2} for long-term dissolution) and employing the chronopotentiometric (CP) method. Accumulated residue at the bottom of the container, due to the long-term dissolution, was collected at different stages. At the very end of the dissolution process, when the connection between the Ti electrode and sample was no longer operational, the potential would get too high for the instrument to continue. The collection of the residue at the very end was carried out with the help of centrifuge device made by Thermo Electron Corporation (Biofude Startos). The study of the surface morphology was performed by means of a Hitachi SU-70 scanning electron microscopy (SEM) equipped with EDS, which was used for residue elemental analysis. XRD spectra were recorded using a Pananalytical X'pert Pro Diffractometer with a Ni filtered monochromatic Cu Kα (1.5406 Å, 2.2 KW Max.) radiation, whereas the patterns were analyzed using X'pert HighScorePlus software. The diffracted X-ray intensities were recorded in the 2θ range, from 10° to 100°.

5.3 Results and discussion

5.3.1 Electrochemical studies of nickel samples

Preliminary electrochemical studies of nickel samples in Watts solution at 55 ºC are presented in Figure 5.1. The cyclic voltammetry behavior of the samples prior to and following chronopotentiometry are presented in Figure 5.1A. Since voltammograms recorded at different stages during the long-term dissolution related to each sample (undergoing dissolution at different applied current densities) followed the same pattern, only the results for the sample that was studied at a current density of 30.0 mA g^{-1} will be presented here. The short-range CV (Figure 5.1A inset) reveals that no anodic peaks exist prior to running the CP. However, two anodic peaks appeared in the CV after running the CP for 5 min. It is likely that applying the current density for 5 min results in making the surface more active; hence, leading to the appearance of these two anodic peaks at ~150 and 290 mV vs. Ni, which are attributed to the active dissolution region [37]. It has been mentioned that nickel dissolution with different electrolytes under various conditions can exhibit diverse behaviors. In some cases, only a single anodic peak shows up on the CV, while at other times, two peaks can be observed [38]. Among the reasons, to date, that might account for the appearance of single or double peaks in the CVs include, certain differences in the structure and quality (e.g., texture, defects, impurities, density) of samples, as well as the pre-treatments carried out on the electrode, solution composition, and kinetics, such as the sweep rate, passivation potential, and hydrodynamic conditions (such as stirring) [39, 40]. Furthermore, in less acidic electrolytes, the dissolution of nickel might be inhibited due to the presence of surface oxide layers.

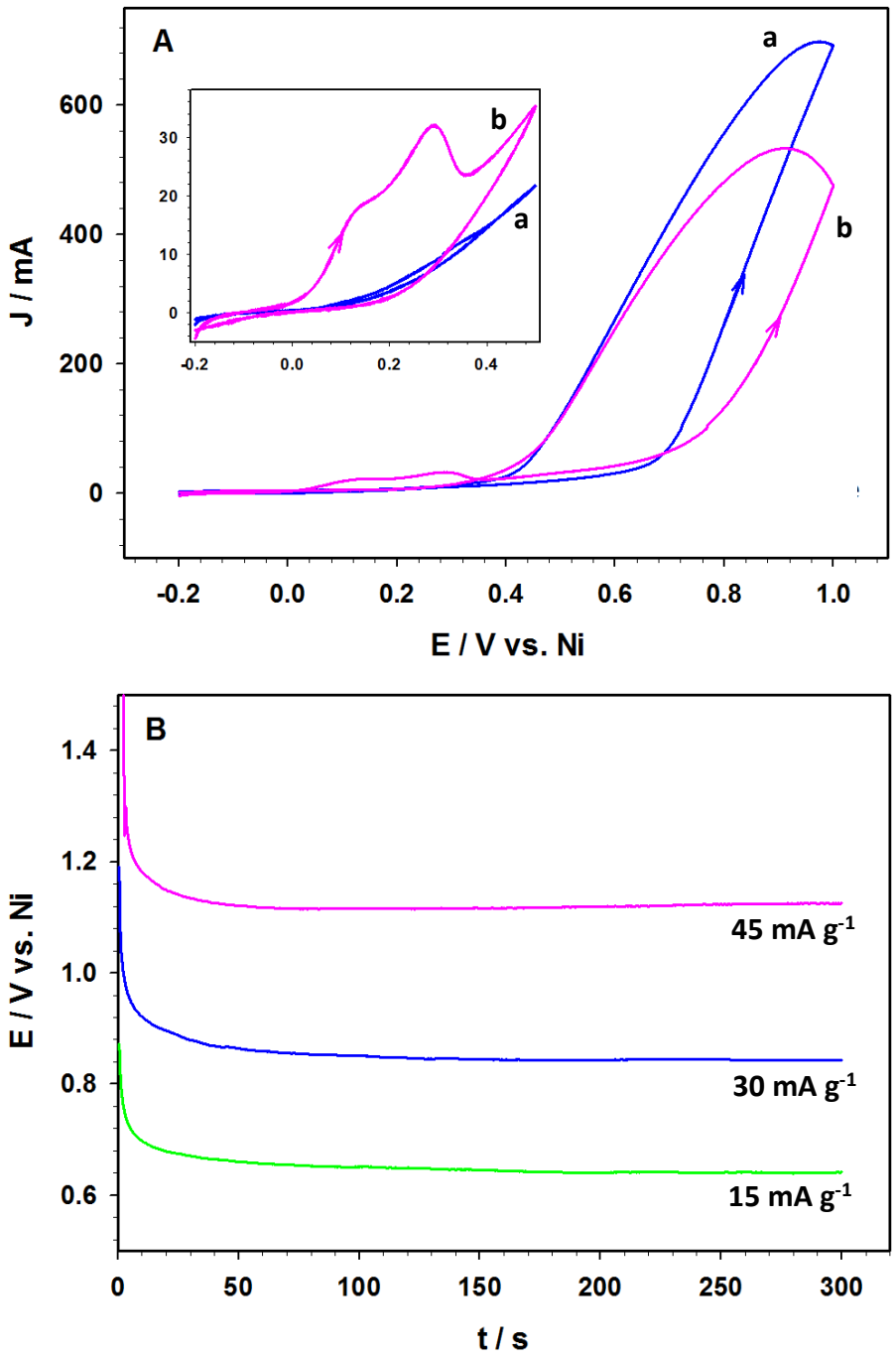

Figure 5.1 (A) Preliminary cyclic voltammetry prior to (a) and following (b) CP at 30.0 mA g^{-1} for 5 min, and (B) chronopotentiometry of the nickel sample in Watts solution at 30.0 mA g^{-1} for 5 min at 55 °C.

On the other hand, the appearance of the cathodic peak and reducibility of the Ni^{2+} is contingent on the formed layer during the electrochemical process, as well as the anodic scan of the CV,

which means that it is possible in some cases to have no cathodic peak during the cathodic scan (as seen in the Figure 5.1). In the case of α-$Ni(OH)_2$ the cathodic peak would be present, while if β-$Ni(OH)_2$ is formed, no cathodic peak is observed [41, 42]. The nature of the film formed on the surface is reported to be dependent on the potential and pH. Also, there is some debate between researchers as per the kinetics and mechanism of the dissolution, as well as the composition of the layer that is formed on the surface [39]. It has been mentioned that the passive film formed by the anodic current is not static. Rather, it is constantly dissolving and reforming while the potential is in passive region, which results in the continuous dissolution of the sample [39], i.e. only 20% of the current is consumed for passivation [43]. However, most recent reports concur that the surface consists of a duplex structure with an inner layer of NiO and an outer layer of $Ni(OH)_2$. The outer layer possesses a granular, porous and amorphous structure, which is likely due to the hydration of the oxide layer [44]. The structure of the hydroxide layer is more dependent on the history of the sample, whereas the oxide layer has a crystalline structure, and its structure and thickness relies on the passivation potential. Increasing the potential decreases the crystal size [39] while increasing the thickness [45].

The current response of the electrolytic nickel in the long-range CV (Figure 5.1A) attains its highest potential once the CP has decreased, in contrast to that prior to the CV. The long-range CV may be categorized into active dissolution, passivation, and transpassive dissolution regions. The active dissolution region in the long-range CV following 5 min of CP appears at between 0 and 350 mV vs. Ni for all the samples, which is not observed in the CVs carried out prior to the CP. Followed by the active dissolution region, there is a passive region at the potential range of ~600-700 mV, after which the transpassive region begins in the long-range CVs. The presence of the transpassive region is in good agreement with the electrochemical dissolution study of nickel

in a sulfuric acid solution [37]. After undergoing the CP, the transpassive region in the CV shifted to higher potentials, indicating that the potential required for the break-down of the passive film increased slightly following 5 min of the CP, which might be attributed to the formation of some species of surface coating at the applied current density. Transpassive dissolution has been reported to be due to the further oxidation of NiO and/or $Ni(OH)_2$ to NiOOH, which can chemically dissolve into the solution at low pH and, therefore, result in the breakdown of the passive layer [45], primarily at surface defect or inclusion sites [46].

Potential vs. time curves for nickel samples that underwent CP under different applied current densities for 5 min are presented in Figure 5.1B. The potential behavior based on time for all of the samples followed the same pattern. After a sharp increase in the potential at the very onset of the E-t plot (which might be due to the double layer capacitance charging and the breakdown of a possibly very thin passive layer of natural oxides that are formed on the samples), the samples attained a quite stable potential, which was about 640, 840, and 1125 mV under applied current densities of 15.0, 30.0, and 45.0 mA g^{-1}, respectively. As expected, the response potential increased with higher current densities. Based on the CV curve and recorded potentials of the CP, it appeared that the first sample, which underwent CP at a constant applied current of 15.0 mA g^{-1}, was in the passive region, while the other two samples underwent electrochemical dissolution at constant applied currents of 30.0 and 45.0 mA g^{-1} in the transpassive region.

Figure 5.2 presents the continuous long-term dissolution of the nickel samples under different current densities. Close to the final stages of the dissolution, when most of the sample had dissolved into the solution, the potential began to increase, which might be attributed to the decrease in the surface area and weight loss effect of the sample. To investigate the changes in electrochemical behavior of the surface over time at different stages of the long-term dissolution,

the CV behavior of a new nickel sample was studied at a constant applied current density of 30.0 mA g^{-1}, with the CV curves displayed in Figure 5.2. Based on these curves, it was clear that prior to the onset of the long-term dissolution, the current response was fairly low, which could be due to the presence of a few active sites on the surface or a lower active surface area, most likely due to a natural oxide on the surface. After running electrochemical dissolution for 10 hours, the population of active sites increased and attained the highest point throughout the process, which might have been due to an increased surface roughness via the formation of pores or active sites due to the dissolution of the surface oxides. Subsequently, by increasing the dissolution durations to 20 and 25 hours, the active sites continued to dissolve into the solution, which resulted in the decrease of current response in the CV curves.

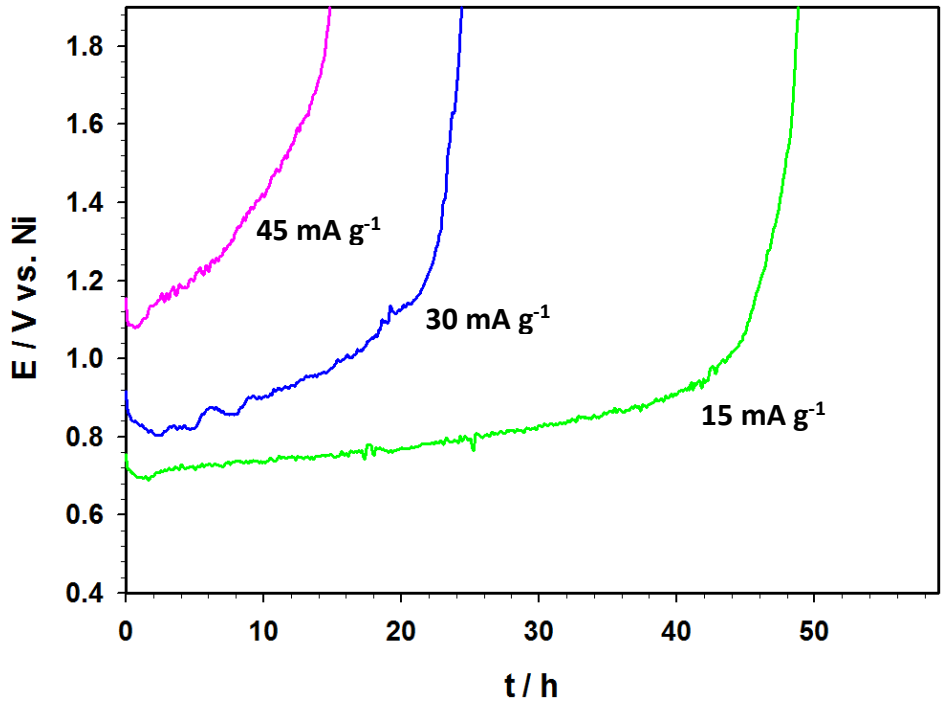

Figure 5.2 Long-term dissolution behavior of Ni sample in Watts solution at applied constant current densities of 15.0, 30.0, and 45.0 mA g^{-1}.

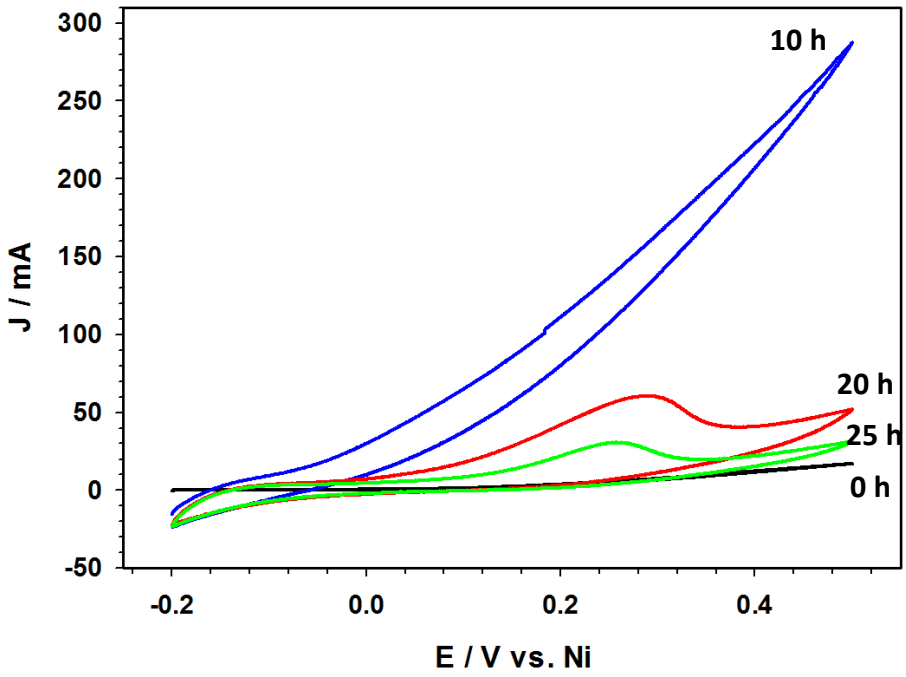

Figure 5.3 Cyclic voltammetry characterization of the nickel sample at different stages of long-term dissolution in Watts solution for a nickel sample undergoing dissolution at an applied constant current density of 30.0 mA g^{-1}.

Long-term electrochemical dissolution studies were conducted using a bigger electrolytic Ni electrode in Watts electrolyte at an applied current density of 8.0 mA cm^{-2}, which followed the same behavior as Figure 5.2. Primary electrochemical investigations on the electrolytic Ni electrode were completed, and the electrode potentials at different time intervals are listed in Table 5.1. Initially, upon the immersion of the nickel sample into the solution, the electrode potential of 0.34 V (vs. Ni) was obtained for the electrolytic Ni electrode at an applied current density of 8.0 mA cm^{-2}. By increasing the dissolution duration, from 0 to 608 h, the electrode potential was significantly increased from 0.34 to 0.75 V.

The impedance elements were monitored during the anodic dissolution of the electrolytic Ni electrode. EIS measurements were carried out at an applied potential of 0.3 V for the electrolytic

Ni electrode in Watts solution, with the impedance values also presented in Table 5.1. Prior to the onset of the long-term electrochemical dissolution, the R_p value for the electrolytic Ni electrode was obtained as 870.7 Ω cm^2, while the double layer capacitance (C_{dl}) was 1.68 mF cm^{-2}. The R_p value of the electrolytic Ni decreased from 870.7 to 46.9 Ω cm^2, and the C_{dl} value was increased from 1.68 to 135.80 mF cm^{-2} once the long-term dissolution had proceeded for ~608 h (25.3 days).

Table 5.1 Electrochemical data obtained during the long-term dissolution of electrolytic Ni material.

t / h	**E / V vs. Ni**	**R_p / Ω cm^2 @ 0.3V)**	**C_{dl} / mF cm^{-2}**	**η_A / %**
0	0.34	870.69	1.68	-
68	0.31	578.30	3.01	99.00
158	0.36	372.06	5.95	98.90
248	0.38	262.00	6.07	99.30
338	0.43	108.30	29.37	98.30
428	0.53	64.10	49.65	97.50
518	0.63	51.75	123.00	98.50
608	0.75	46.87	135.80	98.70

A decrease in R_p and increase in C_{dl} were observed with the long-term electrochemical dissolution of the electrolytic Ni electrode. The impedance results indicated that both the roughness and surface area were increased with the tunable kinetic barrier of the Ni electrodes via electrochemical anodic dissolution. The electrochemical properties with anodic and cathodic

efficiencies were also estimated and listed in Table 5.1. Anodic and cathodic efficiencies were calculated to be in the range of from 97% - 99% for the electrolytic Ni electrode.

5.3.2 Surface characterization of nickel samples

Macroscopic images of the sample that underwent long-term dissolution at different times during the process were obtained (Figure 5.4). In the later stages of the dissolution, the outer shell of the sample remained almost intact, except for the appearance of minor pores formed on the surface. This indicated that the dissolution occurred primarily underneath the external shell and within the sub-surface layers of the sample, which led to the formation of a sponge-like structure with lower mechanical strength. This is important, as under actual plating conditions, samples are piled up in a basket, which results in a high compressive pressure on the samples at the bottom of the pile. Therefore, weaker mechanical strength might translate to pulverization as well as residue formation. Consequently, this could add to the generation of residue build-up at the final stages of the dissolution process. These results are consistent with an additional study that involved nickel dissolution in a similar electrolyte [35], as only a handful of deep pits occurred on the surface and resulted in a lace-like morphology on the surface. In this case, the pits grew in a lateral direction beneath the surface of the metal, leading to what appeared to be a cluster of pits, while there was a very large void within the sample, with many pores to the outside. The dissolution typically began at the bottom edges of the samples and continued toward the side edges and center of the sample, which was most likely caused by breakdown of the films that were formed on the surface. It is not yet clear which sites are most susceptible to the initial degradation of the passive films [46].

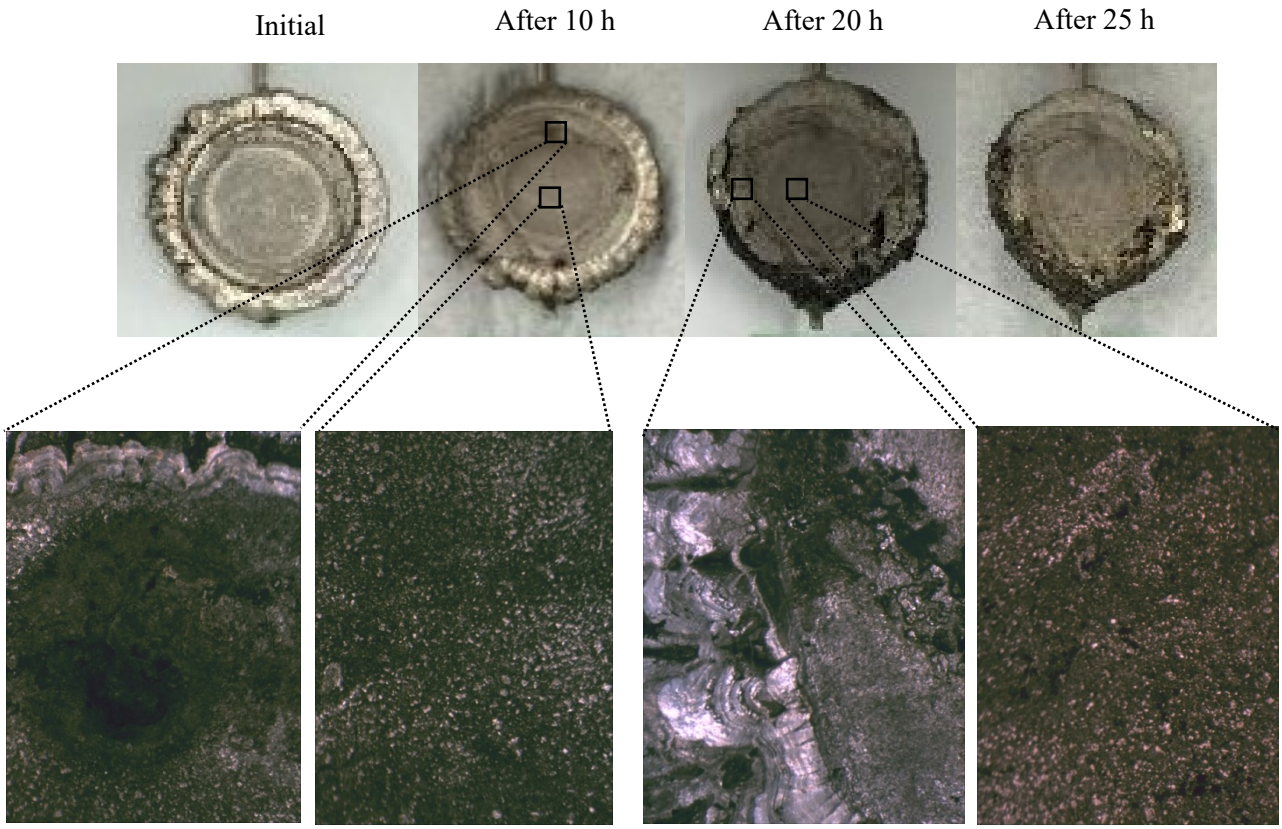

Figure 5.4 Macroscopic images of Ni sample at different stages of long-term dissolution at an applied constant current density of 30.0 mA g^{-1}.

It was demonstrated that nickel samples with few impurities had a tendency for surface passivation and dissolution via sublayers of the sample, rather than more uniform surface localized dissolution at the onset [35]. This was attributed to differences in surface states [40], variations in the surface geometry, local passivation by adsorbents, and/or the presence of dissolution accelerating anions [39], i.e. chlorides, which was the case in this study, as nickel chloride is an ingredient of Watts solution. These differences, in conjunction with a significant electric field (107-108 V m^{-1}) resulted in non-uniform rates of dissolution at different sites of the sample, where increasing the anodic aspect of the potential caused only the roughness of the surface to increase.

Further, the chloride anions that were present in the Watts solution tended to accelerate the active dissolution, which caused the passive layer to break down, resulting in the pitting type dissolution [47].

Based on the pH and chloride anion concentration of the solution, Ni dissolution rate might either increase or decrease [48]. During the localized dissolution of Ni, a series of complex reactions such as the diffusion of soluble species through the pores, and the precipitation of insoluble phases may occur. But a proposed simplified mechanism [49] for passive layer breakdown by aggressive anions (such as chloride ions) transpires as mentioned in the following steps: i) preferential competitive adsorption of aggressive anions over species such as H_2O or OH^-; ii) diffusion of halide anions through the oxide layer possibly via cracks (flaws) and binding with metal sites; iii) diffusion of halide ions through the metal oxide lattice and binding to metal sites; iv) adsorption of aggressive anions on the oxide film, thereby dissolving it. Another parameter that might be taken into consideration is the presence of oxygen in the electrolyte. At more positive potentials, oxygen evolution might also contribute to decreasing the pH within the pits, while increasing the dissolution rate [35].

Active and transpassive (pitting-like) dissolution on the surface and within the sub-layers of the Ni are the most common mechanisms that have been observed for the electrochemical dissolution of nickel [50]. The formation and growth of 3D pits is reported to be the dominant mechanism at more positive potentials. The localized dissolution of nickel in presence of the passive layer, which is due to the disruption of an inhibiting adlayer, could cause the formation of short-lived, highly active sites on the surface. Further dissolution and re-passivation might lead to pronounced pits along with increased surface roughness [39]. This is in agreement with the results of other studies [51] observed for bulk nickel, rather than the more uniform dissolution observed

in the case of nanocrystalline nickel. In other words, grain sizes and their distribution within the metal are another factor that may affect the dissolution behavior of the metal [51, 52]. It has been shown that samples with smaller grain sizes or samples with a broader range of grain sizes are more resistant to dissolution in non-passivating environments. This might be attributed to the higher density of grain boundaries in nanocrystalline structures, which would result in a more rapid diffusion rate of the ions to the surface, translating to the accelerated passivation of the surface [53].

The XRD patterns of the nickel sample, obtained at different stages of the long-term dissolution at an applied constant current density of 30.0 mA g^{-1} are depicted in Figure 5.5. All of the primary peaks, corresponding to face cubic center (FCC) nickel positioned at 2θ of 44.4, 51.7, 76.2, 92.8, and 98.5° were present in the sample. Based on the JCPDS database (PDF: 04-1027) the peaks could be assigned to (111), (200), (220), (311), and (222) planes of the FCC Ni, respectively. Also, as expected, the preferred orientations of the crystals were (111) and (200), where (111) was dominant. Furthermore, by increasing the dissolution time, the crystalline structure of the surface and sub-surface layers were altered toward decreasing the peak intensity ratio of the (111) plane to the (200) plane, from 1.96 (initial structure at t = 0 h) to 0.93 after 10 hours, and 0.66 after 25 hours, which meant that crystals with the (111) plane orientation on the surface, and close to surface, continued to degrade either into the solution, as nickel ions, or into the residue as fine particulates of nickel, which will be discussed shortly.

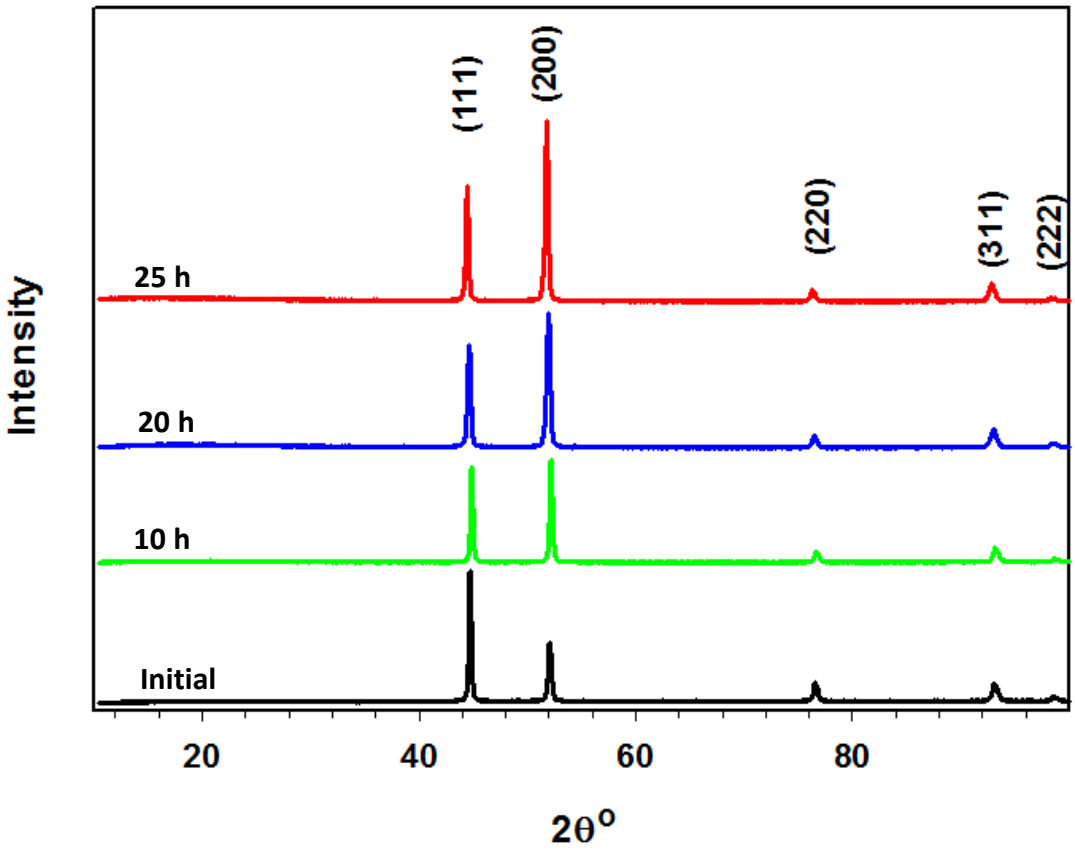

Figure 5.5 XRD patterns of the nickel sample at different stages of the long-term dissolution at an applied constant current density 30.0 mA g^{-1}.

5.3.3 Quantitative and qualitative characterization of the residue

The quantity of residue collected at different stages of the dissolution of the nickel sample which underwent CP at an applied constant current density of 30.0 mA g^{-1} is shown as a bar chart in Figure 5.6A. Following 10 hours of dissolution, there was no sign of residue, or the accumulated residue was insignificant. Once the process had continued for 20 hours, ~16 mg of fine particles had accumulated at the bottom of the container. As the process progressed, the amount of residue increased to ~77 mg at t = 25 h, which was ca. 4.8 times higher than what was collected after only

5 hours. In other words, by the time the dissolution was ~92% complete, in comparison to the point of 74% completion, the accrued residue increased by ~5 times. At the final stage of the dissolution, the total residue amounted to ~114 mg, which was ca. 1.5 times higher than that at t = 25 h. The same pattern of residue formation was observed for the other two samples that underwent dissolution at applied constant current densities of 15.0 and 45.0 mA g^{-1}, which revealed that the formation of the residue was independent of the applied current, and truly proceeded once the dissolution was closer to its final stages. This could be related to the way the sample dissolved from its sub-layers and from beneath the surface of the sample, as discussed earlier.

Most likely, the formation of the pits and their coalescence with increased time, and subsequently, the appearance of a lacy structure might have led to some parts of the sample being detached from all neighboring sites and falling into the solution. Figure 5.6B depicts (in a bar chart) the mass of the collected residue as a ratio of the mass loss of the sample through the process (dissolved/residue nickel) under different applied current densities. In general, the quantity of residue collected at the conclusion of the anodic dissolution process was increased with a higher applied current.

The percentage values of the mass of the formed residue, to the mass of the dissolved sample was ca. 0.37%, 0.49%, and 0.65% at applied current densities of 15.0, 30.0, and 45.0 mA g^{-1}, respectively. This behavior might be due to the formation of additional and larger interconnected pits and islands within the sample by increasing the current density. A more aggressive dissolution may commence as the result of a higher applied current density, which could likely lead to larger particles or more small and isolated segments of nickel falling to the bottom of the container.

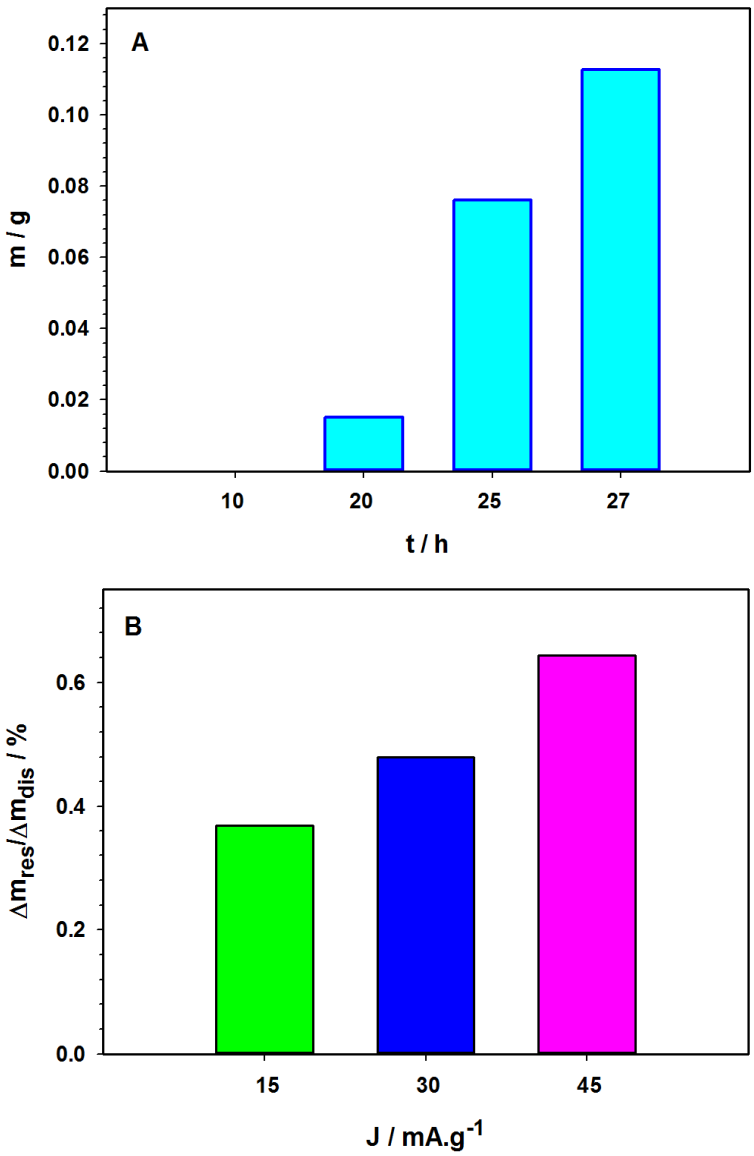

Figure 5.6 (A) Accumulation of residue at different stages of the long-term dissolution at an applied constant current density of 30.0 mA g^{-1}, and (B) mass ratio of collected residue to the mass loss of the sample that underwent dissolution under different applied constant current densities.

A SEM image of the collected residue at the conclusion of the long-term dissolution of nickel sample at an applied constant current density of 30.0 mA g^{-1} is presented in Figure 5.7. The images reveal that the segments dislodged from the samples had a fine particle size, with dimensions that varied from several micrometers to a few millimeters. Moreover, the EDS results confirmed that

the residue primarily consisted of nickel, while small amount of oxygen and carbon were detected. The presence of oxygen might have been due to portions of the surface oxide, or passive layer that sank to the bottom of the container as a result of the dissolution of neighboring active sites, and the formation of several pits or laces [35] around the passivated sites, causing the residues to accumulate. Further, the carbon could likely be present due to environmental contamination. It is noteworthy to mention that the presence of impurities was negligible in the composition of the residue. However, they might have played a trivial role in the dissolution of specific segments of the sample, or served to make certain segments more susceptible to dissolution and pit formation, followed by the neighboring pieces sinking to the bottom of the container.

XRD patterns of the collected residue following the long-term dissolution at different applied constant current densities are presented in Figure 5.8. Similar to the XRD pattern displayed for the nickel sample (Figure 4.8), all of the key peaks of the FCC nickel were present for the collected residue as well. The preferred crystalline phase of the nickel particles in the collected residue was the (111) plane. Further, there was a slight decrease in the peak intensity ratio of (111) plane to (200) plane, from 2.50 to 2.38, when the applied current density was decreased from 45.0 to 15.0 mA g^{-1}. However, the slight change between the ratios could fall well within the experimental error margin. The XRD pattern of the residue was also in agreement with the XRD pattern of the samples at the onset of the dissolution process. Therefore, it could mean that not all of the aforementioned nickel with the (111) plane was dissolved into the solution, as a portion of it might have migrated into the formed residue, which may have also occurred with the residue itself (i.e. same general structure as the starting material).

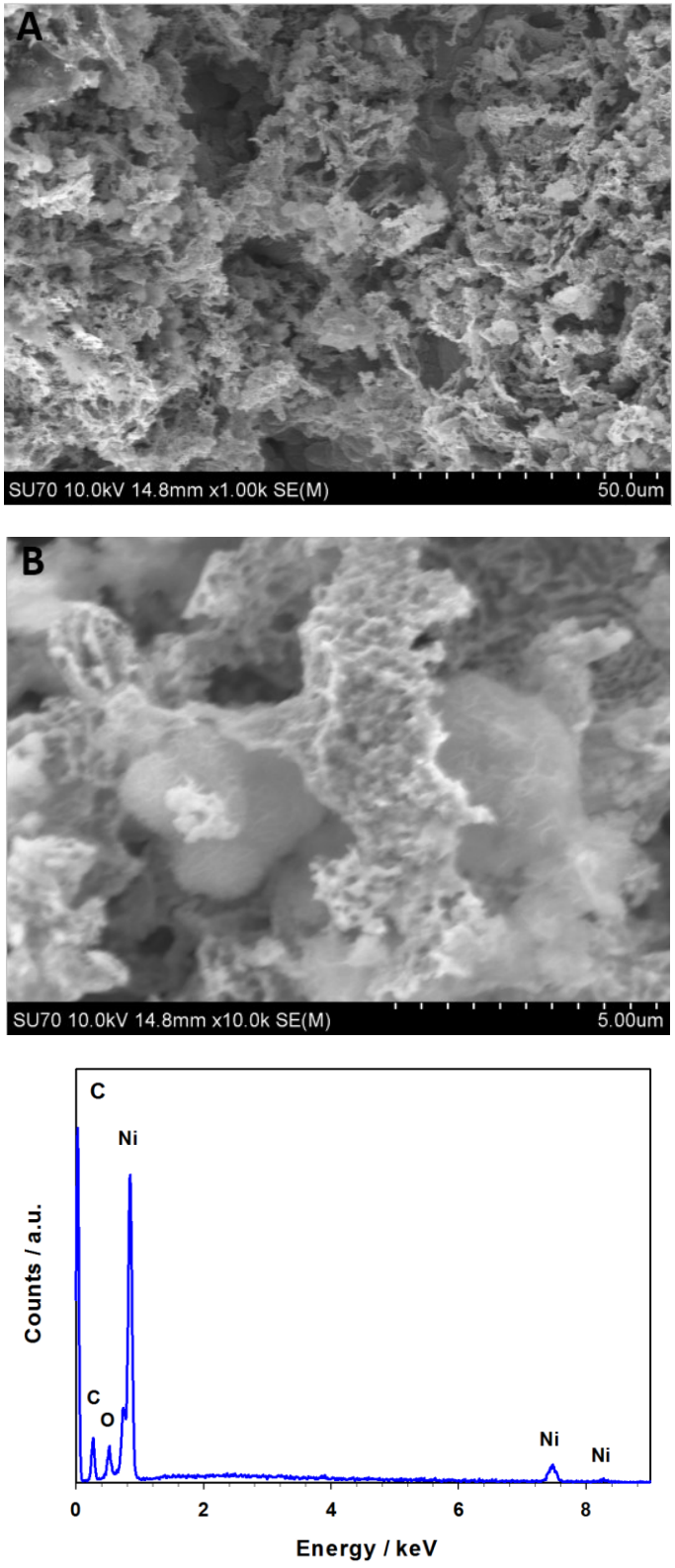

Figure 5.7 (A) & (B) SEM images at different magnifications, and (C) EDS of the residue collected at the end of the long-term dissolution at an applied constant current density of 30.0 mA g^{-1}.

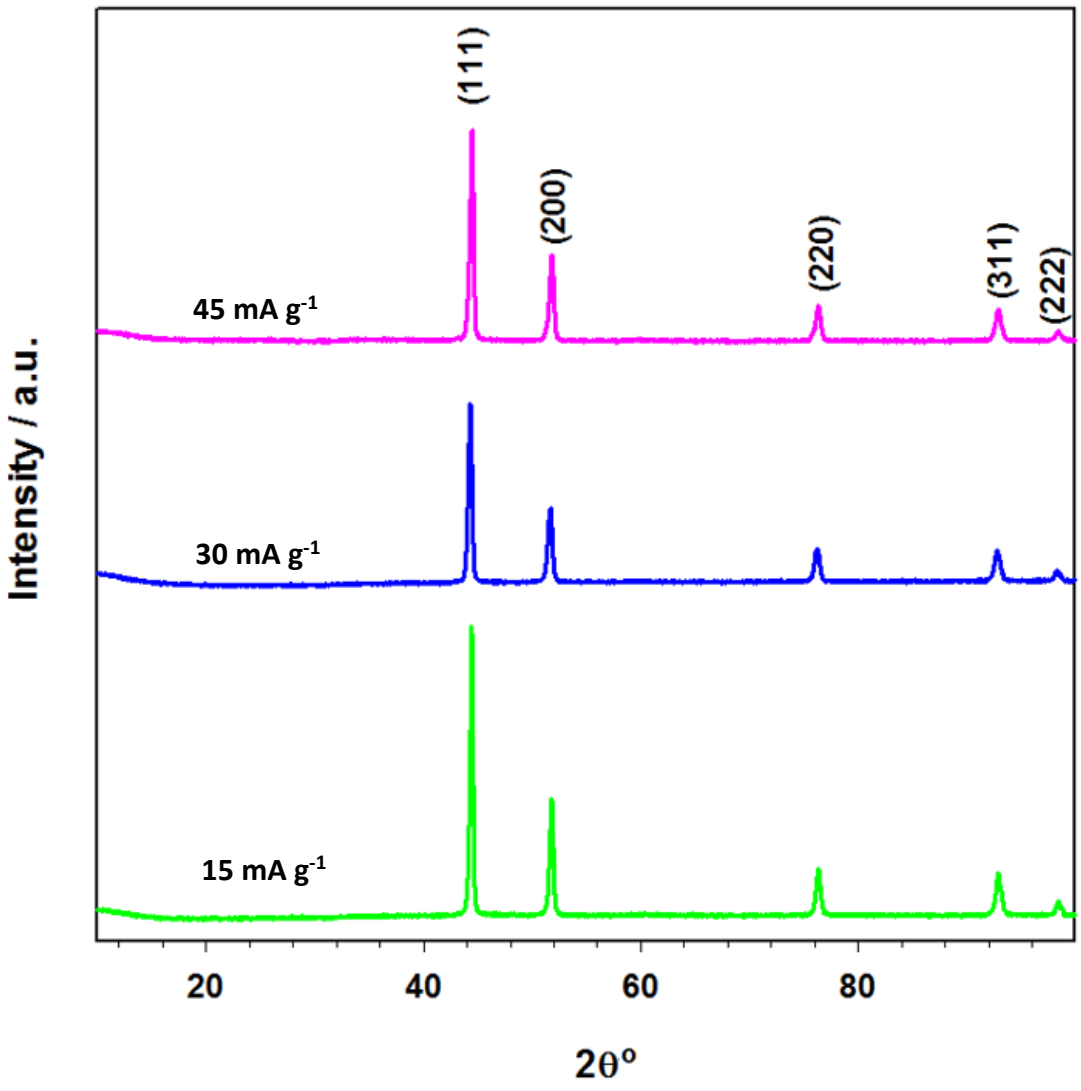

Figure 5.8 XRD of the residue collected at the end of the long-term dissolution under different applied constant current densities.

Finally, the conductivity of the collected residue was tested. The obtained residues generated under all of the current densities were confirmed to be conductive, which was in agreement with previous studies [35, 36]. This could mean that if electrical contact with these segments was somehow maintained, or the dissolution of the sample followed a more uniform pattern, there was

a good chance that these particles would dissolve into the solution, rather that ending up in the residue. Hence, perhaps the residue formation issue could be prevented.

5.4 Conclusions

The anodic dissolution of industrial electrolytic nickel chips under different applied constant current densities was studied to investigate residue formation behaviors and the possible effects of current density during the plating process. The CV studies indicated that the process of anodic dissolution began by activating the sample during the first stages. However, further dissolution resulted in reducing the number of active sites, which was caused by their dissolution. Also, at higher current densities (30.0 and 45.0 mA g^{-1}) anodic dissolution more likely occurred in the trans-passive region. This might potentially result in the lace-like dissolution of the sample; hence, falling out of neighboring disconnected nickel islands, and the formation of additional residue.

In general, the dissolution began from the sub-layers, edges and bottom of the sample, where only at final stages of the process; the surface of the sample was involved. This might mean that, as the process continued, the mechanical properties of the sample deteriorated. Under practical conditions, where the samples are in a basket, the weight of the samples at the top of the pile could result in pulverization of the lower samples. This could likely result in the generation of more residue than would be expected at the beginning of the process, if just one sample was involved. Also, there was slight decrease in residue formation with a decreased applied current. Therefore, lower current densities might be suitable for the initiation of uniform dissolution.

Based on the XRD patterns and residue analysis, it was shown that (111) oriented crystals were diminishing at a more rapid rate in contrast to (200) planes, thereby resulting in decreasing the

peak intensity of the (111)/(200) ratio. This might be indicative of a higher tendency of (111) oriented crystals to dissolve. However, most of the collected residue consisted primarily of (111) crystals as well. This could be explained by the formation of pits within the surface defects on the formed oxide layers, which were either formed during the passivation process in the solution, or the natural passive oxide that was formed in the ambient air prior to the use of the samples.

References

[1] M. Dinca, Y. Surendranath, D. G. Nocera, Nickel-borate oxygen-evolving catalyst that functions under benign conditions, *PNAS*, 2010 , **107**, 10337–10341.

[2] A. R. Sheik, M. K. Ghosh, K. Sanjay, T. Subbaiah, B. K. Mishra, Dissolution kinetics of nickel from spent catalyst in nitric acid medium, *J. Taiwan Inst. Chem. Engr.*, 2013, **44**, 34–39.

[3] C. A. Sequeira, D. S. Cardoso, L. Amaral, B. Šljukić, D. M. Santos, On the performance of commercially available corrosion-resistant nickel alloys: a review, *Corros. Rev.,* 2016, **34**,187-200.

[4] C. Gu, J. Lian, J. He, Z. Jiang, Q. Jiang, High corrosion-resistance nanocrystalline Ni coating on AZ91D magnesium alloy, *Surf. Coat. Tech.*, 2006, **200**, 5413–5418.

[5] B. Liu, X. Wei, W. Wang, J. Lu, J. Ding, Corrosion behavior of Ni-based alloys in molten NaCl-$CaCl_2$-$MgCl_2$ eutectic salt for concentrating solar power, *Sol. Energ. Mat. Sol. Cells*, 2017, **170**, 77-86.

[6] C. Whittington, I. Rose, Nickel plating handbook, Nickel Institute, Brussels, 2014, 5.

[7] T. A. Dar, A. Agrawal, R. J. Choudhary, P. Sen, Electrical and magnetic transport properties of undoped and Ni doped ZnO thin films, *Thin Solid Films*, 2015, **589**, 817–821.

[8] D. Lei, D. C. Lee, A. Magasinski, E. Zhao, D. Steingart, G. Yushin, Performance enhancement and side reactions in rechargeable nickel–iron batteries with nanostructured electrodes, *ACS Appl. Mater. Interfaces*, 2016, **8**, 2088-2096.

[9] I. G. Casella, M. Gatta, Electrodeposition and characterization of nickel-copper alloy films as electrode material in alkaline media, *J. Electrochem. Soc.*, 2002, **149**, 465-471.

[10] K. Watanabe, T. Kikuoka, N. Kumagai, Physical and electrochemical characteristics of nickel hydroxide as a positive material for rechargeable alkaline batteries, *J. Appl. Electrochem.*, 1995, **25**, 219-226.

[11] H. Luo, B. Wang, Y. Li, T. Liu, W. You, D. Wang, Core-shell structured Fe_3O_4@ NiS nanocomposite as high-performance anode material for alkaline nickel-iron rechargeable batteries, *Electroch. Acta*, 2017, **231**, 479-86.

[12] J. Chen, D. H. Bradhurst, S. X. Dou, H. K. Liu, Nickel hydroxide as an active material for the positive electrode in rechargeable alkaline batteries, *J. Electrochem. Soc.*, 1999, **146**, 3606-3612.

[13] A. Valenzuela-Muñiz, G. Alonso-Nuñez, G. Botte, M. Miki-Yoshida, Y. Verde-Gomez, Influence of nickel on the electrochemical activity of PtRu multiwalled carbon nanotubes electrocatalysts for direct methanol fuel cells, *J. Appl. Electrochem.*, 2014, **44**, 695-700.

[14] W. Yang, S. Yang, W. Sun, G. Sun, Q. Xin, Nanostructured silver catalyzed nickel foam cathode for an aluminum–hydrogen peroxide fuel cell, *J. Power Sources*, 2006, **160**, 1420–1424.

[15] Z. Jiao, A. Ueno, Y. Suzuki, N. Shikazono, Study on the influences of reduction temperature on nickel-yttria-stabilized zirconia solid oxide fuel cell anode using nickel oxide-film electrode, *J. Power Sources*, 2016, **328**, 377-384.

[16] B. C. H. Steele, A. Heinzel, Materials for fuel-cell technologies, *Nature*, 2001, **414**, 345-352.

[17] J. Zhang, F. Liu, J. P. Cheng, X. B. Zhang, Binary nickel-cobalt oxides electrode materials for high-performance supercapacitors: influence of its composition and porous nature, *Appl. Mater. Interfaces*, 2015, **7**, 17630–17640.

[18] H. J. Qiu, L. Peng, X. Li, Y. Wang, Enhanced supercapacitor performance by fabricating hierarchical nanoporous nickel/nickel hydroxide structure, *Mater. Lett.*, 2015, **158**, 366–369.

[19] X. Wang, X. Han, M. Lim, N. Singh, C. L. Gan, M. Jan, P. S. Lee, Nickel cobalt oxide-single wall carbon nanotube composite material for superior cycling stability and high-performance supercapacitor application, *J. Phys. Chem. C*, 2012, **116**, 12448–12454.

[20] P. K. Kannan, C. S. Rout, High performance non-enzymatic glucose sensor based on one-step electrodeposited nickel sulfide, *Chem. Eur. J.*, 2015, **21**, 9355-9359.

[21] Y. M. Sabri, S. J. Ippolito, A. J. Atanacio, V. Bansal, S.K. Bhargava, Mercury vapor sensor enhancement by nanostructured gold deposited on nickel surfaces using galvanic replacement reactions, *J. Mater. Chem.*, 2012, **22**, 21395-21404.

[22] P. Wu, J. H. Sun, Y. Y. Huang, G. F. Gu, D. G. Tong, Solution plasma synthesized nickel oxide nanoflowers: An effective NO_2 sensor, *Mater. Lett.*, 2012, **82**, 191-194.

[23] A. C. C. Tseung, S. Jasem, Oxygen evolution on semiconducting oxides, *Electrochem. Acta*, 1977, **22**, 31-34.

[24] J. Gregori, J. J. Garcia-Jareno, F. Negrete, M. P. Pena, C. Sanz, J. Subiela, F. Vicente, Electrochemical dissolution and passivation of nickel powder randomly dispersed in a graphite + polypropylene matrix, *J. Appl. Electrochem.*, 2007, **37**, 241-248.

[25] X. Wang, H. Luo, H. Yang, P. J. Sebastian, S.A. Gamboa, Oxygen catalytic evolution reaction on nickel hydroxide electrode modified by electroless cobalt coating, *Int. J. Hydrogen Energ.*, 2004, **29**, 967-972.

[26] G. Wu, W. Chen, X. Zheng, D. He, Y. Luo, X. Wang, J. Yang, Y. Wu, W. Yan, Z. Zhuang, X. Hong, Hierarchical Fe-doped NiO_x nanotubes assembled from ultrathin nanosheets containing trivalent nickel for oxygen evolution reaction, *Nano Energy*, 2017, **38**, 167-174.

[27] B. Singh, Treatment of spent catalyst from the nitrogenous fertilizer industry-A review of the available methods of regeneration, recovery and disposal, *J. Hazard. Mater.*, 2009, **167**, 24–37.

[28] N. M. Al-Mansi, N. M. Abdel Monem, Recovery of nickel oxide from spent catalyst, *Waste Manage.*, 2002, **22**, 85-90.

[29] Y. Ishida, K. Kumabe, K. Hata, K. Tanifuji, T. Hasegawa, K. Kitagawa, N. Isu, Y. Funahashi, T. Asai, Selective hydrogen generation from real biomass through hydrothermal reaction at relatively low temperatures, *Biomass Bioenerg*., 2009, **33**, 8-13.

[30] K. K. Sahu, A. Agarwal, B. D. Pandey, Nickel recovery from spent nickel catalyst, *Waste Manage. Res.*, 2005, **23**,145-154.

[31] A. Watt, A. Philip, Electroplating and electrorefining of metals, Watchmaker Publishing, 2005, 630.

[32] H. T. Brown, P. G. Mason, Electrowinning of nickel at the Bindura Smelting and Refining Company, *J. South Afr. Inst. Min. Metall.*, 1977, **7**, 143-145.

[33] V. Zentner, A. Brenner, C. W. Jennings, Physical properties of electrodeposited metals, *AES Res. Rep.*, 1952, **39**, 865.

[34] G. D. Bari, Surface Engineering, ASM Handbook, ASM International, Materials Park, 1994, 201.

[35] M. G. Moula, G. Szymanski, B. Shobeir, H. Huang, I. J. Burgess, A. Chen, J. Lipkowski, Electrochemical dissolution behavior and the residue formation mechanism of laboratory made carbonyl nickel, *Electrochim. Acta*, 2015, **162**, 108–118.

[36] C. M. Whittington, K. L. K. Yeung, W. Y. Lo, Refined nickel anodes: pointers to industrial best practice, *Trans. Inst. Met. Finish.*, 2011, **89**, 122-131.

[37] M. Itagaki, H. Nakazawa, L. Watanabe, K. Noda, Study of dissolution mechanisms of nickel in sulfuric acid solution by electrochemical quartz crystal microbalance, *Corros. Sci.*, 1997, **39**, 901-911.

[38] B. MacDougall, M. Cohen, Anodic oxidation of nickel in neutral sulfate solution, *J. Electrochem. Soc.*, 1974, **121**, 1152-1159.

[39] J. Scherer, B. M. Ocko, O. M. Magnussen, Structure, dissolution, and passivation of Ni (111) electrodes in sulfuric acid solution: an in situ STM, X-ray scattering, and electrochemical study, *Electrochim. Acta*, 2003, **48**, 1169-1191.

[40] S. S. Abd El Rehim, S. M. Abd El Wahaab, E. A. Abdel Maguid, Electrochemical behaviour of nickel anode in H_2SO_4 solutions and the effect of halide ions, *Mater. Corros.*, 1986, **37**, 550-555.

[41] A. Seyeux, V. Maurice, L. H. Klein, P. Marcus, In situ scanning tunnelling microscopic study of the initial stages of growth and of the structure of the passive film on Ni (111) in 1 mM $NaOH_{(aq)}$, *J. Solid State Electrochem.*, 2005, **9**, 337–346.

[42] S. Hinnov, J. Tamm, The effect of halide ions on nickel corrosion in perchloric acid solutions, *Proc. Estonian Acad. Sci.*, 2011, **60**, 184–192.

[43] D. Zuili, V. Maurice, P. Marcus, Surface structure of nickel in acid solution studied by in-situ scanning tunneling microscopy, *J. Electrochem. Soc.*, 2000, **147**, 1393-1400.

[44] Y. Liang, P. M. A. Sherwood, D. K. Paul, Valence and core photoemission of the films formed electrochemically on nickel in sulfuric acid, *J. Chem. Soc. Faraday Trans.*, 1994, **90**, 1271-1278.

[45] B. MacDougall, D. F. Mitchell, M. J. Graham, Changes in oxide films on nickel during long-term passivation, *J. Electrochem. Soc.*, 1985, **132**, 2895-2898.

[46] B. MacDougall, M. Cohen, The effect of cathodic treatment on nickel dissolution, *J. Electrochem. Soc.,* 1975, **122**, 383-385.

[47] A. B. Shein, O. S. Ivanova, R. N. Minkh, The effect of anions on the anodic dissolution of nickel silicide in sulfate electrolytes, *Prot. Met.*, 2008, **44**, 32–38.

[48] T. H. Nguyen, R. T. Foley, On the mechanism of pitting of aluminum, *J. Electrochem. Soc.*, 1979, **126**, 1855-1860.

[49] M. Nakamura, N. Ikemiya, A. Iwasaki, Y. Suzuki, M. Ito, Surface structures at the initial stages in passive film formation on Ni (111) electrodes in acidic electrolytes, *J. Electroanal. Chem.*, 2004, **566**, 385-391.

[50] R. Mishra, R. Balasubramaniam, Effect of nanocrystalline grain size on the electrochemical and corrosion behavior of nickel, *Corros. Sci.*, 2004, **46**, 3019–3029.

[51] S. Gollapudi, Grain size distribution effects on the corrosion behaviour of materials, *Corros. Sci.*, 2012, **62**, 90-94.

[52] W. Zeiger, M. Schneider, D. Scharnweber, H. Worch, Corrosion behaviour of a nanocrystalline FeA18 alloy, *Nanostruct. Mater.*, 1995, **6**, 1013-1016.

[53] M. Turner, G. E. Thompson, P. A. Brook, The anodic behaviour of nickel in sulphuric acid solutions, *Corros. Sci.*, 1973, **13**, 991-990.

Chapter 6: Facile Synthesis of a Novel Carbon Nitride/Reduced Graphene Oxide/Nickel Hydroxide Nanocomposite for Oxygen Reduction in Alkaline Media*

6.1 Introduction

The demand for clean energy as well as energy efficient systems has increased significantly in recent years due to limited fossil fuel resources and environmental pollution that is caused by traditional energy production methods [1]. Fuel cells, such as direct methanol fuel cells, and proton-exchange membrane fuel cells have strong potential for replacing common strategies owing to their low/zero emission, high energy conversion efficiency, and environmental compatibility [2]. However, the major obstacles against the commercialization of these fuel cells are a low reaction rate for the oxygen reduction reaction (ORR), insufficient durability and high cost of cathode materials [3]. Platinum, its alloys, and platinum containing materials are typically employed as cathode materials due to their high catalytic activity toward the ORR [4]. Nevertheless, its high cost, scarcity, low tolerance to fuel crossover and CO poisoning have resulted in the shifting of research focus to the design and synthesis of new candidate materials for use as cathodes [5].

Various carbon-based materials such as single/multi-walled carbon nanotubes [6], graphene or reduced graphene oxide (rGO) [7], carbon black [8], graphitic carbon nitride compounds [9], or doped carbon or graphene [10] have been widely utilized as support materials for different catalysts [11]. Not only do these materials increase the active surface area significantly, but also facilitate

* Most of the results presented in this chapter have been published in *ChemElectroChem* **2017**, *4*, 997-1001.

improvements in electron transfer due to their conductive nature. Graphene and rGO demonstrate exceptional mechanical and electrical features, while offering a high surface area [12]. Further, their 2D planar structure facilitates exceptional electron transfer properties [13]. Their properties also assist with the suppression of the aggregation of nanoparticles, as well as hindering the electrochemical degradation of metals by an order of magnitude or more [14]. Binary carbon nitrides are another carbon-based material that have garnered considerable attention due to their promising potential for high performance in various applications such as biosensing or electrocatalysis [15], which is believed to be due to the incorporation of nitrogen [16]. Graphitic carbon nitride (g-C_3N_4) is the most stable allotrope of carbon nitride under ambient conditions, which possesses a 2D stacked structure that is similar to graphite. It is also environmentally compatible and is available at a fairly low cost thanks to precursors such as urea [17]; however, it suffers from poor conductivity [16]. Recent studies have shown that transition metals in combination with different types of carbon materials result in significant improvement in electrocatalytic activity [18].

The fact that nickel is one of the earth-abundant transition metals along with its catalytic characteristics has made it attractive for various studies. Nickel oxide [19] and nickel hydroxide [20] have proven to be good catalysts for various applications under different environments [21]. In the present work, we developed a feasible and cost-effective one-step process to synthesize new nanocomposites via the simultaneous reduction of graphene oxide (GO) sheets while forming $Ni(OH)_2$ in the presence of g-C_3N_4. Remarkably, the $Ni(OH)_2$/C_3N_4/rGO (NCG) nanocomposite exhibited high catalytic activity for ORR in terms of high current density and low overpotential, which is comparable to the benchmark commercial Pt/C electrode. More importantly, the NCG nanocomposite was much more durable in comparison to the commercial Pt/C.

6.2 Experimental section

Graphene oxide (4 mg mL^{-1}), nickel chloride ($NiCl_2.6H_2O$, > 98%), and Nafion (10%) were purchased from Sigma-Aldrich. All other chemicals were of analytical grade and used as received. The fabrication of the NCG nanocomposite was achieved by casting the precursors from a stock solution onto a glassy carbon electrode (GCE), following the *in-situ* electrochemical reduction of GO and Ni precursors. The g-C_3N_4 sample was prepared using a facile combustion method as described in our previous study [22]. The GCE surface was polished with alumina powder (0.5 μm) followed by sonication in pure water for 1 min. A 100 μL mixture of GO (0.25 mg mL^{-1}), $NiCl_2.6H_2O$ (5-15 mM), g-C_3N_4 (0.5 mg mL^{-1}) and Nafion (10%) was casted onto the GCE and then allowed to air dry. The electrochemical procedures were performed using a three-electrode setup with Pt as counter and Ag/AgCl as reference electrodes. In order to convert potential values to reversible hydrogen potential (RHE) values, the following equation was employed:

$$E_{RHE} = E_{Ag/AgCl} + 0.059\ pH + E^{o}_{Ag/AgCl}\ ;\ E^{o}_{Ag/AgCl}\ (at\ T = 25\ ^{o}C) = 0.1976\ V$$

The *in-situ* formation of the nanocomposites on the GCE was achieved using cyclic voltammetry (CV) performed in 0.1 M KOH by running 20 cycles within the reducing electrode potential between 0.765 V and -0.035 V (vs. RHE) at 10 mV s^{-1} scan rate. For comparison purposes, electrodes consisting of only $Ni(OH)_2$, C_3N_4/rGO (CG), $Ni(OH)_2/C_3N_4$ (NC), $Ni(OH)_2$/rGO (NG) and $Ni(OH)_2/C_3N_4$/rGO with varying Ni concentrations were prepared using the identical electrochemical approach. For electrochemical studies, a VoltaLab PGZ 402 potentiostat was employed and all the studies were carried out in 0.1 M KOH solution. Scanning electron microscopy (SEM) and energy-dispersive X-ray spectroscopy (EDS) (Hitachi SU-70), infrared spectroscopy (FTIR), X-ray photoelectron spectroscopy (XPS), were employed for

surface characterization. The XPS measurement was carried out with a takeoff angle regarding the horizontal surface was 90° and monochromatic Al Kα X-ray source of 400 μm spot size was used. Charge compensation was measured, and the spectrum was corrected using the position of C1s main peak (C–C) at 284.6 eV. XPSpeak software was used for deconvolution of the spectra.

6.3 Results and discussion

6.3.1 Surface morphology and elemental analysis of the modified electrode

Figure 6.1A-C are scanning electron microscopic (SEM) images, whereas Figure 6.1D is the energy-dispersive X-ray spectra (EDS) of the as-synthesized nanoporous g-C_3N_4, reduced graphene oxide sheets, and NCG nanocomposite, which verified that the existence of all the constituents of the elements were accounted for in the composite. It is worth mentioning that the F peak in the EDS was derived from Nafion, which was used as the binding agent. The average dimension of the nickel hydroxide particles was estimated to be ~ 30 nm.

Figure 6.2 displays the scanning transmission electron microscopic (STEM) image of the NCG nanocomposite and the corresponding EDS mapping. Nanoparticles and nanosheets were clearly observed in the STEM image. As shown in the EDS mappings, the elements C, N, Ni and O were well distributed; and the variations of their intensity were consistent with the amount of the nanocomposite allocated on the spots as seen in the STEM image. The X-ray photoelectron spectra of the NCG presented in Figure 6.3 are in good agreement with the EDS results. As the XPS peak of F overlaps with the Ni peak, Nafion was not added when we prepared the sample for the XPS analysis. The doublets of Ni 2p1/2 and 2p3/2 transitions in the 850 – 890 eV region are shown in Figure 6.3B. The main peaks at ca. 855.6 and 873.4 eV with intense satellite peaks at ca. 861.2

and 879.5 eV are both characteristic of Ni^{2+} ions in $Ni(OH)_2$. The less intense peaks centered at 857.3 and 874.8 eV and their following satellites are an indication of the formation of a small amount of NiOOH as well. Furthermore, the oxygen peak at 531.5 eV, which is related to presence of hydroxyls corroborates with the formation of nickel hydroxide [23].

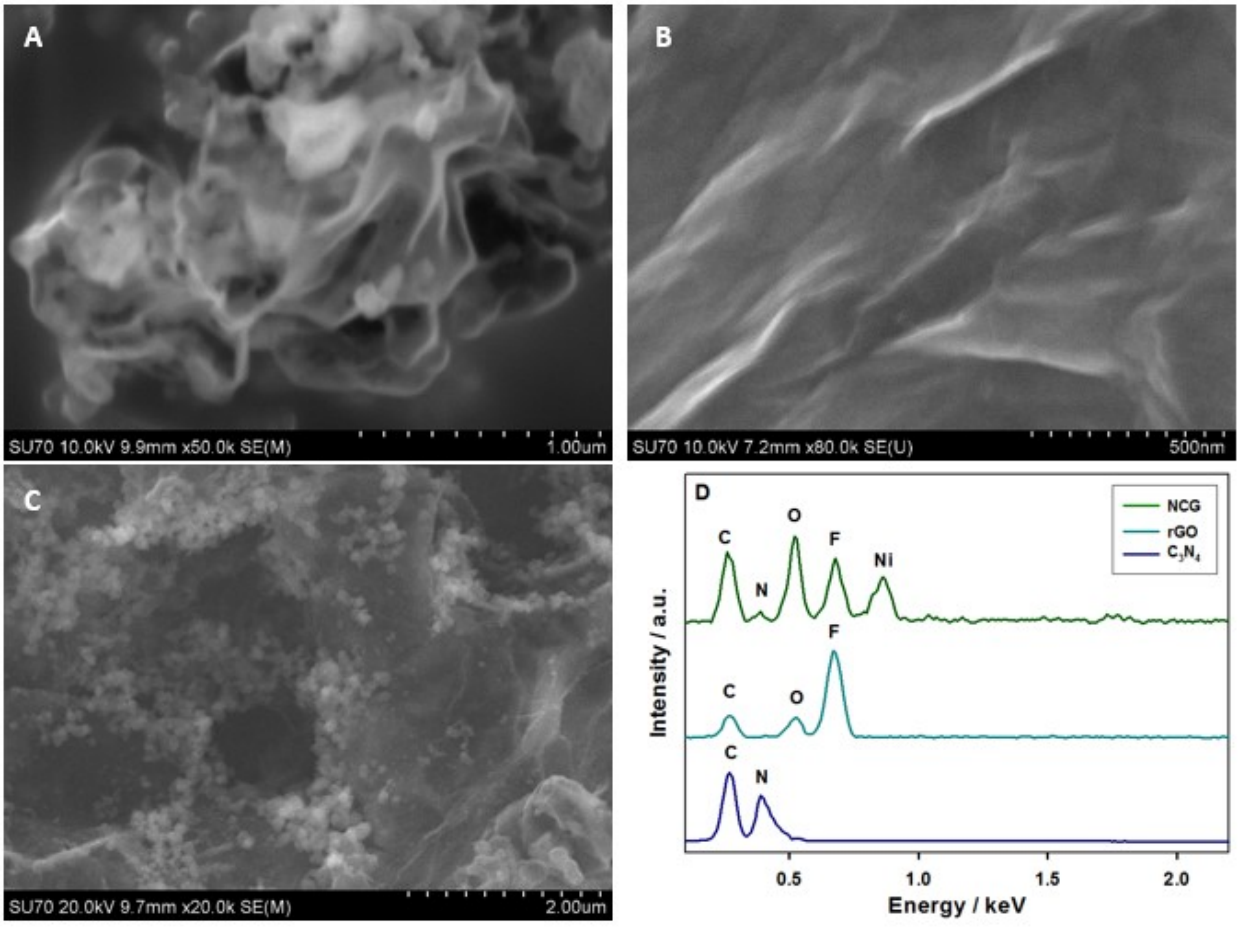

Figure 6.1 SEM images of (A) C_3N_4, (B) rGO sheets, (C) NCG nanocomposite, and (D) EDS of the C_3N_4, rGO, and NCG nanocomposite.

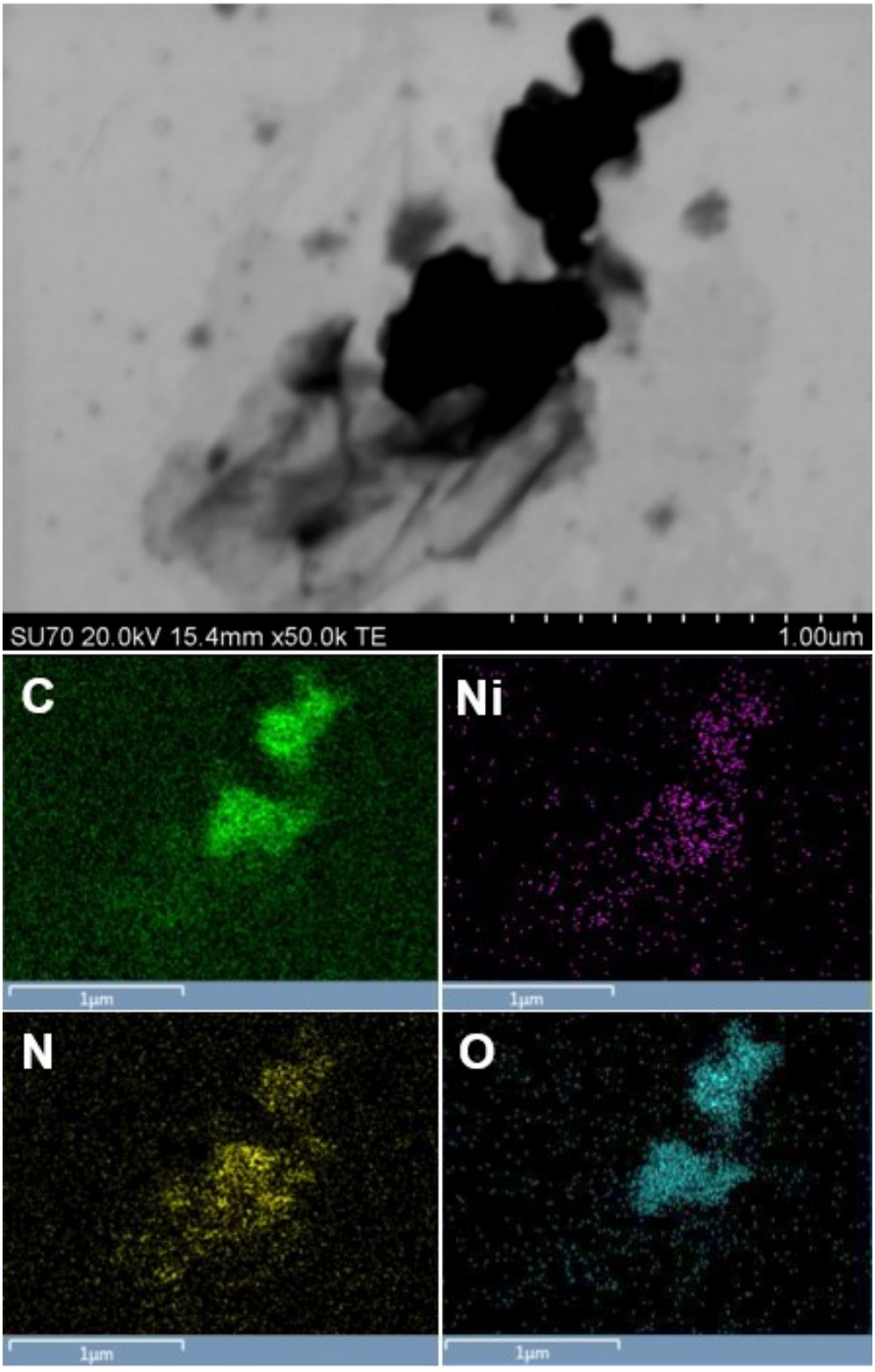

Figure 6.2 STEM image and EDS mapping of the NCG nanocomposite showing presence of Ni, C, O and N.

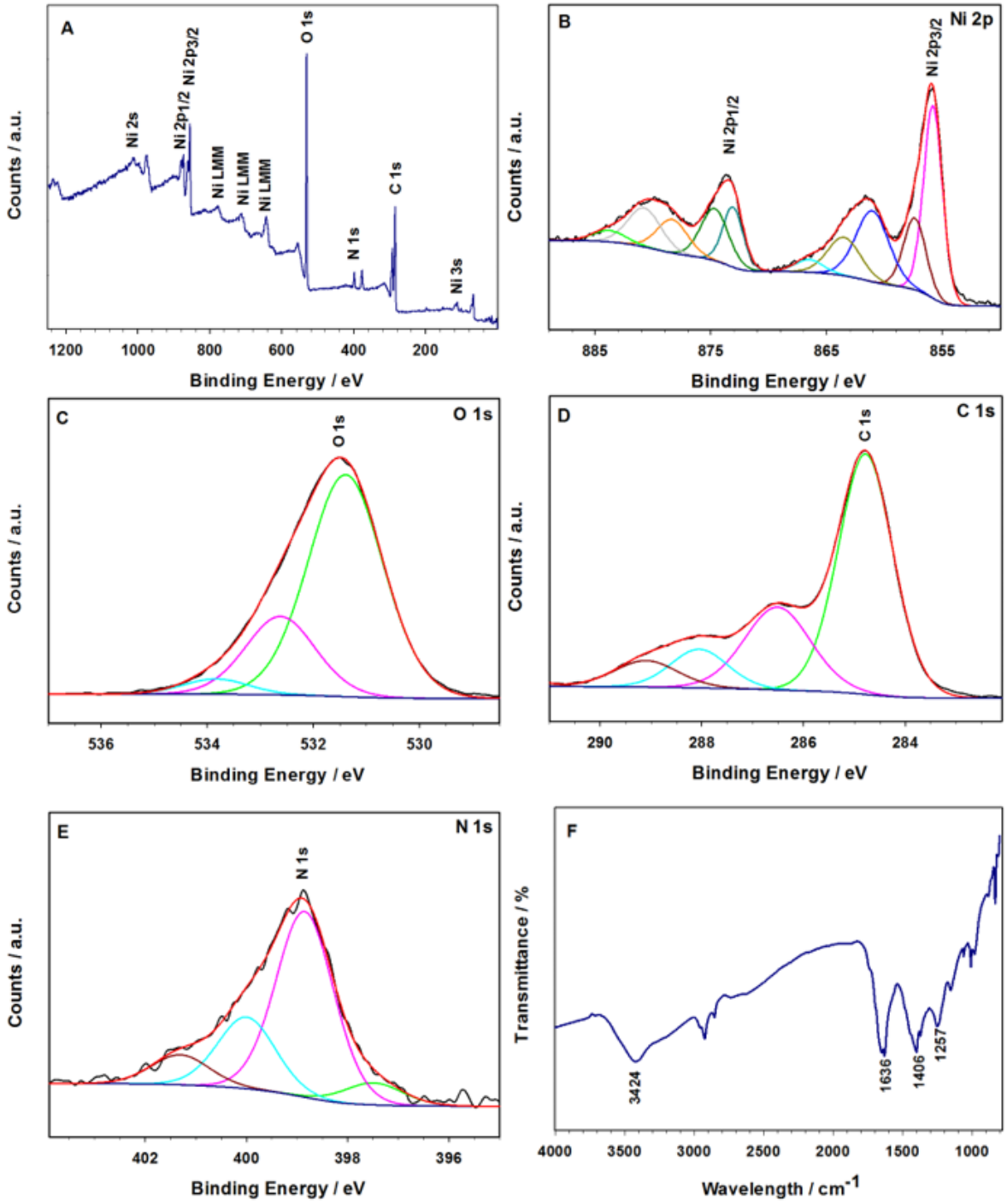

Figure 6.3 The survey scan (A) and high resolution XPS spectra and the fitted curves of (B) Ni 2p, (C) O 1s, (D) C 1s, (E) N 1s of the NCG nanocomposite, and (F) FTIR spectrum of NCG.

The high-resolution carbon scan indicated the presence of sp^2 C-C bonds at 284.7 eV, C–O or C–N at 286.7 eV, C=O or C=N at 288.3 eV, and O=C–O at 289.3 eV [24]. The intense C-C peak is the indication of reduction of the majority of graphene oxide in the composite. The high-resolution N 1s spectrum indicated that the N 1s may be present in four different component peaks, at 397.6, 398.6, 399.8, and 401.2 eV corresponding to N in a C_3N_4 structure, graphitic nitrogen, pyrrolic, and N–H groups, respectively [25]. The functional groups present in the as-synthesized NCG were characterized by Fourier transform infrared spectroscopy (FTIR) in Figure 6.3F. Several distinct bands in the range of 1200–1700 cm^{-1} may be observed, i.e. the peaks at ca. 1257, 1406, and 1636 cm^{-1}, which belong to the typical stretching modes of CN heterocycles in C_3N_4. The absorption at ~1630 cm^{-1} is attributed to C=N stretching. The bands at 1257 and 1406 cm^{-1} correspond to C–N aromatic stretching. The broad band at 3150-3500 cm^{-1} belongs to the stretching modes of uncondensed amine groups of $–NH_2$ or =NH groups [26].

6.3.3 Electrochemical studies of the modified electrodes

To study the electrochemical behavior of the NCG nanocomposite towards the oxygen reduction reaction (ORR), Figure 6.4 displays cyclic voltammograms (CVs) recorded in the Ar-saturated or the O_2-saturated 0.1 M KOH solution at room temperature, indicating that the onset potential for ORR was ~ 0.97 V vs. RHE. The ORR current was significantly increased when the potential was scanned from 0.97 to 0.85 V, and reached the peak current at ~ 0.8 V.

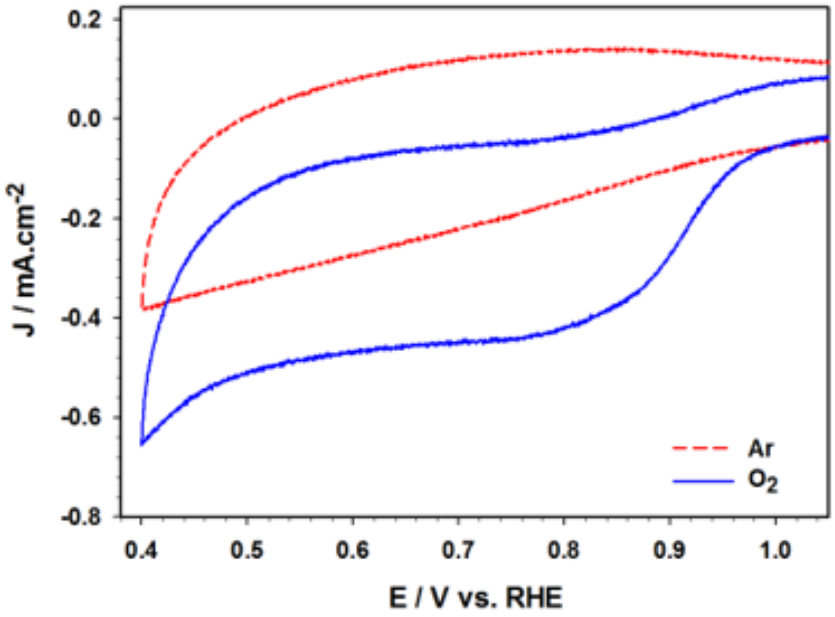

Figure 6.4 Cyclic voltammograms of NCG recorded in Ar- or O_2-saturated 0.1 M KOH at a scan rate of 50 mV s^{-1}.

As presented in Figure 6.5, the linear sweep voltammograms (LSVs) of the $Ni(OH)_2$, C_3N_4/rGO (CG), $Ni(OH)_2$/C3N_4 (NC), $Ni(OH)_2$/rGO (NG) and NCG were recorded in the Ar-purged solution (dotted lines) and in the O_2-saturated electrolyte (dashed lines) and the individual subtracted curves (solid line). The LSVs of the GCE, $Ni(OH)_2$, NC and NCG electrodes were almost identical prior to and after the subtraction; while the ORR current densities of the NC and NG electrodes were slightly decreased after the subtraction of the background current measured in the Ar-purged solution.

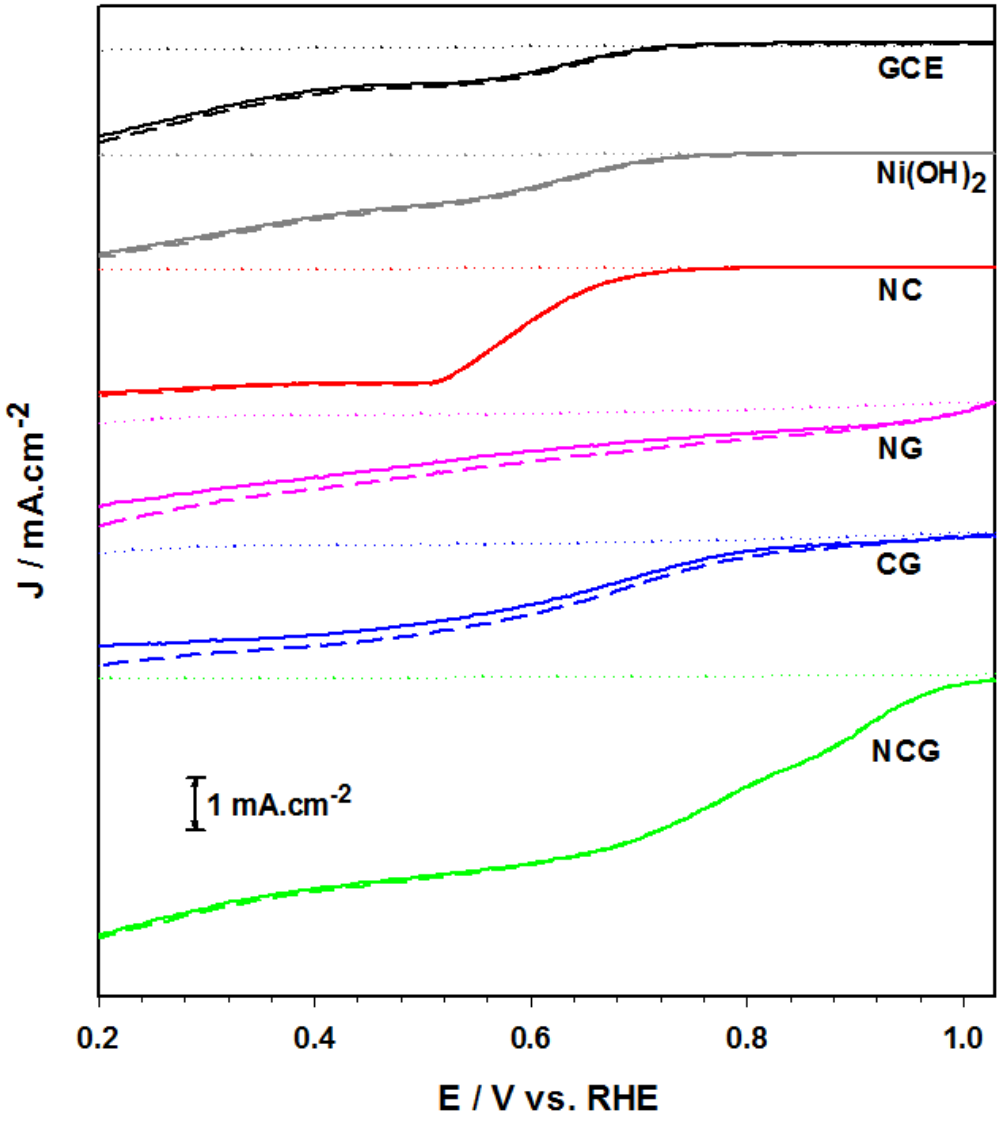

Figure 6.5 Linear sweep voltammograms of various electrodes recorded in Ar-saturated (dotted line) or O_2-saturated (dashed line) 0.1 M KOH and their subtraction (solid line). Rotating speed: 1600 rpm; scan rate: 50 mV s^{-1}.

The subtracted LSVs of all the electrodes are compared and presented in Figure 6.6A. For comparison, the LSV of a commercial 10 wt.% Pt/C was also included. NCG exhibited a pronounced catalytic activity, close to Pt/C. The onset potential of the NCG nanocomposite was

much more positive than that of $Ni(OH)_2$ (~ 0.73 V) and CG (0.80 V). In addition, the ORR current density of the NCG nanocomposite was much higher than that of nickel hydroxide combined with either rGO or g-C_3N_4, showing a strong synergistic effect of the nanocomposition. No clear limiting current was attained for the NCG nanocomposite, which might be attributed to the further reduction of some functional groups of the rGO [27, 28].

Inductively coupled plasma atomic emission spectroscopy (ICP-AES, Varian Vista Pro) was employed to analyze the 0.1 M KOH solution before and after the electrochemical fabrication process. No nickel leached from the electrode surface to the solution was evident, confirming that all the casted nickel ions on the GC electrode remained after the electrochemical fabrication process. The optimal amount of Ni precursor loading for ORR in NCG was also studied (shown in Figure 6.6B), which proved to be 0.37 mg cm^{-2} (44 wt.%). The catalytic activity increased with the addition of nickel hydroxide to the CG nanocomposite. However, more than 44 wt.% likely resulted in the agglomeration of the particles, and therefore, the size increase led to a decrease in the active sites. The ORR properties were further investigated through the performance of LSVs in an O_2-saturated 0.1 M KOH electrolyte, at a scan rate of 50 mV s^{-1} using a rotating disk electrode (RDE) method. RDE method is used to make a steady-state diffusion condition and minimize the contribution of mass transfer to reaction kinetics. Figure 6.7A depicts the ORR polarization curves of NCG that were normalized by the geometrical surface area of the electrodes at rotation speeds varied from 200 to 2200 rpm. The curves display the mixed kinetic-diffusion control region between 0.915 and 0.665 V and the diffusion-limiting current region between 0.615 and 0.365 V vs RHE. It is worthy to note that the current density of the NCG nanocomposite measured at 1600 rpm was much higher compared to some other Ni-based ORR catalysts such as $NiCo_2O_4$ [28], $NiCo_2O_4$/rGO [29], Ni_3S_2 [30], and NiO flakes wrapped in GO sheets [31].

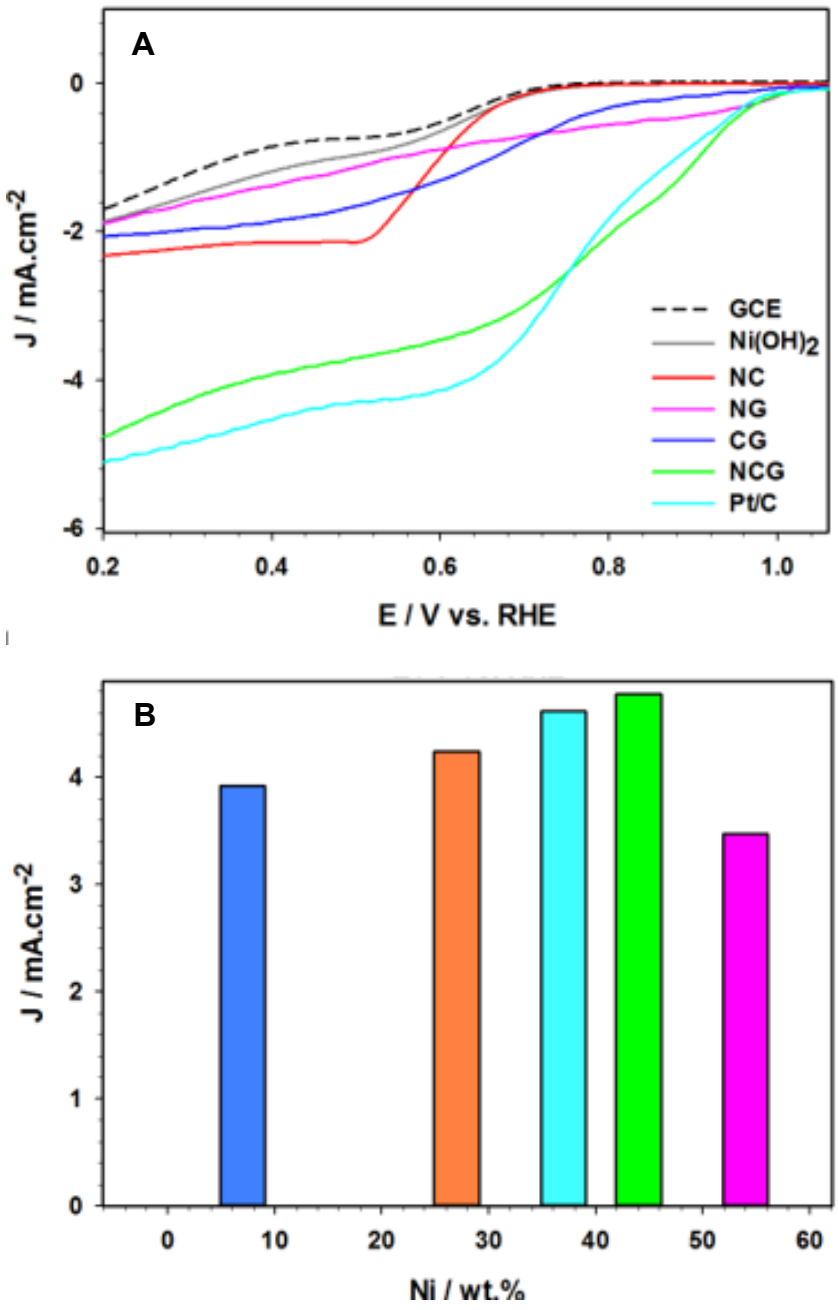

Figure 6.6 (A) Linear sweep voltammetry of different electrodes in O_2 saturated 0.1 M KOH at 1600 rpm at 50 mV s^{-1} scan rate, (B) Current response of different concentrations of Ni on Ni/C_3N_4/rGO electrodes in O_2 saturated 0.1 M KOH at 0.2 V and at the rotating speed of 1600 rpm and the scan rate of 50 mV s^{-1}.

Oxygen reduction reactions can occur via two main pathways; i.e. the less desired indirect or 2-e^- transfer pathway and direct or 4-e^- transfer pathway, which is the most desired one [32]. In order to find the pathway under which oxygen reduction is happening, Koutecky-Levich (K-L) plots can be used [33]. Figure 6.7B presents the Koutecky-Levich plots of NCG, and the number of electron transfer for ORR at different electrode potentials was estimated based on the slope as shown in Figure 6.7C. The average number of electron transfer was calculated to be 3.93, revealing that the direct four-electron transfer dominated in the oxygen reduction process at the NCG nanocomposite although under some potentials a small amount of HO_2^- along with OH^- might be generated. Recent studies of unsupported and graphene supported nickel hydroxide catalysts have shown that the catalysts may produce both OH^- and HO_2^-, while for the graphene supported ones, the four-electron pathway is dominant [34]. Graphene has also helped in increase the kinetic rate constant of the catalyst probably due to a reduction of the activation energy of O_2 adsorption [34]. The main pathway for the CG catalyst is four-electron as well, which is attributed to the densely stacked rGO sheets on porous C_3N_4 sites facilitating direct electrical contact within the composite and providing an efficient network for electron transport along with good conductivity and high charge transfer kinetics [35]. However, C_3N_4 alone did not improve the catalytic activity towards oxygen reduction reaction. The mass transfer corrected Tafel plot [35] of the NCG nanocomposite is presented in Figure 6.7D. The slope was calculated to be 0.075 V dec^{-1}, close to the value obtained for Pt/C electrodes (0.060 V dec^{-1}) at the low current density region, indicating that the rate-determining step might be the oxygen adsorption process under the Temkin adsorption condition [36].

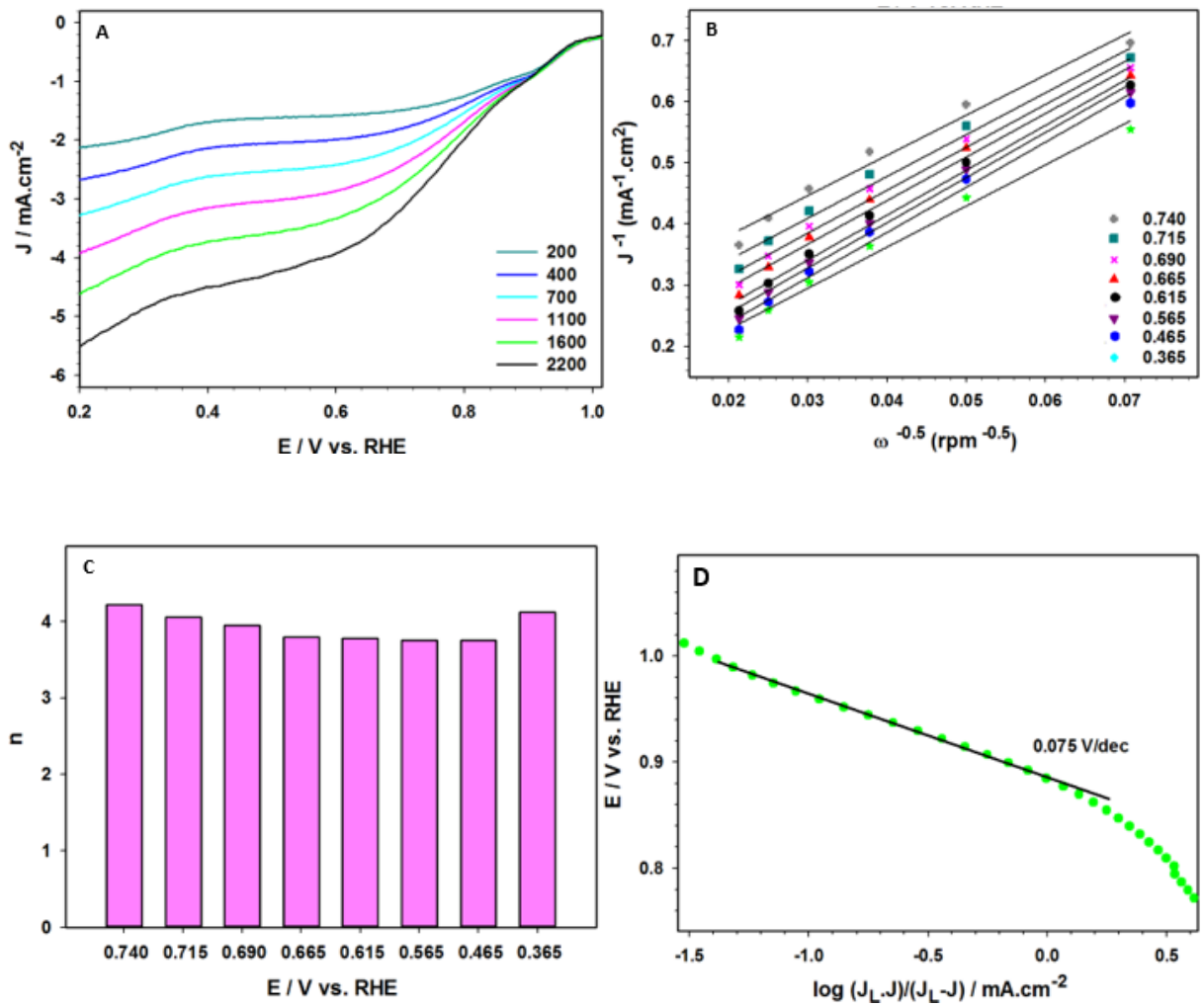

Figure 6.7 (A) Linear sweep voltammetry of the optimal $Ni/C_3N_4/rGO$ in O_2 saturated 0.1 M KOH at rotating speeds of 200, 400, 700, 1100, 1600, 2200 rpm at the scan rate of 50 mV s^{-1}, (B) Koutecky-Levich plots of NCG at 0.740, 0.715, 0.690, 0.665, 0.615, 0.565, 0.465 and 0.365 V, (C) Number of electrons being transferred at each potential for the NCG nanocomposite electrode calculated from the K-L plots presented in part (B), and (D) Mass transfer corrected Tafel plot of NCG for ORR at the rotation speed of 2200 rpm and the scan rate of 2 mV s^{-1}.

Methanol crossover can cause problems by permeating the membrane on the anode side and moving to the cathode side, where it could result in decline in the efficiency due to CO production as a side product of its chemical oxidation. Therefore, there is a need for cathode materials with

high tolerance towards methanol. Figure 6.8A shows chronoamperometric plots of the NCG and commercial Pt/C electrodes in an O_2-saturated 0.1 M KOH solution, prior to and following the addition of CH_3OH (3 M) at 0.615 V and a 1600 rpm rotation speed. The retained stable current response, except for a slight current increase following the addition of methanol, indicated a very good tolerance of the NCG nanocomposite electrode to the CH_3OH crossover effect, which is a challenge encountered in the methanol fuel cell where Pt is used as the cathode. In comparison, upon addition of 3 M methanol, for the Pt/C electrode, a sudden drop in current of the Pt/C electrode was observed, indicating the occurrence of the partial oxidation of methanol and dramatic decrease of the catalytic activity, which is one of the major drawbacks of the Pt/C catalyst used for ORR in the direct methanol fuel cell.

The durability of NCG with respect to commercial Pt/C, which is widely used as the benchmark electrocatalyst for oxygen reduction in acidic media, was further evaluated using the chronoamperometric technique carried out in an O_2-saturated 0.1 M KOH at 0.615 V and a rotation speed of 1600 rpm. As Figure 6.8B reveals, the current−time response for NCG demonstrated a very slow deterioration of the electrode activity, with a high current retention of 93.6% after 40,000 s; whereas, for the Pt/C electrode, a rapid current decrease (57.9%) was observed. The superior durability of the NCG may be attributed to the uniquely confined structure of nickel hydroxide nanoparticles (NPs) within the graphene sheets and carbon nitride particles, which can improve their interfacial contact while impeding the agglomeration and dissolution of NPs, as well as assisting with the transport of ions within the electrolyte [27].

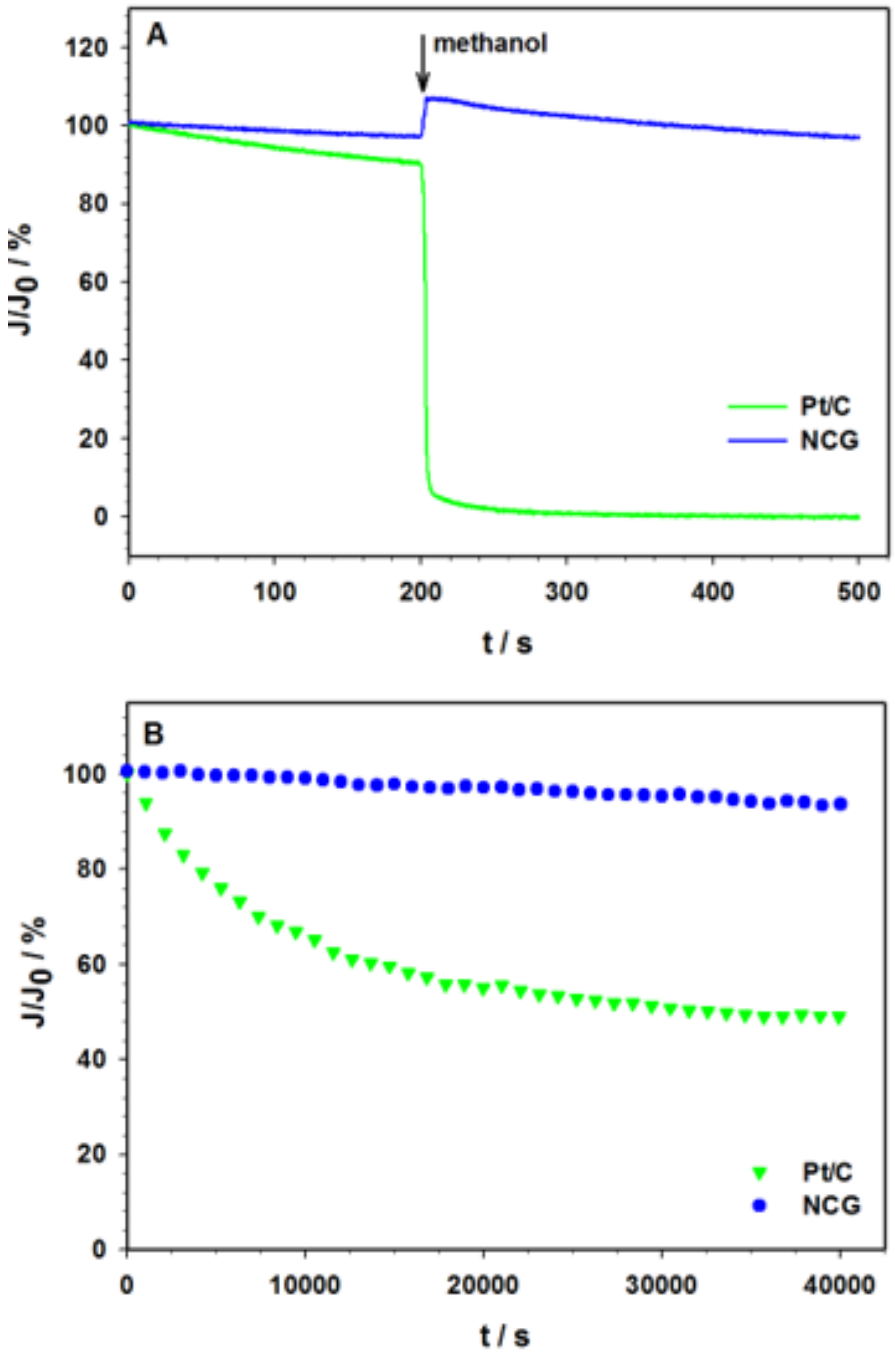

Figure 6.8 (A) Current-time response at Pt/C and NCG in an oxygen saturated 0.1 M KOH prior to and following the addition of 3 M methanol at 0.615 V at 1600 rpm, (B) Stability tests of the NCG and Pt/C electrodes in oxygen saturated 0.1 M KOH at 0.615 V at 1600 rpm.

6.4 Conclusions

In summary, we have successfully developed a novel NCG nanocomposite via a cost-effective and facile one-step electrochemical process. Due to the presence of carbon nitride and reduced graphene oxide sheets within the structure and high surface area, the novel NCG nanocomposite demonstrated excellent electrocatalytic activity for the ORR in an alkaline electrolyte with a high mass activity of 12.83 $A\ g_{Ni}^{-1}$, along with an improved current density, higher electron transfer number, enhanced resistance to methanol poisoning, and better durability, which makes the NCG a promising non-precious metal cathode catalyst for fuel cell applications. The novel approach described in this study would open the door to develop other metal or metal oxide/graphene-based nanocomposites for promising energy conversion and environmental.

References

[1] F. Pan, J. Jin, X. Fu, Q. Liu, J. Zhang, Advanced oxygen reduction electrocatalyst based on nitrogen-doped graphene derived from edible sugar and urea, *ACS Appl. Mater. Interfaces*, 2013, **5**, 11108-11114.

[2] L. Feng, L. Yang, Z. Huang, J. Luo, M. Li, D. Wang, Y. Chen, *Sci. Rep.*, 2013, **3**, 3306.

[3] I. Mahesh, A. Sarkar, Electrochemical study of oxygen reduction on carbon supported core-shell platinum-gold electrocatalyst with tuneable surface composition of gold, *ChemElectroChem*, 2016, **3**, 836-845.

[4] A. Chen, P. Holt-Hindle, Platinum-based nanostructured materials: synthesis, properties, and applications, *Chem. Rev.*, 2010, **110**, 3767-3804.

[5] A. Chen, C. Ostrom, Palladium-based nanomaterials: synthesis and electrochemical applications, *Chem. Rev.*, 2015, **115**, 11999-12044.

[6] L. Tao, Q. Wang, S. Dou, Z. Ma, J. Huo, S. Wang, L. Dai, Edge-rich and dopant-free graphene as a highly efficient metal-free electrocatalyst for the oxygen reduction reaction, *Chem. Commun.*, 2016, **52**, 2764-2767.

[7] W. Alammari, M. Govindhan, A. Chen, Modification of TiO_2 nanotubes with PtRu/graphene nanocomposites for enhanced oxygen reduction reaction *ChemElectroChem*, 2015, **2**, 2041-2047.

[8] M. Bron, J. Radnik, M. Fieber-Erdmann, P. Bogdanoff, S. Fiechter, EXAFS, XPS and electrochemical studies on oxygen reduction catalysts obtained by heat treatment of iron phenanthroline complexes supported on high surface area carbon black, *J. Electroanal. Chem.*, 2002, **535**, 113-119.

[9] S. M. Lyth, Y. Nabae, S. Moriya, S. Kuroki, M. Kakimoto, J. Ozaki, S. Miyata, Carbon nitride as a nonprecious catalyst for electrochemical oxygen reduction, *J. Phys. Chem. C*, 2009,**113**, 20148-20151.

[10] X. Liu, L. Li, W. Zhou, Y. Zhou, W. Niu, S. Chen, High-performance electrocatalysts for oxygen reduction based on nitrogen-doped porous carbon from hydrothermal treatment of glucose and dicyandiamide, *ChemElectroChem*, 2015, **2**, 803-810.

[11] R. A. Sidik, A. B. Anderson, N. P. Subramanian, S. P. Kumaraguru, B. N. Popov, O_2 reduction on graphite and nitrogen-doped graphite: experiment and theory, *J. Phys. Chem. B*, 2006, **110**, 1787-1793.

[12] Y. Li, Y. Li, E. Zhu, T. McLouth, C. Y. Chiu, X. Huang, Y. Huang, Stabilization of high-performance oxygen reduction reaction Pt electrocatalyst supported on reduced graphene oxide/carbon black composite, *J. Am. Chem. Soc.*, 2012, **134**, 12326-12329.

[13] B. Seger, P. V. Kamat, Electrocatalytically active graphene-platinum nanocomposites. Role of 2-D carbon support in PEM fuel cells, *J. Phys. Chem. C*, 2009, **113**, 7990-7995.

[14] C. Wang, L. Ma, L. Liao, S. Bai, R. Long, M. Zuo, Y. Xiong, A unique platinum-graphene hybrid structure for high activity and durability in oxygen reduction reaction, *Sci. Rep.*, 2013, 3, 2580.

[15] J. Tian, Q. Liu, C. Ge, Z. Xing, A. M. Asiri, A. O. Al-Youbi, X. Sun, Ultrathin graphitic carbon nitride nanosheets: a low-cost, green, and highly efficient electrocatalyst toward the reduction of hydrogen peroxide and its glucose biosensing application, *Nanoscale*, 2013, **5**, 8921-8924.

[16] J. Liang, Y. Zheng, J. Chen, J. Liu, D. Hulicova-Jurcakova, M. Jaroniec, S. Z. Qiao, Facile oxygen reduction on a three-dimensionally ordered macroporous graphitic C_3N_4/carbon composite electrocatalyst, *Angew. Chem. Int. Ed.*, 2012, **51**, 3892-3896.

[17] G. Wu, S. S. Thind, J. Wen, K. Yan, A. Chen, A novel nanoporous α-C_3N_4 photocatalyst with superior high visible light activity, *Appl. Catal. B*, 2013, **142–143**, 590-597.

[18] Y. Liang, H. Wang, J. Zhou, Y. Li, J. Wang, T. Regier, H. Dai, Covalent hybrid of spinel manganese–cobalt oxide and graphene as advanced oxygen reduction electrocatalysts, *J. Am. Chem. Soc.*, 2012, **134**, 3517-3523.

[19] I. J. Godwin, M. E. G. Lyons, Enhanced oxygen evolution at hydrous nickel oxide electrodes via electrochemical ageing in alkaline solution, *Electrochem. Commun.*, 2013, **32**, 39-42.

[20] M. Saeed, M. Ilyas, Oxidative removal of phenol from water catalyzed by nickel hydroxide, *Appl. Catal. B*, 2013, **129**, 247-254.

[21] S. K. Konda, A. Chen, One-step synthesis of Pd and reduced graphene oxide nanocomposites for enhanced hydrogen sorption and storage, *Electrochem. Commun.*, 2015, **60**, 148-152.

[22] S. K. Konda, M. Amiri, A. Chen, Photoassisted deposition of palladium nanoparticles on carbon nitride for efficient oxygen reduction, *J. Phys. Chem. C*, 2016, **27**, 14467-14473.

[23] H. Jiang, Y. Guo, T. Wang, P. L. Zhu, S. Yu, Y. Yu, X. Z. Fu, R. Sun, C. P. Wong, Electrochemical fabrication of $Ni(OH)_2$/Ni 3D porous composite films as integrated capacitive electrodes, *RSC Adv.*, 2015, **5**, 12931-12936.

[24] Y. Zhou, G. Zhang, Z. Gong, X. Shang, F. Yang, Potentiodynamic uniform anchoring of platinum nanoparticles on N-doped graphene with improved mass activity for the electrooxidation of ammonia, *ChemElectroChem*, 2016, **3**, 605-614.

[25] Y. Q. Zhang, D. K. Ma, Y. Zhuang, X. Zhang, W. Chen, L. L. Hong, Q. X. Yan, K. Yu, S. M. Huang, One-pot synthesis of N-doped carbon dots with tunable luminescence properties, *J. Mater. Chem.*, 2012, **22**, 16714-16718.

[26] M. Kim, S. Hwang, J. S. Yu, Novel ordered nanoporous graphitic C_3N_4 as a support for Pt–Ru anode catalyst in direct methanol fuel cell, *J. Mater. Chem.*, 2007, **17**, 1656-1659.

[27] Z. S. Wu, S. Yang, Y. Sun, K. Parvez, X. Feng, K. Mullen, 3D nitrogen-doped graphene aerogel-supported Fe_3O_4 nanoparticles as efficient electrocatalysts for the oxygen reduction reaction, *J. Am. Chem. Soc.*, 2012, **134**, 9082-9085.

[28] Z. Jiang, Z. Jiang, Reduction of the oxygen reduction reaction overpotential of nitrogen-doped graphene by designing it to a microspherical hollow shape, *J. Mater. Chem. A*, 2014, **2**, 14071-14081.

[29] Y. Xiao, C. Hu, L. Qu, C. Hu, M. Cao, Three-dimensional macroporous $NiCo_2O_4$ sheets as a non-noble catalyst for efficient oxygen reduction reactions, *Chem. - Eur. J.*, 2013, **19**, 14271-14278.

[30] G. Zhang, B. Y. Xia, X. Wang, Strongly coupled $NiCo_2O_4$-rGO hybrid nanosheets as a methanol-tolerant electrocatalyst for the oxygen reduction reaction, *Adv. Mater.*, 2014, **26**, 2408-2412.

[31] J. M. Falkowski, N. M. Concannon, B. Yan, Y. Surendranath, Heazlewoodite, Ni_3S_2: A potent catalyst for oxygen reduction to water under benign conditions, *J. Am. Chem. Soc.*, 2015, **137**, 7978-7981.

[32] C. Jin, F. Lu, X. Cao, Z. Yang, R. Yang, Facile synthesis and excellent electrochemical properties of $NiCo_2O_4$ spinel nanowire arrays as a bifunctional catalyst for the oxygen reduction and evolution reaction, *J. Mater. Chem. A*, 2013, **1**, 12170−12177.

[33] M. B. Zakaria, V. Malgras, T. Takei, C. Li, Y. Yamauchi, Layer-by-layer motif hybridization: nanoporous nickel oxide flakes wrapped into graphene oxide sheets toward enhanced oxygen reduction reaction, *Chem. Commun.*, 2015, **51**, 16409-16412.

[34] E. Farjami, L. J. Deiner, Kinetic Study of the Oxygen Reduction Reaction on α-$Ni(OH)_2$ and α-$Ni(OH)_2$ Supported on Graphene Oxide, *J. Electrochem. Soc.*, 2015, **162**, H571-H578.

[35] J. Tian, R. Ning, Q. Liu, A. M. Asiri, A. O. Al-Youbi, X. Sun, Three-dimensional porous supramolecular architecture from ultrathin g-C_3N_4 nanosheets and reduced graphene oxide: solution self-assembly construction and application as a highly efficient metal-free electrocatalyst for oxygen reduction reaction, *ACS Appl. Mater. Inter.*, 2014, **6**, 1011-1017.

[36] A. Ezeta-Mejía, O. Solorza-Feria, H. J. Dorantes-Rosales, J. H. López, E. M. Arce-Estrad, Electrocatalytic properties of bimetallic surfaces for the oxygen reduction reaction, *Int. J. Electrochem. Sci.*, 2012, **7**, 8940-8957.

[37] A. Muthukrishnan, Y. Nabae, C. W. Chang, T. Okajima, T. Ohsaka, A high-performance Fe and nitrogen doped catalyst derived from diazoniapentaphene salt and phenolic resin mixture for oxygen reduction reaction, *Catal. Sci. Tech.,* 2015, **5**, 1764-1774.

Chapter 7: Superb Pseudocapacitance Based on Three-Dimensional Porous Nickel Oxide Modified with Iridium Oxide

7.1 Introduction

With the increasing demand for more efficient, less polluting, and environmentally compatible energy systems, batteries and capacitors have garnered significant attention [1]. An electrochemical capacitor involves immersion of electrode materials within an electrolyte, where energy is stored via an electrochemical process [2]. Based on charge storage mechanisms, electrochemical capacitors are divided into two subcategories [3]: (i) supercapacitors, which operate on the basis of a non-Faradaic process (charge/discharge the double-layer) at the electrode/electrolyte interface; and (ii) pseudocapacitors, where the Faradaic reactions of electroactive materials are involved at the interface. These devices have the potential to provide high power densities and energy densities [4] as well as rapid charge/discharge rates [5]. However, the aforementioned characteristics are strongly contingent on the selected electrode material. While endeavoring to improve materials with high capacitances and remarkable electrical conductivities, the aim is to develop an eco-compatible electrode [4]. In order to enhance electrochemical energy storage capacities, two primary approaches have been extensively explored. One involves expanding the specific surface area of the electrode to increase the number of adsorbed ions from the electrolyte. The other entails the utilization of transition metal oxides with different oxidation states, robust redox reversibility, and chemical stability to engage pseudocapacitance [6, 7].

Although supercapacitors have garnered significant attention due to their high power density, they would be even more desirable if they could provide improved energy densities. On the other

hand, pseudocapacitor materials, such as metal oxides, hydroxides, or conductive polymers may offer even more specific capacitance along with enhanced energy densities [8, 9]. Among these materials, transition metal oxides and hydroxides, including $Ni(OH)_2$ [10], NiO [11-13], $Co(OH)_2$ [14], RuO_2 [15], IrO_2 [6], and Fe_2O_3 [16] have demonstrated attractive properties for electrochemical capacitor applications.

Various techniques, such as the hydrothermal method, chemical reduction, chemical vapor deposition, chemical bath deposition, and electrodeposition have been employed to fabricate electrode materials with high surface areas [17]. Electrochemical deposition comprises a facile approach with the advantages of simple instrumentation, easy auto-control and scale-up; hence, it has gained much attention in recent years. Hydrogen bubbles simultaneously formed on electrode surfaces during the electrochemical deposition process may be utilized as templates for the growth of 3D porous structures [18]. Generally speaking, a large cathodic current density is applied to ensure that both metal deposition and hydrogen evolution occur at a rapid rate, thereby, resulting in a very porous structure. The generated 3D porous structures may possess fine grains and provide an expansive surface area, thus facilitating access for reactants to active sites on the surface to further enhance the reactive performance of the electrode [19-21]. High surface area makes the formed 3D porous structures excellent candidates for various environmental and energy applications, such as electrochemical supercapacitors and pseudocapacitors.

Nickel and nickel-based electrodes are among numerous materials that have attracted considerable attention as electrochemical capacitors, as well as suitable substrates for this purpose [22, 23]. Nickel is a cost effective and naturally abundant material, whereas nickel oxide has been widely investigated due to its intrinsically benign nature, high redox activity, and very high capacitance [24, 7]. However, it remains a challenge to achieve the theoretical specific capacitance

of NiO due to its low electrical conductivity [5]. In order to improve this situation, the modification of NiO with conductive polymers or other oxides with high conductivity has been explored. Improvements in the pseudocapacitive behavior was observed when NiO was combined with MnO_2 [22], MnO_2/CeO_2 [25], and mixed oxides, such as $NiCo_2O_4$ [26, 27].

Iridium belongs to the transition metal category, and iridium oxide possesses a rutile structure with good conductivity, similar to a metal [28]. Iridium oxide has been widely employed as an electrode material in electrocatalysis, electrochromic displays, and sensors [29, 30]. It also exhibits high chemical stability, several oxidation states, and high redox reversibility, making IrO_2 an appropriate candidate for electrochemical capacitors [6]. Further, when coupled with other oxides, such as tungsten oxide, tantalum oxide [28], or ruthenium oxide [31], it has exhibited improved electrochemical capacitance.

For the present study, a 3D porous nickel was grown directly onto a Ni plate using a feasible electrodeposition technique, which was assisted by hydrogen bubble templates. The effects of applied current densities and durations on the growth of the 3D porous nickel were investigated in order to identify the optimal conditions. The optimized 3D porous Ni electrodes were subsequently modified with iridium oxide. Compared to 3D porous NiO, the addition of iridium oxide to the 3D porous nickel structure showed a significant enhancement in the specific capacitance.

7.2 Experimental

7.2.1. Chemicals and materials

Nickel chloride ($NiCl_2.6H_2O$, ≥ 98.0%), ammonium chloride (NH_4Cl, ≥ 99.5%), and potassium hydroxide of analytical grade were purchased from Sigma-Aldrich. Iridium chloride ($IrCl_3 \cdot 3H_2O$)

was obtained from Pressure Chemical Corp. These chemicals were used without any further purification. Prior to electrodeposition, a nickel foil purchased from Alfa-Aesar (purity: 99.5%; thickness: 0.5 mm) was cut into small pieces (1.0 cm x 1.0 cm), cleaned via sonication in acetone, and rinsed using double-distilled water.

7.2.2 Preparation and modification of the 3D porous nickel

The electrodeposition of the 3D porous nickel electrodes was carried out in a 2.0 M NH_4Cl + 0.1 M $NiCl_2$ solution under two different current densities of 1.5 and 3.0 A cm^{-2} over different time intervals of 75, 100, and 150 s using Arbin Instruments (MSTAT, USA) potentiostat/galvanostat. The 3D porous Ni electrode prepared at 3.0 A cm^{-2} for 150 s was selected to be modified with various loadings of a 0.1 M iridium chloride precursor, where the loaded iridium amounts were 3.0, 7.0, 10.0, and 15.0 wt.% of the 3D porous Ni that was electrodeposited on the Ni plate. For clarification, the prepared samples were denoted as NiIr(3%)Ox, NiIr(7%)Ox, NiIr(10%)Ox, and NiIr(15%)Ox, respectively. Following air drying, the cast electrodes, including a 3D porous nickel electrode (as the control electrode), were annealed at 450 ^oC for 3 h in an air furnace.

7.2.3 Surface characterization and electrochemical studies

The surface morphologies, particle sizes, and compositions of the 3D porous nickel electrodes prior to and following the modification of IrO_2, were characterized using field-emission scanning electron microscopy (FE-SEM, Hitachi SU70) coupled with energy dispersive X-ray spectroscopy (EDS). X-ray photoelectron spectroscopy (XPS) (Thermo Scientific K-alpha) was employed to

investigate the oxidation states of each element using a monochromatic Al Kα X-ray source with a spot size of 400 μm, where the takeoff angle from the horizontal surface was 90 degrees. Charge compensation was measured and the spectra correction was accomplished using the position of the C-C peak at 284.6 eV. The deconvolution of the spectra was performed using XPSpeak software.

Electrochemical studies were performed in a three-electrode cell system, using a Voltalab 40 potentiostat (PGZ 402) for cyclic voltammetry (CV); and a Solartron SI 1287, which was equipped with frequency response analyzer (1252A), was employed for the electrochemical impedance spectroscopy (EIS) and galvanostatic charge/discharge analysis. The prepared 3D porous Ni based electrodes were used as the working electrode, the coiled Pt wire as the counter electrode, and an Ag/AgCl electrode as the reference electrode. The platinum wire was flamed and quenched prior to use.

7.3 Results and discussion

7.3.1. Surface morphology and electrochemical studies of the 3D porous Ni

Three-dimensional porous nickel samples were fabricated using hydrogen bubble template electrodeposition, which was performed in a nickel-containing ammonium chloride solution, where different current densities over various deposition times were employed. The FE-SEM images of the 3D nickel electrode prepared at an applied current density of 3.0 A cm^{-2} for 150 s are presented in Figure 7.1. As seen in the low-magnification image (Figure 7.1A), a 3D interconnected porous structure was uniformly formed on the Ni plate with an average pore diameter of ~5.5 μm, due to the generation of hydrogen bubbles. The high-magnification SEM image (Figure 7.1B) depicts the typical morphology of the walls that surrounded the generated

pores, which exhibited a flower-like porous structure that was formed by small particulates with an average size of ~500 nm. It was anticipated that the formation of the interconnected 3D porous structure would greatly increase the surface area, which was desirable for the capacitance application.

Cyclic voltammetry was employed to investigate the effects of the applied time and current density of the electrodeposition process on the electrochemical behaviors, as well as the electrochemically active surface area (EASA) of the fabricated 3D porous Ni electrodes. Figure 7.2A presents the CV curves of the 3D porous Ni electrodes, which were prepared under an applied current density of 1.5 A cm^{-2} for 75, 100, and 150 s recorded in a 0.1 M KOH solution at the scan rate of 20 mV s^{-1}. The CV curve of a smooth Ni substrate is also included for the comparative purpose. As the CV of the smooth Ni electrode was so small, it was enlarged and presented as the inset of Figure 7.2A. Well defined oxidation and reduction peaks appeared in all the CV curves. It is known that in alkaline media, Ni might be easily oxidized to form $Ni(OH)_2$, which can be further oxidized to NiOOH at the electrode potential of ~ 0.85 V vs. Ag/AgCl. The cathodic peak (*ca*. 0.33 V vs. Ag/AgCl) may be attributed to the reduction of NiOOH, which was generated during the anodic oxidation, to form $Ni(OH)_2$ [32]. It was evident that the hydrogen bubble-assisted electrodeposition dramatically enhanced the actual surface area. By increasing the electrodeposition time from 75 to 150 s, the oxidation and reduction peaks were gradually increased. This might be attributed to the effect of having additional nickel deposited onto the electrode, as well as formation of additional pores on the surface, thereby leading to higher roughness values and thus a higher population of active sites.

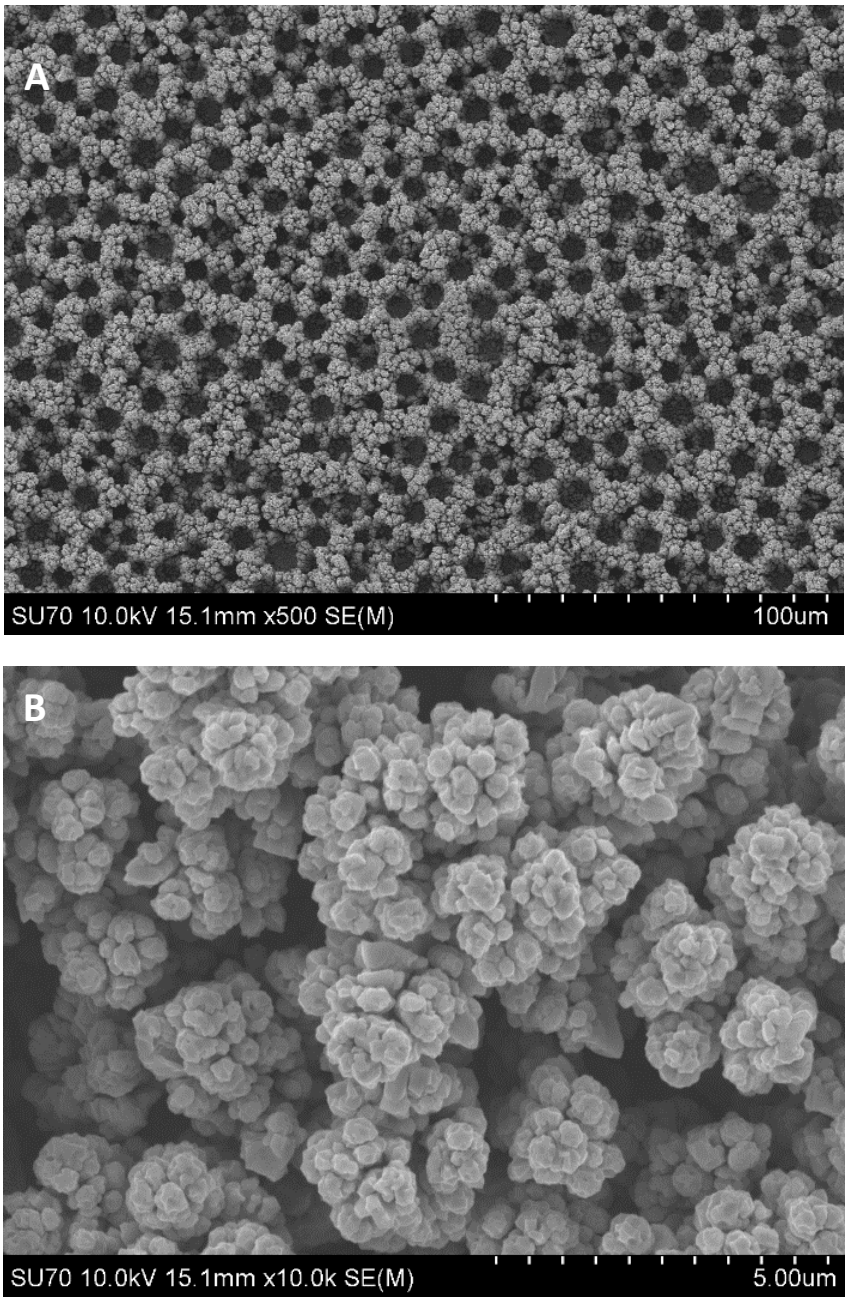

Figure 7.1 (A) & (B) SEM images of the 3D porous Ni grown on a Ni substrate via hydrogen bubble template electrochemical deposition at 3.0 A cm^{-2} and 150 s.

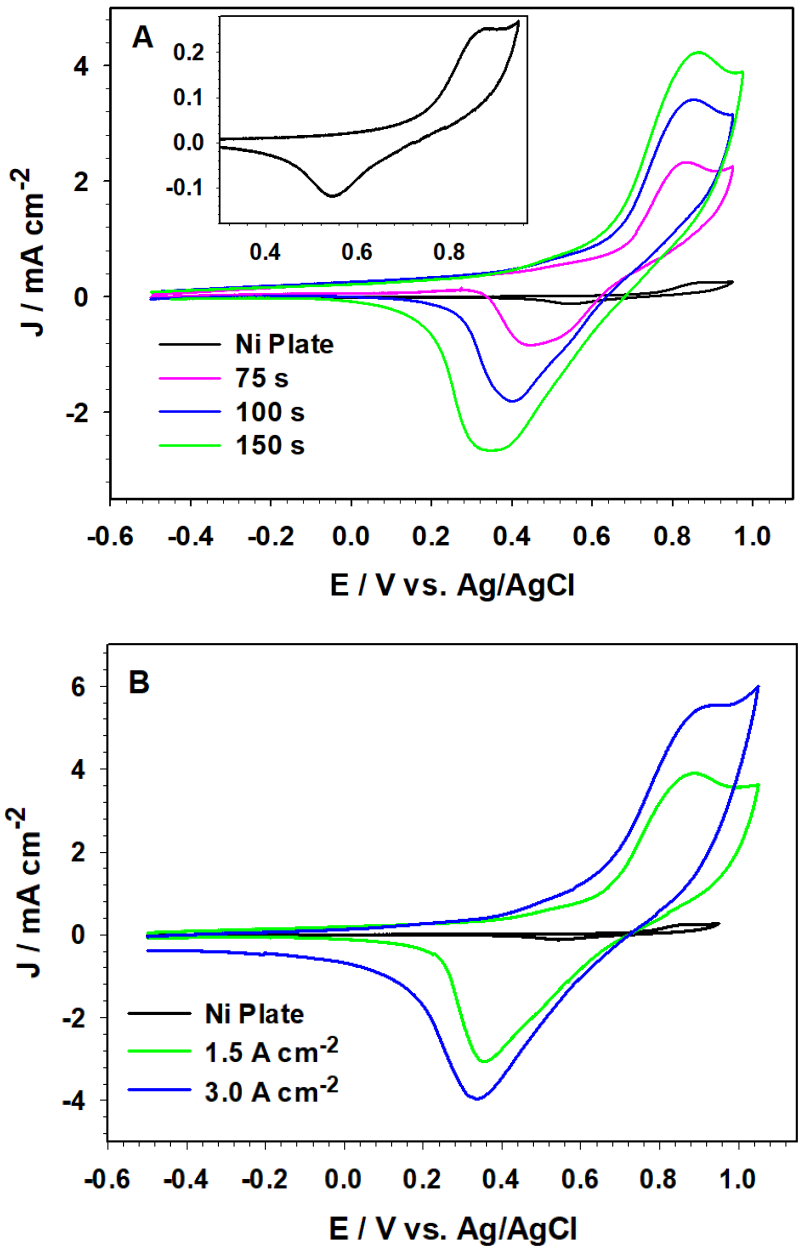

Figure 7.2 Cyclic voltammograms of the 3D porous Ni electrodeposited: (A) at the applied current density of 1.5 A cm^{-2} for different durations (inset is the CV curve of a smooth Ni plate for comparison purposes); and (B) at different applied current densities for 150 s. Electrolyte: 0.1 M KOH solution; scan rate: 20 mV s^{-1}.

The EASA of the fabricated 3D porous Ni electrodes was estimated based on the integration of the anodic peak of the CV curves, with the results listed in Table 7.1. The EASA of the 3D porous

Ni electrode prepared under an applied current density of 1.5 A cm^{-2} for 75 s was 16.29 times larger than that of the smooth Ni electrode. The EASA was increased with the prolongation of the electrodeposition time, from 75 to 150 s to attain 26.66 cm^2, which was a ~1.64 fold increase. The effect of the applied current density was also investigated, where the electrodeposition time was kept at 150 s. As displayed in Figure 7.2B, the oxidation and reduction peaks were increased with a higher applied current density, from 1.5 to 3.0 A cm^{-2}. As listed in Table 7.1, the EASA of the 3D porous Ni electrode prepared at the applied current density of 3.0 A cm^{-2} was calculated to be 34.50 cm^2, which was a ~1.29 fold increase, which revealed that the changes incurred upon increasing the current were not as significant as extending the deposition time. This might be explained by the consumption of extra current through the gas formation/evolution, rather than the electrodeposition of nickel by increasing the applied current density.

Table 7.1 EASA for 3D porous nickel structures grown under different applied current densities and times estimated using the CV curves presented in Figure 7.2.

Conditions		**EASA / cm^2**
Applied current density / A cm^{-2}	**time / s**	
1.5	75	16.29
1.5	100	21.73
1.5	150	26.66
3.0	150	34.50

7.3.2 Surface morphology and elemental analysis of the modified 3D porous electrodes

Figure 7.3 presents low magnification SEM images of the 3D porous nickel following the heat treatment process at 450 ºC for 3 h without (A) and with the iridium chloride precursor (B) as well as a high magnification SEM image of NiIr(10%)Ox (D) and a corresponding, relatively high magnification SEM image of NiO, which is displayed in Figure 7.3C. Compared to the 3D porous Ni (Figure 7.1A), the interconnected porous network structure disappeared due to the formation and growth of the NiO particles where instead, several large pores with diameters between 2 and 17 μm were observed (Figure 7.3A). The average dimension of the formed NiO particles was ~850 nm (Figure 7.3C), which was larger than that of the Ni particles (Figure 7.1B). In contrast, as shown in Figure 7.3B, the electrodeposited 3D porous Ni network structure served as a template to accommodate the cast iridium chloride precursor solution, and to anchor the formed iridium oxide during the subsequent thermal treatment. The formed iridium oxide particles were infused within and covered some of the pores and gaps/cracks of the 3D porous Ni surface. The average pore diameter and depth of the formed NiIr(10%)Ox were ~10 μm (Figure 7.3B) and ~5 μm (Figure 7.3D), respectively. It was anticipated that conductive iridium oxide with an appropriate hierarchical 3D porous Ni current collector backbone would exhibit excellent electrochemical behavior. This would be enabled by a high actual surface area, as well as facile electron exchange and ion diffusion between the electrolyte and electrode due to the extensive porous structure of the nickel substrate.

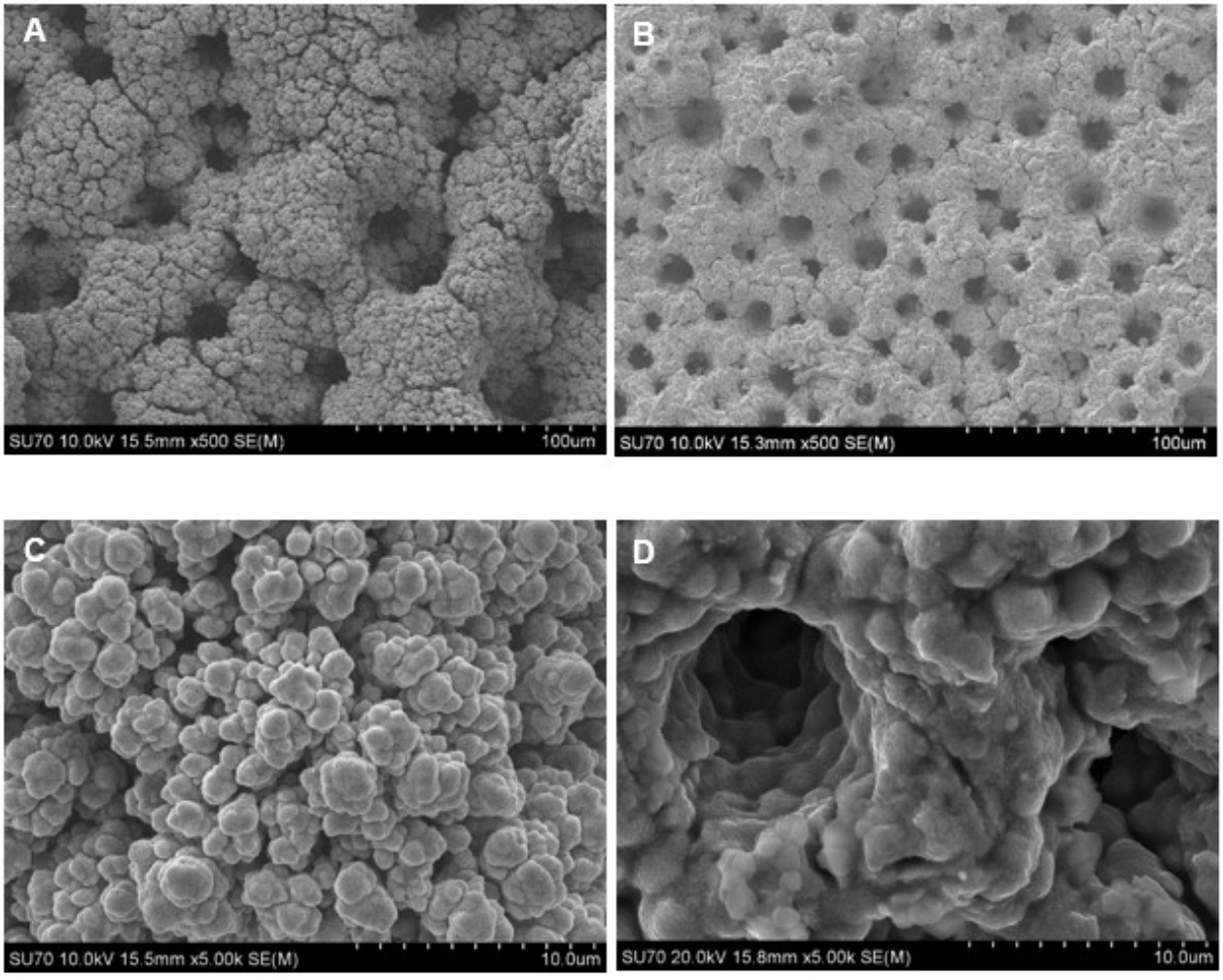

Figure 7.3 SEM images of the 3D porous (A) and (C) NiO, (B) and (D) NiIr(10%)Ox electrodes at low and high magnifications, respectively, and (E) the EDS spectra of the formed 3D porous Ni, NiO and NiIr(10%)Ox.

Figure 7.3E presents the EDS spectra of the fabricated 3D porous Ni, NiO, and NiIr(10%)Ox electrodes. A strong oxygen peak appeared following the thermal treatment process, showing the conversion of the 3D porous Ni to NiO. In addition, the peak intensity of Ni was decreased after the modification with iridium oxide; and strong nickel and iridium peaks were observed for the NiIr(10%)Ox sample. The ratio of the O:Ni peak intensity was increased due to the formation of the iridium oxide in addition to nickel oxide in the NiIr(10%)Ox sample.

XPS was employed to study the oxidation states of Ni and Ir in the fabricated 3D porous NiIr(10%)Ox electrode. The high-resolution spectrum of the primary Ni $2p_{3/2}$ and $2p_{1/2}$ peaks is presented in Figure 7.4A, revealing that ~97% of the nickel, located at binding energies of 853.9, 855.7, and 861.2 eV could be assigned to the Ni(II) oxidation state, which was in good agreement with the values reported in the literature for NiO [33]. The intrinsic characteristic spin-energy separation of 17.4 eV further confirmed the formation of NiO [34].

Figure 7.4B displays the high resolution Ir 4f spectrum of the NiIr(10%)Ox electrode surface. The $4f_{7/2}$ and $4f_{5/2}$ peaks appeared at 62.0 and 65.0 eV, respectively, which might be attributed to the Ir(IV) oxidation state, in good agreement with reported values on an IrO_2 single crystal [35]. There are two additional peaks that appeared at 63.3 and 66.04 eV, which might be due to physisorbed hydroxyl groups [36].

Figure 7.4C displays the O 1s spectrum of the fabricated electrode, which could be deconvoluted into two intense peaks. The strong peak at 529.5 eV may be attributed to the oxygen chemical bonding in NiO, while the intense peak at 531.2 eV was due to the oxygen chemical bonding in IrO_2 [35, 37], which further confirmed the formation of the mixed NiO and IrO_2 in the 3D porous NiIr(10%)Ox electrode.

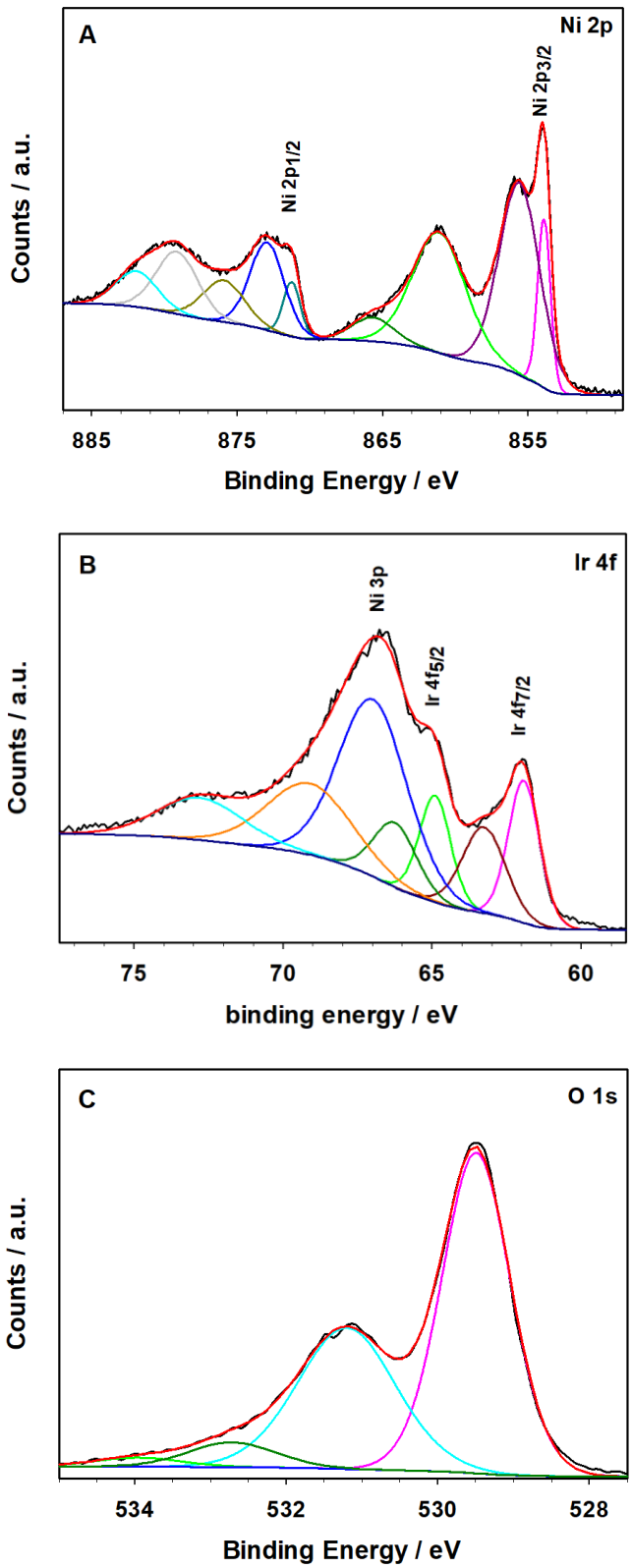

Figure 7.4 High resolution XPS spectra of (A) nickel, (B) iridium, and (C) oxygen derived from the 3D porous NiIr(10%)Ox electrode.

7.3.3 Electrochemical studies of the modified electrodes

Figure 7.5A presents the CV curves of the fabricated 3D porous NiO and NiIr(10%)Ox electrodes recorded in a 1.0 M KOH electrolyte at a scan rate of 50 mV s^{-1} in the potential range of 0.0 - 0.8 V vs. Ag/AgCl. The CVs showed a typical pseudocapacitance faradaic redox behavior, which was very different from the electric double-layer capacitance behavior (rectangular shape of CV curve) that is typically associated with supercapacitors. Also, the potential differences between the cathodic and anodic peaks were far larger than the theoretical value of 0.059 V for reversible single-electron involved redox reactions [38]. In the case of the 3D porous NiO electrode, the redox peaks might be attributed to the conversion between NiO and NiOOH, with the anodic peak appearing at ~0.51 V, and the cathodic peak located at 0.36 V vs. Ag/AgCl [23]. For the 3D porous NiIr(10%)Ox electrode, the anodic and cathodic peaks dramatically shifted to higher and lower potentials, respectively, in comparison to the CV curve of the 3D porous NiO electrode. These peaks could be ascribed to Ir(IV)/Ir(V) redox couples, as well as Ir(IV)/Ir(VI) [28, 39]. The symmetric behavior of anodic and cathodic peaks indicated excellent reversibility of the fabricated electrode as a pseudocapacitor. The iridium containing electrode delivered a far superior current response in contrast to the 3D porous NiO, which demonstrated the significance of the existence of IrO_2 on the 3D porous nickel current collector substrate.

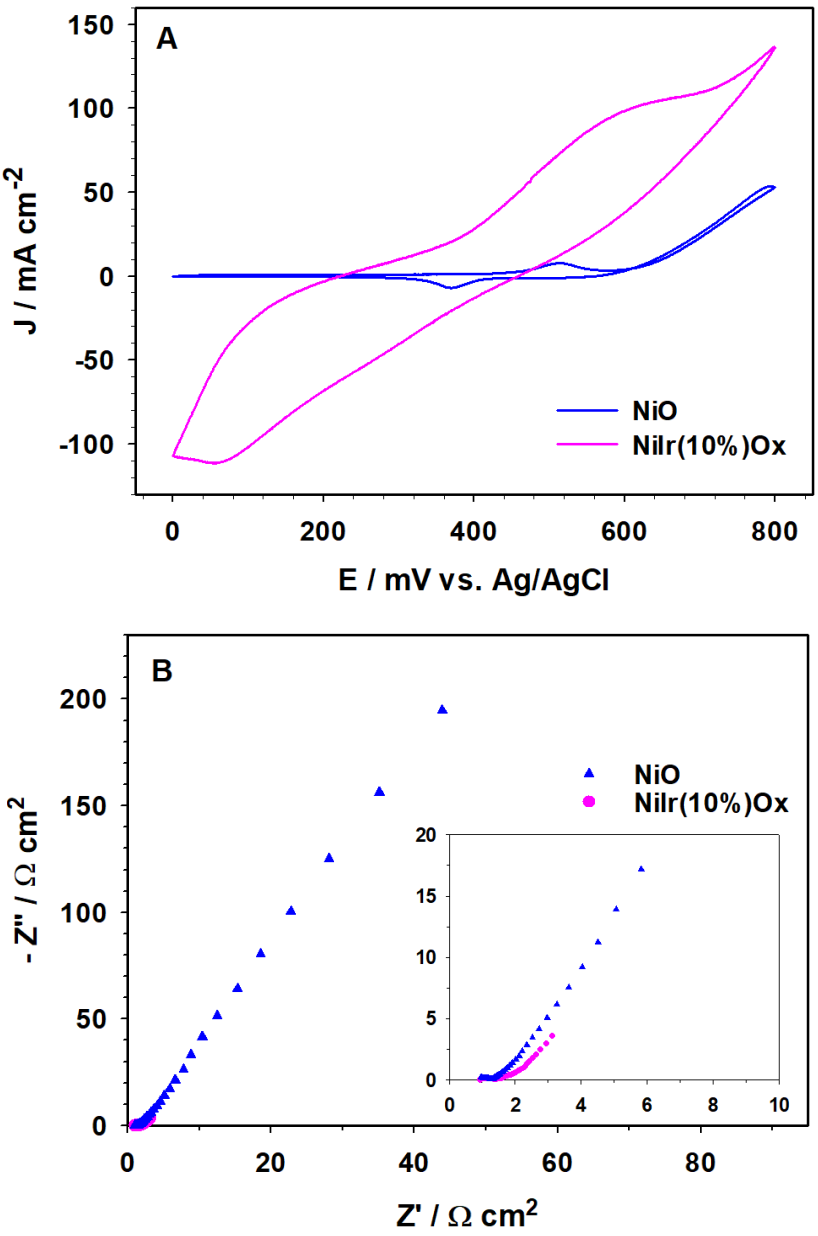

Figure 7.5 (A) Cyclic voltammograms of 3D porous NiO and NiIr(10%)Ox electrodes recorded in 1.0 M KOH at the scan rate of 50 mV s^{-1}, and (B) their electrochemical impedance spectra measured in 1.0 M KOH.

Electrochemical impedance spectroscopy was employed to investigate the frequency response of the 3D porous NiIr(10%)Ox electrode. Figure 7.5B compares the Nyquist plots of the 3D porous NiO and NiIr(10%)Ox electrodes recorded in a 1.0 M KOH solution at 0.37 V vs. Ag/AgCl where

the frequency was varied from 100 kHz to 20 mHz. Both the 3D porous NiO and NiIr(10%)Ox electrodes exhibited a small solution resistance. The 3D porous NiIr(10%)Ox composite demonstrated an enhancement in ionic transport in contrast to the 3D porous NiO electrode, as evidenced by the insignificant diameter of the semicircle, or high frequency region resistor/capacitor (RC) loop (indicating a lower charge transfer resistance and capacitance), as well as the smaller Warburg region (lower frequency), which is generally caused by mass transfer resistance [10]. The charge-transfer resistance of the 3D porous NiIr(10%)Ox electrode was estimated to be 0.21 Ω cm^2, which is an indication of a high charge-transfer rate at the electrode/electrolyte interface.

Figure 7.6A compares the charge/discharge behaviors of the 3D porous nickel samples modified with various concentrations of the iridium chloride precursor at a constant applied current density of 5.0 mA cm^{-2}. In agreement with the CVs shown in Figure 7.5A, the charge/discharge curves did not display the triangular behavior (which is typically observed for an electrical double layer capacitor). This performance was related to the redox reaction that occurred throughout the charge/discharge process. The IR drop, which is the potential drop right in the beginning of the discharge process, for the 3D porous nickel based electrodes modified with different quantities of iridium oxide was measured. As seen in Figure 7.6A, the 3D porous NiIr(10%)Ox electrode had the lowest IR drop of 0.021 V, while the NiIr(3%)Ox electrode possessed the highest IR drop (0.068 V) among all of the NiIrOx electrodes prepared in this study. This revealed that the NiIr(10%)Ox electrode had a fairly low internal resistance due to good interfacial contact between the active material and substrate, which led to rapid responses [40].

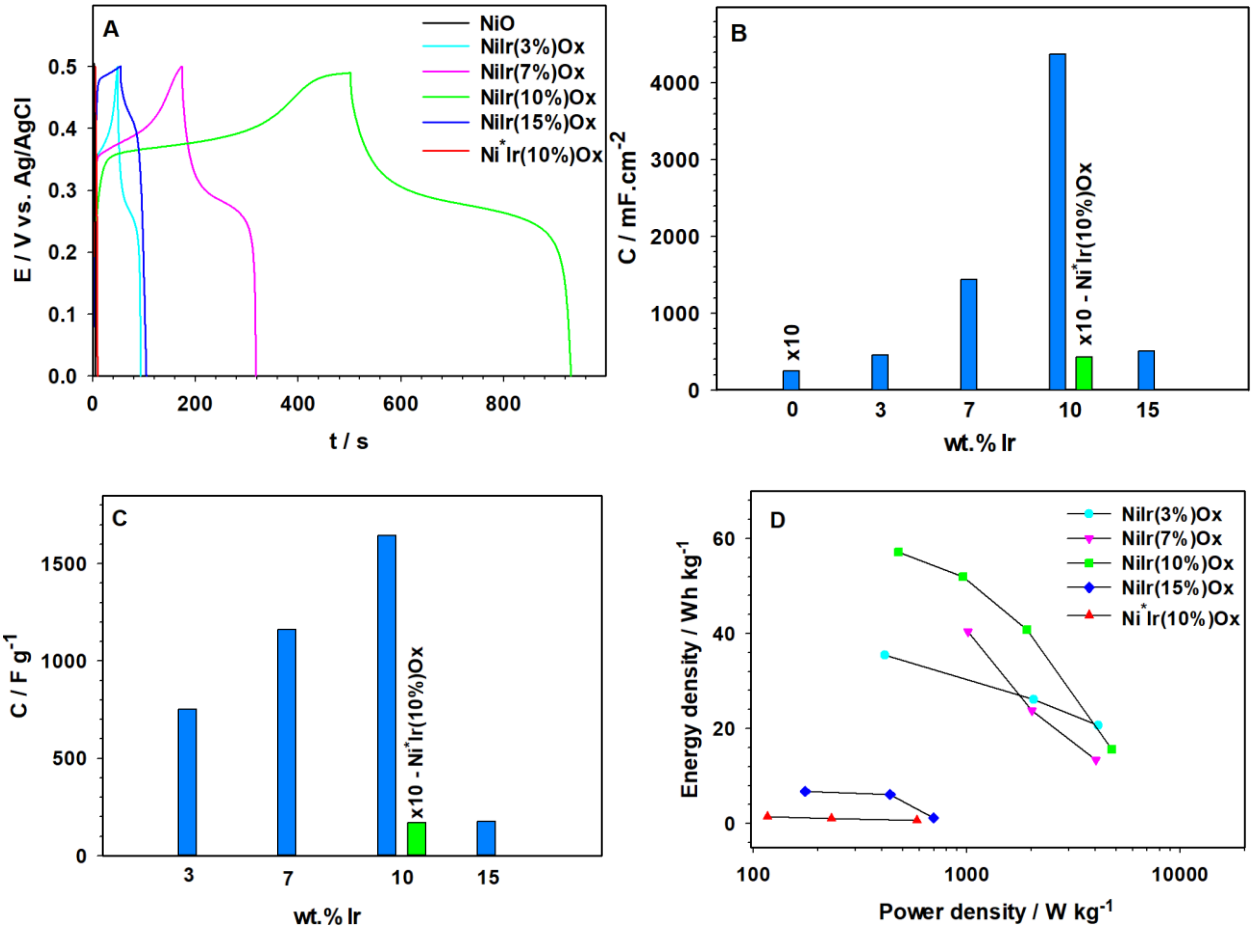

Figure 7.6 (A) Charge/discharge curves of the 3D porous Ni samples modified with various percentages of the iridium at the applied current density of 5.0 mA cm^{-2}, (B) & (C) the corresponding geometric and gravimetric specific capacitances of the 3D porous NiIr(y%)Ox electrodes, where y% was 3.0, 7.0, 10.0, and 15.0 wt.% of iridium, and (D) corresponding Ragone plot (correlation of the energy density with the power density) of the fabricated NiIr oxide electrodes.

To assess the effects of the 3D porous Ni substrate, a nickel plate with an identical loading of the iridium chloride precursor as the 3D porous NiIr(10%)Ox electrode, was denoted as Ni*Ir(10%)Ox. The capacitances of all the fabricated electrodes were calculated using charge/discharge curves with the results presented in Figure 7.6B and C. The specific capacitances of the 3D porous NiIr(y%)Ox electrodes, where y% was 3.0, 7.0, 10.0, and 15.0 wt.% of iridium,

were 750, 1162, 1643, and 176 F g^{-1} (or 455, 1441, 4377, and 504 mF cm^{-2}), respectively. By increasing the quantity of iridium chloride precursor to the 3D porous nickel, up to 10% in NiIr(10%)Ox, the specific capacitance was increased as a result. However, the further addition of Ir to 15% resulted in a decrease in the specific capacitance of the formed NiIr(15%)Ox electrode. This might have been due to the over stacking of iridium oxide through the fabrication process, caused by the excessive casting of iridium, which could cover most of the pores of the 3D nickel substrate. This would lead to an almost structurally flat surface, similar to the Ni*Ir(10%)Ox electrode, where a smooth nickel plate was employed as the substrate.

The specific capacitance of the 3D porous NiO electrode was also calculated to be 25 mF cm^{-2}, which was 175 times smaller than that of the 3D porous NiIr(10%)Ox electrode, demonstrating the significant enhancement of the capacitance through the addition of 10.0 wt.% Ir. In addition, the specific capacitance of the Ni*Ir(10%)Ox electrode was calculated to be 17.05 F g^{-1}. Although the same amount of the IrO_2 was deposited, the specific capacitance of the 3D porous NiIr(10%)Ox electrode was >95 times larger than that of the Ni*Ir(10%)Ox electrode. This confirmed the considerable contribution of the electrodeposited 3D porous Ni network template in serving as a substrate for the anchoring of iridium oxide particles.

Figure 7.6D presents the Ragone plot (correlation of the energy density with the power density) of the fabricated NiIrOx electrodes. The energy density (E) and power density (P) of the electrodes were calculated based on the following equations [41]:

$$E = \frac{1}{2} C(\Delta V)^2 \qquad (1)$$

$$P = \frac{E}{\Delta t} \qquad (2)$$

where C is the gravimetric capacitance, ΔV is the potential window, and Δt is the discharge time. For the NiIr(10%)Ox electrode, an extremely high energy density (57.07 Wh kg^{-1}) was

attained at a power density of 478.8 W kg^{-1}. Although the increase in power density was accompanied by a continuing decrease in the energy density, a high energy density of 15.56 Wh kg^{-1} was achieved at a power density of 4787.5 W kg^{-1}. This improved energy density might be ascribed to the formation of a unique 3D porous NiIrOx structure, which was readily available for electrochemical reactions through Faradaic charge transfer between the electrolyte and electrode; thereby enhancing the efficiency of the composite [29]. For the NiIr(3%)Ox electrode, the energy density attained a value as high as 35.41 Wh kg^{-1} at a power density of 412.2 W kg^{-1}, whereas increasing the power density to 4122.0 W kg^{-1} resulted in a decrease of the energy density value to 20.60 Wh kg^{-1}. The same pattern of behavior for energy and power density was observed for the NiIr(7%)Ox electrode. As expected, the electrode with 15.0 wt.% Ir (NiIr(15%)Ox) exhibited energy and power densities that were lower than the other electrodes. The Ni plate that was supported by iridium oxide (Ni*Ir(10%)Ox) delivered even lower energy and power densities, further verifying the significance of the 3D interconnected porous Ni network as a viable template for capacitor development.

Figure 7.7A displays the cyclic voltammograms of the 3D porous NiIr(10%)Ox electrode recorded in a 1.0 M KOH solution at scan rates that varied from 5 to 60 mV s^{-1}. The shape of all the CV curves was negligibly affected by altering the scan rate, which indicated high electron transfer, as well as the stable electrochemical pseudocapacitive behavior of the electrode. Figure 7.7B presents the plots of the anodic and cathodic peak currents vs. the square root of the applied potential scan rates. The good linear relationship is an indication that the diffusion of the OH^- ions might control the overall process [42, 43]. The capacitance values of the NiIr(10%)Ox electrode at scan rates of 5, 10, 20, 40, and 60 mV s^{-1} were calculated to be 712.0, 550.2, 380.0, 226.5, and

160.8 F g^{-1} as presented in Figure 7.7C (or 1859, 1436, 991, 591, and 420 mF cm^{-2}, as shown in Figure 7.7D), respectively.

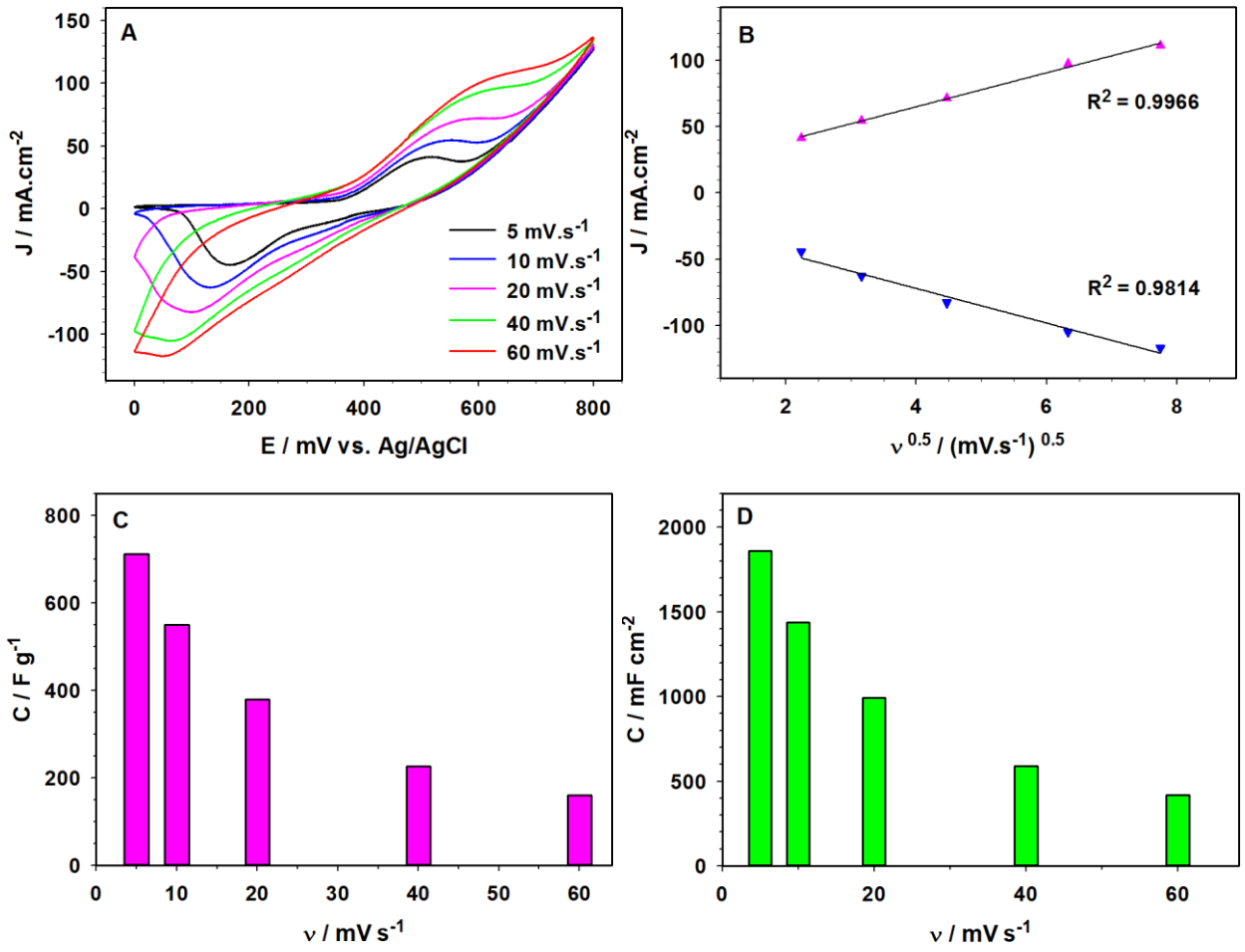

Figure 7.7 (A) Cyclic voltammograms of the 3D porous NiIr(10%)Ox electrode recorded in 1.0 M KOH solution at the scan rates varied from 5 to 60 mV s^{-1}, (B) the anodic and cathodic peak currents vs. the square root of the applied potential scan rates, (C) & (D) the gravimetric and geometric capacitances of the NiIr(10%)Ox electrode as a function of the scan rate, respectively.

Decreasing the potential scan rate resulted in an increase in capacitance, which suggested that the capacitance was primarily associated with the redox reaction [44]. At low scan rates, both the

inner and outer layer materials may be accessed by electrolytic species. However, at higher scan rates the probability of ion diffusion occurring at the outer surface is higher than for the inner layer. Further, the gradual decrease of the specific capacitance in conjunction with the scan rate might be due to the 3D porous structure of the electrode acting as an OH^- buffering reservoir, which in turn, resulted in the reduction of the ion transport path that hindered the sudden drop in the specific capacitance [44].

The galvanostatic charge/discharge curves of the 3D porous NiIr(10%)Ox electrode recorded at three different applied current densities of 5.0, 10.0, and 20.0 mA cm^{-2} are presented in Figure 7.8A. As discussed earlier, the potential drop at the onset of the discharge process, which was primarily due to the internal resistance of the electrode, was negligible (~ 0.021 V at a discharge current density of 5.0 mA cm^{-2}). The gravimetric and geometric specific capacitances were calculated from the discharge curves, with the results presented in Figure 7.8B and C, respectively. An extremely high specific capacitance of 1643 F g^{-1} (4377 mF cm^{-2}) was achieved at 5.0 mA cm^{-2}. Although it gradually decreased with a higher applied current density, large specific capacitances of 1497 and 1175 F g^{-1} (3909 and 3066 mF cm^{-2}) were attained at current densities of 10.0 and 20.0 mA cm^{-2}, respectively.

These results revealed the excellent charge storage performance and rate capability of the 3D porous NiIr(10%)Ox electrode. As can be seen in Figure 7.8B-C, the specific capacitance and the rate capability of the 3D porous NiIr(10%)Ox electrode developed in the present study, were significantly enhanced in contrast to various metal oxides and hydroxides reported in the literature. The superior performance of the NiIr(10%)Ox electrode might be attributed primarily to the unique 3D porous structure, as well as good interfacial bonding, which were beneficial for ion diffusion, while it improved charge transfer throughout the charge/discharge process.

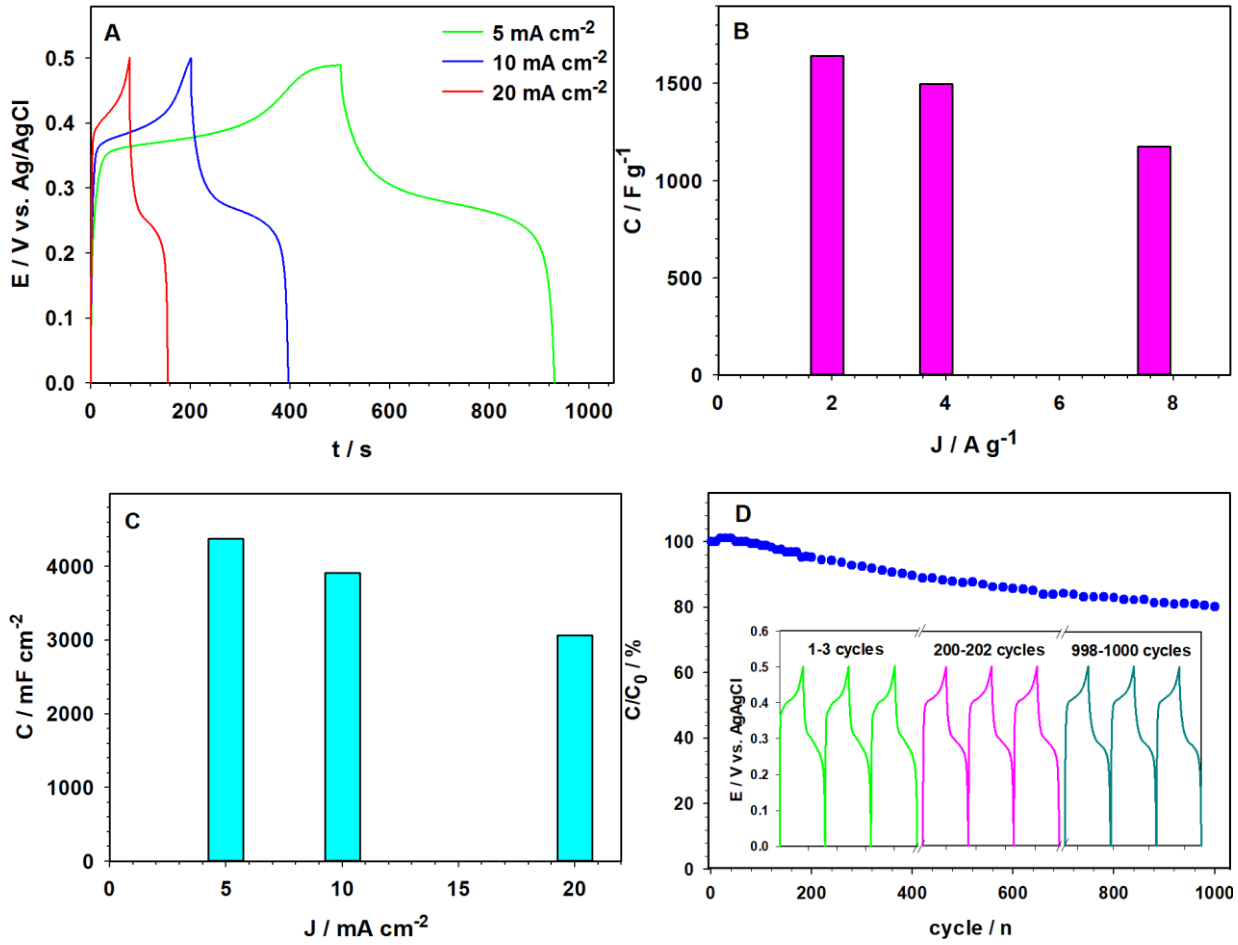

Figure 7.8 (A) The galvanostatic charge/discharge behavior of the NiIr(10%)Ox electrode in the 1.0 M KOH solution recorded at three different applied current densities of 5.0, 10.0, and 20.0 mA cm^{-2}, (B) & (C) the gravimetric and geometric capacitances vs. the applied current density, and (D) the cycling stability of the 3D porous NiIr(10%)Ox electrode using the galvanostatic charge/discharge at a current density of 20.0 mA cm^{-2} (the inset presents the charge/discharge curves of the electrode at different intervals).

7.3.4 Cycling stability of the 3D porous NiIr(10%)Ox electrode

The cycling stability of the 3D porous NiIr(10%)Ox electrode was further assessed using the galvanostatic charge/discharge method at a high current density of 20.0 mA cm^{-2}. As seen in Figure 7.8D, the electrode demonstrated good cycling performance, where the specific capacitance had a value of 2459 mF cm^{-2} following 1000 charge/discharge cycles. The charge/discharge curves of the electrode at different intervals are presented as the inset in Figure 7.8D. The charge/discharge

profile did not show any discernible change over 1000 cycles. The excellent performance of this pseudocapacitor might be attributed to the unique structure and high chemical stability of the 3D porous NiIr(10%)Ox electrode.

Table 7.2 Specific capacitance of various recently developed electrochemical capacitors

Material	**C_s**	**Applied current density**	**Ref.**
NiO	377.9 F g^{-1}	2 A g^{-1}	[45]
NiO	390 F g^{-1}	2 A g^{-1}	[46]
NiO	401 F g^{-1}	0.5 mA cm^{-2}	[47]
NiO	239 F g^{-1}	0.2 A g^{-1}	[23]
NiO/rGO	428 F g^{-1}	0.38 A g^{-1}	[48]
NiO/UDG [1]	425 F g^{-1}	2 A g^{-1}	[49]
Graphene sheet/NiO	400 F g^{-1}	2 A g^{-1}	[50]
NiO/Graphene	651 F g^{-1}	1 A g^{-1}	[51]
Amorphous mesoporous NiO/carbon	1272 F g^{-1} / 1820 mF cm^{-2}	1 A g^{-1}	[12]
Hierarchical flower-like C/NiO composite hollow microspheres	585 F g^{-1}	1 A g^{-1}	[52]
Ni_2CoS_4@$NiCo_2O_4$/CFP [2]	1501 F g^{-1} / 1860 mF cm^{-2}	1 mA cm^{-2}	[53]
$NiCo_2O_4$/MSBPC composite [3]	1604 F g^{-1}	2 A g^{-1}	[22]
rGO/$Ni(OH)_2$ NP/ CNTs	1235 F g^{-1}	1 A g^{-1}	[10]
3D porous $Ni(OH)_2$/Ni	922 mF cm^{-2}	1 mA cm^{-2}	[21]
Amorphous Ni-P	1597 F g^{-1}	0.5 A g^{-1}	[54]
rGO paper-based Ni–Mn LDH/graphene composite	217.8 mF cm^{-2}	2 mA cm^{-2}	[55]
IrO_2–Ta_2O_5/WO_3 nanocomposite [4]	250.0 F g^{-1}	0.25 mA cm^{-2}	[28]
IrO_2NT/MWCNT [4]	69.0 F g^{-1}	0.1 mA cm^{-2}	[29]
$Ir_{0.4}Ru_{0.6}$-oxide [4]	85.0 mF cm^{-2}	0.1 mA cm^{-2}	[31]
3D NiO modified with IrO_2	1643 F g^{-1} / 4377.6 mF cm^{-2}	1.92 A g^{-1} / 5 mA cm^{-2}	Present work

[1] Ultrathin Derived Graphene
[2] Carbon Fiber Paper
[3] Mollusc Shell Based Macro-Porous Carbon
[4] Supercapacitor

7.4 Conclusions

An interconnected 3D porous nickel network electrode was fabricated via a facile electrodeposition method with the assistance of simultaneously formed hydrogen bubbles as the template. Among the electrodes prepared at various current densities for different durations, the 3D porous Ni electrode electrodeposited at 3.0 A cm^{-2} for 150 s exhibited the highest EASA. The optimized 3D Ni network electrode was modified with iridium oxide via a thermal oxidation process. The developed 3D porous NiIr(10%)Ox electrode demonstrated a superbly high specific capacitance of 4377 $mF.cm^{-2}$ or 1643 $F.g^{-1}$ at an applied charge/discharge current density of 5.0 $mA.cm^{-2}$. This was ~175 times higher than the unmodified 3D NiO electrode and over 95 times larger than the Ni*Ir(10%)Ox electrode (where a smooth Ni surface served as the substrate). Further, the 3D porous NiIr(10%)Ox electrode displayed good cyclic stability, as well as a high charge/discharge rate capacity. The excellent electrochemical properties and capacitive performance of the 3D porous NiIr(10%)Ox electrode might be attributed to the very high EASA of the substrate, high conductivity, and high stability, showing promising applications for energy storage.

References

[1] G. Wang, L. Zhang, J. Zhang, A review of electrode materials for electrochemical supercapacitors, *Chem. Soc. Rev.*, 2012, **141**, 797-828.

[2] C. Guan, J. Liu, Y. Wang, L. Mao, Z. Fan, Z. Shen, H. Zhang, J. Wang, Iron oxide-decorated carbon for supercapacitor anodes with ultrahigh energy density and outstanding cycling stability, *ACS Nano.*, 2015, **9**, 5198-5207.

[3] H. B. Li, M. H. Yu, F. X. Wang, P. Liu, Y. Liang, J. Xiao, C. X. Wang, Y. X. Tong, G. W. Yang, Amorphous nickel hydroxide nanospheres with ultrahigh capacitance and energy density as electrochemical pseudocapacitor materials, *Nat. Commun.*, 2013, **4**, 1894.

[4] X. Cheng, X. Gui, Z. Lin, Y. Zheng, M. Liu, R. Zhan, Y. Zhu, Z. Tang, Three-dimensional α-Fe_2O_3/carbon nanotube sponges as flexible supercapacitor electrodes, *J. Mater. Chem. A*, 2015, **3**, 20927-20934.

[5] L. H. Cui, Y. Wang, X. Shu, J. F. Zhang, C. P. Yu, J. W. Cui, H. M. Zheng, Y. Zhang, Y. C. Wu, Supercapacitive performance of hydrogenated TiO_2 nanotube arrays decorated with nickel oxide nanoparticles, *RSC Adv.*, 2016, **6**, 12185-12192.

[6] Y. T. Shih, K. Y. Lee, Y. S. Huang, Characterization of iridium dioxide–carbon nanotube nanocomposites grown onto graphene for supercapacitor, *J. Alloys Compd.*, 2015, **619**, 131-137.

[7] M.M. Sk, C.Y. Yue, K. Ghosh, R.K. Jena, Review on advances in porous nanostructured nickel oxides and their composite electrodes for high-performance supercapacitors, *J. Power Sources*, 2016, **308**, 121-140.

[8] Z. Ren, J. Li, Y. Ren, S. Wang, Y. Qiu, J. Yu, Large-scale synthesis of hybrid metal oxides through metal redox mechanism for high-performance pseudocapacitors, *Sci. Rep.*, 2016, 6.

[9] S. Dhibar, P. Bhattacharya, G. Hatui, C. K. Das, Transition metal doped poly(aniline-co-pyrrole)/multi-walled carbon nanotubes nanocomposite for high performance supercapacitor electrode materials, *J. Alloys Compd.*, 2015, **625**, 64-75.

[10] L. L. Zhang, Z. Xiong, X. Zhao, A composite electrode consisting of nickel hydroxide, carbon nanotubes, and reduced graphene oxide with an ultrahigh electrocapacitance, *J. Power Sources*, 2013, **222**, 326-332.

[11] S. Y. Kim, H. M. Jeong, J. H. Kwon, I. W. Ock, W. H. Suh, G. D. Stucky, J. K. Kang, Nickel oxide encapsulated nitrogen-rich carbon hollow spheres with multiporosity for high-performance pseudocapacitors having extremely robust cycle life, *Energ. Environ. Sci.*, 2015, **8**, 188-194.

[12] K. Tao, P. Li, L. Kang, X. Li, Q. Zhou, L. Dong, W. Liang, Facile and low-cost combustion-synthesized amorphous mesoporous NiO/carbon as high mass-loading pseudocapacitor materials, *J. Power Sources*, 2015, **293**, 23-32.

[13] V. Senthilkumar, F.B. Kadumudi, N.T. Ho, J.W. Kim, S. Park, J.S. Bae, W.M. Choi, S. Cho, Y.S. Kim, NiO nanoarrays of a few atoms thickness on 3D nickel network for enhanced pseudocapacitive electrode applications, *J. Power Sources*, 2016, **303**, 363-371.

[14] H. Li, M. Yu, X. Lu, P. Liu, Y. Liang, J. Xiao, Y. X. Tong, G. W. Yang, Amorphous cobalt hydroxide with superior pseudocapacitive performance, *ACS Appl. Mater. Interfaces*, 2014, **6**, 745-749.

[15] J. Y. Kim, K. H. Kim, H. K. Kim, S. H. Park, K. C. Roh, K. B. Kim, Template-free synthesis of ruthenium oxide nanotubes for high-performance electrochemical capacitor, *ACS. Appl. Mater. Interfaces*, 2015, **7**, 16686-16693.

[16] C. H. Xu, P. Y. Shen, Y. F. Chiu, P. W. Yeh, C. C. Chen, L. C. Chen, C. C. Hsu, I. C. Cheng, J. Z. Chen, Atmospheric pressure plasma jet processed nanoporous Fe_2O_3/CNT composites for supercapacitor application, *J. Alloys Compd.*, 2016, **676**, 469-473.

[17] A. Chen, C. Ostrom, Palladium-based nanomaterials: synthesis and electrochemical applications, *Chem. Rev.*, 2015, **115**, 11999-12044

[18] H. C. Shin, M. Liu, Copper foam structures with highly porous nanostructured walls, *Chem. Mater.*, 2004, **16**, 5460-5464.

[19] H. C. Shin, M. Liu, Three-dimensional porous copper–tin alloy electrodes for rechargeable lithium batteries, *Adv. Funct. Mater.*, 2005, **15**, 582-586.

[20] Y. Li, Y. Y. Song, C. Yang, X. H. Xia, Hydrogen bubble dynamic template synthesis of porous gold for nonenzymatic electrochemical detection of glucose, *Electrochem. Commun.*, 2007, **9**, 981-988.

[21] H. Jiang, Y. Guo, T. Wang, P. L. Zhu, S. Yu, Y. Yu, X. Z. Fu, R. Sun, C. P. Wong, Electrochemical fabrication of $Ni(OH)_2$/Ni 3D porous composite films as integrated capacitive electrodes, *RSC Adv.*, 2015, **5**, 12931-12936.

[22] J. Liu, J. Jiang, M. Bosman, H. J. Fan, Three-dimensional tubular arrays of MnO_2–NiO nanoflakes with high areal pseudocapacitance, *J. Mater. Chem.*, 2012, **22**, 2419-2426.

[23] J. Liang, M. Li, Y. Chai, M. Luo, L. Li, TEOA-mediated formation of hollow core-shell structured $CoNi_2S_4$ nanospheres as a high-performance electrode material for supercapacitors, *J. Power Sources*, 2017, **362**, 123-130.

[24] S. K. Meher, P. Justin, G. R. Rao, Nanoscale morphology dependent pseudocapacitance of NiO: Influence of intercalating anions during synthesis, *Nanoscale*, 2011, **3**, 683-692.

[25] L. Cui, J. Cui, H. Zheng, Y. Wang, Y. Qin, X. Shu, J. Liu, Y. Zhang, Y. Wu, Construction of NiO/MnO_2/CeO_2 hybrid nanoflake arrays as platform for electrochemical energy storage, *J. Power Sources*, 2017, **361**, 310-317.

[26] W. Xiong, Y. Gao, X. Wu, X. Hu, D. Lan, Y. Chen, X. Pu, Y. Zeng, J. Su, Z. Zhu, Composite of macroporous carbon with honeycomb-like structure from mollusc shell and $NiCo_2O_4$ nanowires for high-performance supercapacitor, *ACS Appl. Mater. Interfaces*, 2014, **6**, 19416-19423.

[27] T. H. Ko, S. Radhakrishnan, M. K. Seo, M. S. Khil, H. Y. Kim, B. S. Kim, A green and scalable dry synthesis of $NiCo_2O_4$/graphene nanohybrids for high-performance supercapacitor and enzymeless glucose biosensor applications, *J. Alloys Compd.*, 2017, **696**, 193-200.

[28] S. S. Thind, X. Chang, J. S. Wentzell, A. Chen, High-performance supercapacitor based on tantalum iridium oxides supported on tungsten oxide nanoplatelets, *Electrochem. Commun.*, 2016, **67**, 1-5.

[29] Y. M. Chen, J. H. Cai, Y. S. Huang, K. Y. Lee, D. S. Tsai, Preparation and characterization of iridium dioxide–carbon nanotube nanocomposites for supercapacitors, *Nanotechnol.*, 2011, **22**, 115706.

[30] Y. Lee, J. Suntivich, K. J. May, E. E. Perry, Y. Shao-Horn, Synthesis and activities of rutile IrO_2 and RuO_2 nanoparticles for oxygen evolution in acid and alkaline solutions, *J. Phys. Chem. Lett.*, 2012, **3**, 399-404.

[31] N. Ullah, M. A. McArthur, S. Omanovic, Iridium-ruthenium-oxide coatings for supercapacitors, *Can. J. Chem. Eng.*, 2015, **93**, 1941-1948.

[32] K. Ramachandran, Ni-Co bimetal nanowires filled multiwalled carbon nanotubes for the highly sensitive and selective non-enzymatic glucose sensor applications, *Sci. Rep.*, 2016, **6**, 36583.

[33] M. C. Biesinger, B. P. Payne, L. W. Lau, A. Gerson, R. S. Smart, X-ray photoelectron spectroscopic chemical state quantification of mixed nickel metal, oxide and hydroxide systems, *Surf. Interface Anal.*, 2009, **41**, 324-332.

[34] J. Ma, L. Yin, T. Ge, 3D hierarchically mesoporous Cu-doped NiO nanostructures as high-performance anode materials for lithium ion batteries, *CrystEngComm*, 2015, **17**, 9336-9347.

[35] R. S. Chen, Y. S. Huang, Y. M. Liang, D. S. Tsai, Y. Chi, J. J. Kai, Growth control and characterization of vertically aligned IrO_2 nanorods, *J. Mater. Chem.*, 2003, **13**, 2525-2529.

[36] T. Audichon, T. W. Napporn, C. Canaff, C. Morais, C. Comminges, K. B. Kokoh, IrO_2 coated on RuO_2 as efficient and stable electroactive nanocatalysts for electrochemical water splitting, *J. Phys. Chem. C*, 2016, **120**, 2562-2573.

[37] G. Wang, D. S. Tsai, Y. S. Huang, A. Korotcov, W. C. Yeh, D. Susanti, Selective growth of IrO_2 nanorods using metalorganic chemical vapor deposition, *J. Mater. Chem.*, 2006, **16**, 780-786.

[38] W. Yang, Z. Gao, J. Ma, J. Wang, X. Zhang, L. Liu, Two-step electrodeposition construction of flower-on-sheet hierarchical cobalt hydroxide nano-forest for high-capacitance supercapacitors, *Dalton Trans.*, 2013, **42**,15706-15715.

[39] J. F. Rivera, I. Pignot-Paintrand, E. Pereira, B. L. Rivas, J. C. Moutet, Electrosynthesized iridium oxide-polymer nanocomposite thin films for electrocatalytic oxidation of arsenic (III), *Electrochim. Acta*, 2013, **110**, 465-473.

[40] S. Zhou, J. Xu, Y. Xiao, N. Zhao, C. P. Wong, Low-temperature Ni particle-templated chemical vapor deposition growth of curved graphene for supercapacitor applications, *Nano Energy*, 2015, **13**, 458-466.

[41] Y. Gao, Y. S. Zhou, M. Qian, X. N. He, J. Redepenning, P. Goodman, H. M. Li, L. Jiang, Y. F. Lu, Chemical activation of carbon nano-onions for high-rate supercapacitor electrodes, *Carbon*, 2013, **51**, 52-58.

[42] T. Nguyen, M. Boudard, M. J. Carmezim, M. F. Montemor, Hydrogen bubbling-induced micro/nano porous MnO_2 films prepared by electrodeposition for pseudocapacitor electrodes, *Electrochim. Acta*, 2016, **202**, 166-174.

[43] W. Sun, X. Rui, M. Ulaganathan, S. Madhavi, Q. Yan, Few-layered $Ni(OH)_2$ nanosheets for high-performance supercapacitors, *J. Power Sources*, 2015, **295**, 323-328.

[44] L. Xuan, L. Chen, Q. Yang, W. Chen, X. Hou, Y. Jiang, Q. Zhang, Y. Yuan, Engineering 2D multi-layer graphene-like Co_3O_4 thin sheets with vertically aligned nanosheets as basic building units for advanced pseudocapacitor materials, *J. Mater. Chem. A*, 2015, **3**, 17525-17533.

[45] G. Cheng, Q. Bai, C. Si, W. Yang, C. Dong, H. Wang, Y. Gao, Z. Zhang, Nickel oxide nanopetal-decorated 3D nickel network with enhanced pseudocapacitive properties, *RSC Adv.*, 2015, **5**, 15042-15051.

[46] X. Zhang, W. Shi, J. Zhu, W. Zhao, J. Ma, S. Mhaisalkar, T. L. Maria, Y. Yang, H. Zhang, H. H. Hng, Q. Yan, Synthesis of porous NiO nanocrystals with controllable surface area and their application as supercapacitor electrodes, *Nano Res.*, 2010, **3**, 643-652.

[47] S. Vijayakumar, S. Nagamuthu, G. Muralidharan, Supercapacitor studies on NiO nanoflakes synthesized through a microwave route, *ACS Appl. Mater. Interfaces*, 2013, **5**, 2188-2196.

[48] W. Li, Y. Bu, H. Jin, J. Wang, W. Zhang, S. Wang, J. Wang, The preparation of hierarchical flowerlike NiO/reduced graphene oxide composites for high performance supercapacitor applications, *Energy Fuels*, 2013, **27**, 6304-6310.

[49] C. Wu, S. Deng, H. Wang, Y. Sun, J. Liu, H. Yan, Preparation of novel three-dimensional NiO/ultrathin derived graphene hybrid for supercapacitor applications, *ACS Appl. Mater. Interfaces*, 2014, **6**, 1106-1112.

[50] X. Xia, J. Tu, Y. Mai, R. Chen, X. Wang, C. Gu, X. Zhao, Graphene sheet/porous NiO hybrid film for supercapacitor applications, *Chem. Eur. J.*, 2011, **17**, 10898-10905.

[51] M. L. Huang, C. D. Gu, X. Ge, X. L. Wang, J. P. Tu, NiO nanoflakes grown on porous graphene frameworks as advanced electrochemical pseudocapacitor materials, *J. Power Sources*, 2014, **259**, 98-105.

[52] T. Liu, C. Jiang, B. Cheng, W. You, J. Yu, Hierarchical flower-like C/NiO composite hollow microspheres and its excellent supercapacitor performance, *J. Power Sources*, 2017, **359**, 371-378.

[53] L. Cao, G. Tang, J. Mei, H. Liu, Construct hierarchical electrode with $Ni_xCo_{3-x}S_4$ nanosheet coated on $NiCo_2O_4$ nanowire arrays grown on carbon fiber paper for high-performance asymmetric supercapacitors, *J. Power Sources*, 2017, **359**, 262-269.

[54] D. Wang, L. B. Kong, M. C. Liu, W. B. Zhang, Y. C. Luo, L. Kang, Amorphous Ni–P materials for high performance pseudocapacitors, *J. Power Sources*, 2015, **274**, 1107-1113.

[55] W. Quan, Z. Tang, S. Wang, Y. Hong, Z. Zhang, Facile preparation of free-standing rGO paper-based Ni–Mn LDH/graphene superlattice composites as a pseudocapacitive electrode, *Chem. Commun.*, 2016, **52**, 3694-3696.

Chapter 8: Conclusions and Future Prospects

8.1 Conclusions

Nickel is a naturally abundant transition metal with very fascinating characteristics, which is why this thesis is dedicated to broadening the knowledge of the anodic dissolution behavior and residue formation through the process as well as affecting parameters. By implementing the results of these studies, the related industries can hopefully avoid or minimize the challenges. Also, this thesis demonstrates two potential applications for fabricated Ni-based materials for energy related processes. For this purpose, very simple and facile techniques of fabrication such as in-situ electrochemical reduction, electrodeposition, or annealing are employed. The precursors are either very cost-effective materials (e.g. carbon based materials) or the use of more expensive materials is kept to minimum. In summary, the important conclusions of presented work are as follows:

8.1.1 Anodic dissolution of nickel in Watts solution

We demonstrated the surface morphology, crystalline nature, and distribution and the electrochemical characteristics associated with the anodic dissolution of an electrolytic Ni electrode in Watts solution. ICP-AES provided quantitative data as relates to the presence of impurities at the electrolytic Ni electrode during the anodic dissolution by designing a custom-made electrochemical cell. The anodic dissolution process of the electrolytic Ni electrode was systematically investigated by altering the surface morphology and crystallinity through the application of current densities at 4.0, 8.0, and 16.0 mA cm^{-2}. The μ-XRD assisted with an investigation into the crystallinity of electrolytic Ni during the anodic dissolution at a specified

site. The cubic crystalline structure was not altered during the dissolution of the electrolytic Ni electrode, whereas the peak intensity ratio of Ni (111)/(200) planes revealed that the (200) plane intensity increased by prolonging the duration of the anodic dissolution at the electrolytic Ni electrode.

Our investigations suggested that (i) the variable crystalline nature, (ii) the presence of other metallic impurities such as Cu, Fe, and Cr, (iii) the disappearance of the (111) plane Ni crystals and the growth of the (200) plane Ni crystals by increasing the anodic dissolution of the electrolytic Ni, (iv) variable microstructured Ni grains and (v) the localized anodic dissolution behaviors of the electrolytic Ni electrode, might be involved in the formation of the residue. A model investigation was studied for the anodic dissolution of the electrolytic Ni electrode, which demonstrated that the rapid interfacial dissolution kinetics of Ni soluble materials may be readily studied, which could open the way for improvements in industrial refinery based applications.

The anodic dissolution of industrial electrolytic nickel chips under different applied constant current densities was studied to investigate residue formation behaviors and the possible effects of current density during the plating process. CV studies indicated that the process of anodic dissolution began by activating the sample during the first stages. However, at later stages with further dissolution the number of active sites was reduced as a result of this dissolution. Also, at higher current densities (30.0 and 45.0 mA g^{-1}) anodic dissolution more likely occurred in the transpassive region. This might potentially result in the lace-like dissolution of the sample; hence, falling out of neighboring disconnected nickel islands, and the formation of additional residue.

In general, the dissolution began from the sub-layers, edges and bottom of the sample, where only at final stages of the process; the surface of the sample was involved. This might have meant that, as the process continued, the mechanical properties of the sample deteriorated. Under

practical conditions, where the samples are in a basket, the weight of the samples at the top of the pile could result in pulverization of the lower samples. This could likely result in the generation of more residue than would be expected at the beginning of the process, if just one sample was involved. Also, there was slight reduction in residue formation with a decreased applied current. Therefore, lower current densities might be suitable for the initiation of uniform dissolution.

It was shown that (111) oriented crystals were diminishing at a more rapid rate in contrast to (200) planes, thereby resulting in decreasing the peak intensity of the (111)/(200) ratio. This might be indicative of a higher tendency of (111) phase crystals to dissolve. However, most of the collected residue consisted primarily of (111) crystals as well. This could be explained by the formation of pits within the surface defects on the formed oxide layers, which were either formed during the passivation process in the solution, or the natural passive oxide that was formed in the ambient air prior to the use of the samples.

8.1.2 Energy related application of Ni-based materials

We have successfully developed a novel nickel hydroxide/reduced graphene oxide/carbon nitride nanocomposite via a cost-effective and facile one-step electrochemical reduction process of the precursors. Due to the presence of carbon nitride and reduced graphene oxide sheets within the structure and high surface area, the novel fabricated nanocomposite has demonstrated excellent electrocatalytic activity for the oxygen reduction reaction in an alkaline electrolyte. The nanocomposite has demonstrated a very high mass activity of 12.83 $A\ g_{Ni}^{-1}$, along with an improved current density, four-electron transfer number, enhanced resistance to methanol poisoning, and better durability. All of which makes the nickel hydroxide/reduced graphene oxide/carbon nitride nanocomposite a promising non-precious metal cathode catalyst for fuel cell applications. The

novel approach described in this study could open the door to develop other metal or metal oxide/graphene-based nanocomposites for promising energy conversion and environmental.

Finally, an interconnected 3D porous nickel network electrode was fabricated via a facile electrodeposition method with the assistance of simultaneously formed hydrogen bubbles as the template. Among the electrodes prepared at various current densities for different durations, the 3D porous Ni electrode electrodeposited at 3.0 A cm^{-2} for 150 s exhibited the highest EASA. The optimized 3D Ni network electrode was modified with iridium oxide via a thermal oxidation process. The developed 3D porous NiIr(10%)Ox electrode demonstrated a superbly high specific capacitance of 4377 mF cm^{-2} or 1643 F g^{-1} at an applied charge/discharge current density of 5.0 mA cm^{-2}. This was ~175 times higher than the unmodified 3D NiO electrode and over 95 times larger than the Ni*Ir(10%)Ox electrode (where a smooth Ni surface served as the substrate). Further, the 3D porous NiIr(10%)Ox electrode displayed good cyclic stability, as well as a high charge/discharge rate capacity. The excellent electrochemical properties and capacitive performance of the 3D porous NiIr(10%)Ox electrode might be attributed to the very high EASA of the substrate, high conductivity, and high stability, showing promising applications for energy storage.

8.2 Future Work

In this PhD research, I have successfully determined some of the factors, strongly affecting anodic dissolution of electrolytic nickel. I have also successfully developed Ni-based electrode materials with enhanced electrochemical activity towards different applications via facile and efficient electrochemical reduction or electrodeposition methods. All of which will contribute to

the development of both industrial application of nickel as well as highly efficient materials in the future for use in various energy applications.

The study carried out here on anodic dissolution of nickel has employed industrial samples, and has demonstrated a few factors affecting the dissolution behavior as well as residue formation such as applied current density, crystalline structure, and impurities associated with the samples. However, there are quite a few more parameters that could play a role in this matter such as crystal size, surface morphology, or various bath compositions. Also, use of high purity nickel could help minimize the interference and enhance control over the procedure. It is also suggested that nickel samples with specific crystal orientations be prepared and their anodic dissolution behavior be explored to further confirm the findings of this study.

Nickel hydroxide has shown great catalytic activities towards various applications such as methanol oxidation, oxygen evolution, or even electrochemical sensing of compositions like hydrogen peroxide and carbohydrides. Therefore, it is suggested to investigate the fabricated nickel hydroxide/reduced graphene oxide/carbon nitride electrode for use in any of the mentioned applications. Also, studies have shown that metals like Co, Cu, or Fe show great synergistic effect while in composition with nickel, therefore it is suggested to the add these metals to the precursor solutions to be reduced along with nickel and graphene oxide and investigate their activity for oxygen reduction reaction as well as other possible applications mentioned earlier where nickel hydroxide has proven to be active and beneficial for.

Nickel oxide supported iridium oxide has shown enhanced electrochemical pseudo-capacitive behavior compared to nickel oxide alone. Addition of other transition metal oxides such as tantalum oxide, titanium oxide, or tungsten oxide with high capacitive activities to the nickel oxide substrate individually or along with iridium oxide could both further improve the capacitance of the material achieved here, and prolong the cycling ability of the capacitance.

Copper oxide is another material that demonstrates good electrochemical capacitance. Also, electrodeposition of nickel and copper together as an alloy has been explored and is possible. Therefore, it is suggested that substrates of these alloys to be fabricated in the same manner and effect of addition of aforementioned oxides separately or combined on the capacitive behavior be investigated.